Aircraft Engine Efficiency Improvement through an Innovative Active Clearance Control System

Doctoral Dissertation
Doctoral Program in Energy Engineering (31st Cycle)

Aircraft Engine Efficiency Improvement through an Innovative Active Clearance Control System

Alessio Desando
* * * * * *

Supervisors
Prof. Elena Campagnoli, Supervisor

Doctoral Examination Committee:
Prof. Bruno Facchini, Referee, Università degli Studi di Firenze
Prof. Wlodzimierz Wróblewski, Referee, Silesian University of Technology
Prof. Daniele Simoni, Referee, Università degli Studi di Genova
Prof. Riccardo Da Soghe, Referee, ERGON Research srl
Prof. Paolo Maggiore, Referee, Politecnico di Torino

Politecnico di Torino
July 16, 2019

I hereby declare that, the contents and organisation of this dissertation constitute my own original work and does not compromise in any way the rights of third parties, including those relating to the security of personal data.

…….....

Alessio Desando

Turin, July 16, 2019

Summary

The concept at the base of the newest aircraft engines is to improve the efficiency as much as possible. These innovations are mainly aimed at reducing the environmental impact and the fuel consumption, and at producing more durable engines. Due to the already very high degree of optimization achieved in current engines, the introduced technological improvements usually have a limited impact in terms of overall efficiency. However, their contribution in terms of fuel savings is still significant, since the larger engines are capable to develop very high amounts of power. Consequently, the optimization of those engine elements, whose impact was once considered negligible, has become crucial in the last years.

One of these tasks is the control of engine clearances in Low Pressure Turbines (LPT). The clearances are the gaps occurring between static and rotating parts that change during the several flight phases, due to the different thermal loads on the stator and the rotor and to the other forces (i.e., thrust, inertial, centrifugal and aerodynamic loads) acting on the engine. Although a clearance between the rotor blade and the turbine shroud is necessary to avoid damage to the blade of the tip, the presence of too large gaps leads to undesirable energy losses and higher fuel consumption. A solution to reduce these losses is the installation of Active Clearance Control (ACC) systems.

A typical ACC system for LPTs of large aircrafts maintains the clearances at an optimal value, by means of the impingement cooling method: when the gaps are larger than needed, a proper amount of cold air is blown by impinging jets. In this way, the turbine casing undergoes a thermal shrinkage and, after a certain response time, the clearances are closed. The cold air is delivered by means of a duct system that behaves as a plenum.

The main goal of this research is to define a solution that allows improving the performance of current ACC systems. First of all, a detailed literature review

has been accomplished to point out the state of the art and the future perspectives about the ACC design.

Then, a flow network analysis of the entire ACC system has been performed by using a DoE, which included several design parameters. The impact of each analyzed parameter in terms of available mass flow rate for the jet impingement has been evaluated, in order to characterize the robustness of the ACC system when its main design parameters are changed.

Also the next phase is focused on the air delivering system and couples the previous fluid-dynamic studies with the heat pick-up, i.e. the increase in temperature of the cold air, due to the proximity of hotter engine components. In order to carry out these analyses, a 1D analytical tool has been developed. This tool has allowed simulating the entire ACC system with a reasonable accuracy, reducing the computational time, in comparison to a complete 3D model. Moreover, the significant circumferential non-uniformity in terms of mass flow rate and temperatures has been pointed out.

The last part of the present research concerns the impinging jets. In particular, the configurations, which have been investigated, aim to improve heat transfer adding elements that increase the roughness of the turbine case. The Computational Fluid-Dynamics (CFD) method has been applied to carry out this activity, comparing a jet impinging on a flat target surface to other geometries and considering the possible presence of a cross flow. The CFD results, in the case of the flat target surface, have been validated on the literature data.

Contents

List of Tables

List of Figures

Chapter 1

Introduction

1.1 Green Aircrafts for the Future

The present research is a small part of a broader context that ultimately aims to cut the pollutant emissions, thus reducing the human footprint on the Earth. In particular, the CO_2 emissions need a concrete cut within 2030, which allows maintaining the increase of the Earth average temperature below 1.5 Celsius degrees [1].

The spotlight has fallen on the risks related to global warming for the first time, when the first international agreement has been signed with the intent to define measures to reduce the emissions of greenhouse gases: it was 1992 and the United Nations Framework Convention on Climate Change (UNFCCC) was held in Rio.

This agreement had no mandatory value for the signatories, but it laid the foundations for the next negotiations, such as the Kyoto protocol (1997). An outcome of this convention was the commitment, by signatory states, to reduce the emission of greenhouse gases, in particular CO_2, which alone were around the 55% of the total emissions [2].

In the first 2000s, major attentions have been paid to the role played in terms of CO_2 emissions by transportation. In particular, the need for reducing the greenhouse gases, emitted by those transport segments in continuous growth, such as aviation, was pointed out during the UNFCCC that took place in Bali in 2007. The guidelines, proposed to fulfill this objective, led to a worldwide regulation, which has been promulgated by the International Civil Aviation Organization (ICAO) [3].

In this scenario, a set of goals, to be achieved by 2020, has been decided in accordance between the European Commission and the Advisory Council for Aviation Research and Innovation in Europe (ACARE). The main objectives are a 50% reduction in CO_2, an 80% reduction in nitrogen oxides and a decrease in the

perceived noise by 10 dB. In particular, a share of 15-20% of the CO_2 reduction has to be achieved by means of improvements in the engine design.

Weight reduction and efficiency improvement are the two main guidelines that will lead to the green aircraft of the next generation, with lower fuel consumption, i.e. lower pollutant emissions, and extended engine life. In order to transpose these guidelines into technological improvements, the last years have seen the start of many projects aimed to improve the engine performance, each of them focused on a specific topic.

On one hand, the current engine designs already show a high degree of optimization, so the improvements introduced have a limited impact on the overall engine efficiency. On the other hand, the power that a modern aircraft engine can develop is very high, especially when larger aircraft transports are considered. This means that even a small efficiency increase can lead to significant fuel savings, with the consequent environmental and economic benefits. In this perspective, the efforts of the researches performed during the last decades are focused on the optimization of those engine elements, which not long time ago were considered with low benefits-costs impact.

1.2 The Clearance Control in Aircraft Engines

One of the previously mentioned topics is the reduction of the flow through the blade tip clearances. Although these gaps between rotating parts are necessary to prevent the damage of the blade, they need to be controlled or reduced in order to avoid unnecessary energy losses. This task is not simple, since the clearances change during the entire flight path, due to the different thermal loads acting on the stator and rotor or the flight loads acting on the engine, as shown in Figure 1.1 [4].

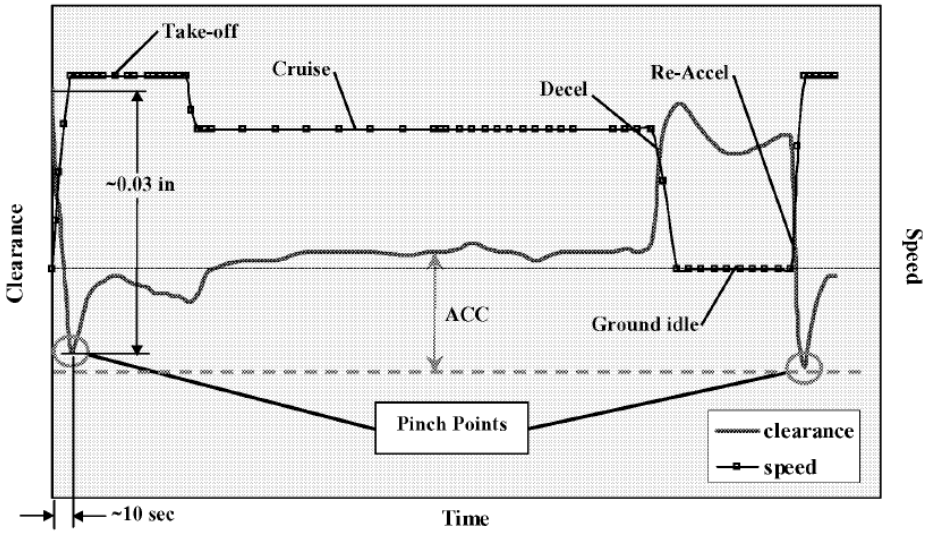

Figure 1.1 - High Pressure Turbine (HPT) tip clearance variations during a mission profile [4].

As shown in the graph, there are sudden events, during which the clearance reaches minimum values, called pinch points. For instance, a pinch point event is recorded during the take-off phase, when the sudden expansion of the rotor blade closes the clearance, and similar events may also occur during the flight when a fast maneuver is required. These events set an important design constraint, known as cold clearance, which is the clearance value when the engine is shut off. Despite this gap is designed to avoid blade rubbing during pinch points, it also determines the clearance value during the other flight phases. As shown in Figure 1.1, the events taking place during a typical flight mission are the following:

- Cold Engine: the clearance value is equal to the design cold clearance.
- Take-off: a sudden expansion of the rotor blades occurs due to the heating and the centrifugal forces, while the casing expands at a slower rate. Consequently, the clearance is closed and the pinch point event occurs. After the pinch point, the clearance starts to increase again. Then, during climb, the rotor heats up again and the clearance closes again.
- Cruise: during this phase, a thermal equilibrium is reached and the clearance is almost constant.
- Throttle transients may occur during the cruise, determining fast clearance variations: attention must be paid in order to avoid blade damage due to rubbing.
- Landing approach: the clearance increases, since the rotor has a lower load and cools down due to the deceleration. A new pinch point may occur if an aborted landing occurs.

A cold clearance that is too large becomes a significant penalty during the cruise phase, increasing unnecessary energy losses. Since cruise is the longest flight phase, many efforts have been paid to reduce the clearance during this part of the flight mission.

On one hand, this objective can be partially fulfilled by using a passive measure, such as a labyrinth seal, that reduces the flow leakage by creating a tortuous path. In the literature there are many studies carried out to identify the best solutions to design this component [5]. High-efficiency labyrinth seals also allow maintaining higher pressure drops across a turbine stage, reducing the risk of hot gas ingestion from the flow path and, thus, reducing the amount of cooling air needed for the downstream cavity pressurization. This is a significant benefit, since the air is bled from the compressor and represents an efficiency penalty.

Although labyrinth seals are very effective in reducing blade tip leakages during each flight phase, they do not allow a proper clearance control, leaving room for a significant efficiency improvement during cruise that could be achieved only by means of an active and more accurate control system. The control action, which is performed by an ACC system, allows changing the clearance value according to the need of each flight phase, in order to optimize the performance. The ACC systems require a certain amount of power to be activated, so the advantage acquired in terms of engine efficiency should be not overwhelmed by system power consumption.

Another advantage related to the usage of ACC systems is the possibility to reduce the cold clearance, if the system exhibits a fast response to the thermal solicitations. The development of fast ACCs is the future direction in the design of these systems [4].

Besides these features, the design of an efficient ACC system encounters another issue, which is the load distribution. On one hand, there are uniform loads, such as the centrifugal forces, the internal pressure and several thermal loads, acting on both stationary and rotating structures, which create a uniform radial displacement in the circumferential direction. On the other hand, there are many other loads (i.e., thermal, thrust, inertial and aerodynamic contributions), usually acting on the stationary part of the engine, which create an asymmetric circumferential displacement. These loads, which may be generated by non-uniform heating or cooling, maneuvers, gyroscopic torques, aerodynamic forces acting on the engine shell, play a relevant role into clearance variations during certain flight phases. Just to give an idea of these effects, Figure 1.2 [4] shows the clearance variations along the engine circumference, during the take-off phase.

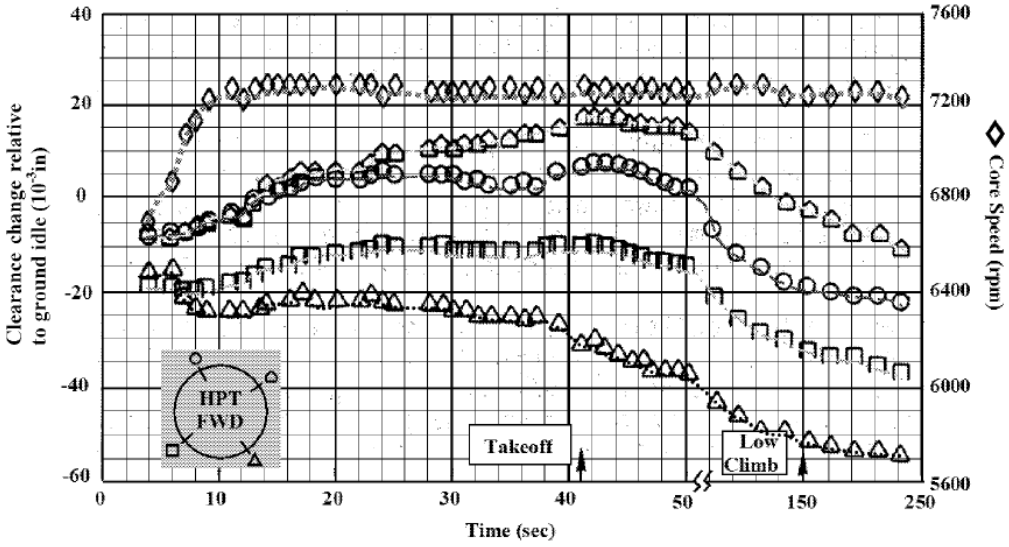

Figure 1.2 - Circumferential HPT clearance variations during take-off, JT9D engine [4]

Note that the ACC system can be installed on several engine components (i.e. the compressor, the high pressure turbine and the low pressure turbine) and its design changes consequently to fit the requirements of each component.

1.3 Research Outline

The aim of this research is to study a method to improve the performance of current ACC systems for Low Pressure Turbines. A special attention has been dedicated to the heat transfer occurring between cooling air jets and the turbine case, proposing a solution capable to improve the efficiency of this mechanism.

The research activity has been carried out in several steps, which are briefly described in this paragraph.

To begin with, Chapter 2 includes the literature review, pointing out the main research topics related to ACC systems. Among the several solutions available, the attention has been focused on thermal ACC systems and, in particular, to the studies concerning jet impingement.

Then, a thermal ACC has been numerically modeled with a 1D approach. The objective of this step, discussed in Chapter 3, is to define the parameters that most influence the mass flow rate distribution inside the duct system composing the ACC.

The next step, reported in Chapter 4, concerns the numerical study of the heat pick-up in the duct system, pointing out the circumferential non-uniformity in the air distribution related to this phenomenon.

Finally, the impinging jets have been analyzed with a CFD methodology. Here, the main purpose is to improve heat transfer by adding elements that increase the roughness of the turbine case. The results are discussed in detail in Chapter 5.

To conclude, the main outcomes of the research activity are summarized in Chapter 6.

Chapter 2

Literature Review

This Chapter is focused on the fundamental work that has to be done before each kind of research, the literature review. Here, the state of the art about the ACC design and the main research topics related to these systems have been pointed out, such as the direction followed by the most recent researches. First of all, an overview about the clearance control systems, which are available today or in the not too distant future, is provided.

While some innovative designs seem to be promising, they are far away from practical applications within the ACARE 2020 deadlines. Among the other possible configurations, the thermal ACC system is currently employed on large civil aircrafts. The present study is focused on this kind of architecture, since it could be improved under many aspects by introducing innovative features.

After some brief considerations about the source of air bleeding, a selection of literature works concerning pressure losses and heat pick-up, which a common thermal ACC system exhibits, are shown. Then, a survey of the studies performed on impinging jets is performed, focusing on the heat transfer enhancement techniques, which have been adopted or investigated in the last decades.

2.1 Clearance Control Systems

As mentioned before, this Paragraph is focused on the clearance control systems currently installed on aircraft engines and on the possible future developments.

A first subdivision for these architectures is into passive and active clearance control systems (PCC and ACC, respectively). Despite the former exhibit the advantage of not requiring any input power, they can be optimized just for a single point of the flight. The latter are capable to perform an active control during the entire mission (by means of Full Authority Digital Engine Control, or FADEC, systems), but require additional power, which must be properly regulated by additional equipment. Consequently, the first guideline in the design

of Active Clearance Control (ACC) systems is that the power saved with these devices is higher than the amount they require to operate. Currently, the power source for ACC systems is air, bled from the fan or from the compressor. So, the usage of these systems should not excessively worsen the performance of these engine components, otherwise they would fail in their purpose.

Beside these designs, which are already operating on current engines, there are also innovative architectures under development. These configurations, known as Fast Active Clearance Control (FACC) systems, are capable not only to perform an active control, but also to obtain a fast response in terms of clearance variations. This point is crucial to achieve a significant cold clearance reduction, meaning a substantial efficiency improvement during cruise. Although FACC systems generally seem promising in terms of performance, they also exhibit some technical issues to be solved, in order to be installed on board of aircrafts.

2.1.1 Pneumatic PCCs

The working principle of these systems consists into utilizing the hydrodynamic effects or gas pressures generated by the engine. Examples of these concepts are blade tip cooling air discharge and floating shroud segments.

In the first design [6], the tip of the turbine blade has a rail that forms a squealer pocket, as shown in Figure 2.1. Within this pocket, there are several ribs, extending along the blade chord, that form vortex-cooling channels. Each channel exhibits a row of cooling nozzles, through which cooling air is discharged. Besides the cooling function, the airflow forms vortices within the channels that reduce the blade tip leakages, providing also a sealing action.

The second concept contemplates a shroud made by floating panels, which are free to slightly move in the axial direction, independently of other engine components [7]. Actually, this design is imposed when shroud panels are made by ceramic composite matrix (CMC). Although these materials are more resistant to high temperatures than metal alloys, they are also more fragile, a feature that makes them less likely to resist to cyclic thermal loads due to other engine components. Besides the manufacturing complexity, this design requires very high tolerances and positioning accuracy, so other solutions are usually preferred.

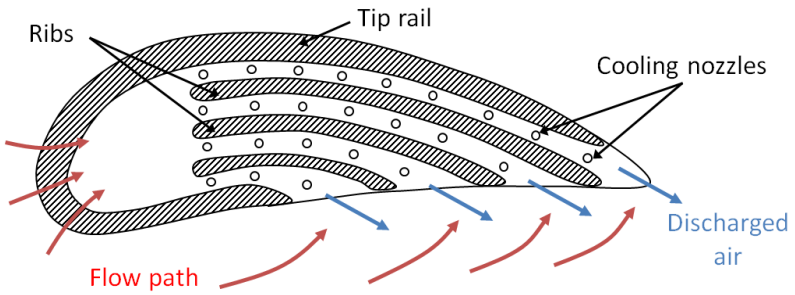

Figure 2.1 - Passive pneumatic clearance control system with blade tip cooling air discharge [6].

2.1.2 Thermal PCCs

Thermal passive control systems rely on the vast knowledge today available on the engine temperature variations during the whole flight and on the material properties. In this approach, those engine components, which are mainly related to clearance variations, are designed to reach the thermal match between rotor and stator with a fast response. More in detail, the choice for the materials of the stator is made in order to follow the centrifugal rotor expansion [8]. Since these architectures are based on well-known mechanisms, they are accurate and reliable. However, their usage is currently limited only to smaller engines. These solutions are indeed designed to avoid pinch point events during rapid transient maneuvers, reducing the required cold clearances. Unfortunately, thermal PCCs are not effective during cruise, the phase where the clearance optimization is really effective in maximizing the fuel savings.

2.1.3 Pneumatic ACCs

These systems perform the control action by using pressure loads generated by the engine or by the secondary air system. The pressure loads, regulated by a series of valves and bellows, are applied on deflectable shroud segments, which are opportunely sealed. An example is the patent [9], shown in the simplified scheme in Figure 2.2. Each pressure pipe is adjacent to a pre-loaded plate that is designed in order to adapt to the shape of the pressure pipe. When the pressure pipe is pressurized, the pre-loaded plate is deflected. In this way, the wall members, which are circumferential segments (each one linked to a pre-loaded plate), are pushed towards the first radial stop position. This position minimizes the clearance and is maintained during steady-state engine operations. As throttle variations, i.e. transient conditions, occur, the pressure within the pressure pipes is released and the wall members move towards the second radial stop position. Here, the clearance is increased to avoid blade rubbing during the transient. After a pre-determined time lapse, pressure is applied again and the condition with the minimum clearance is restored.

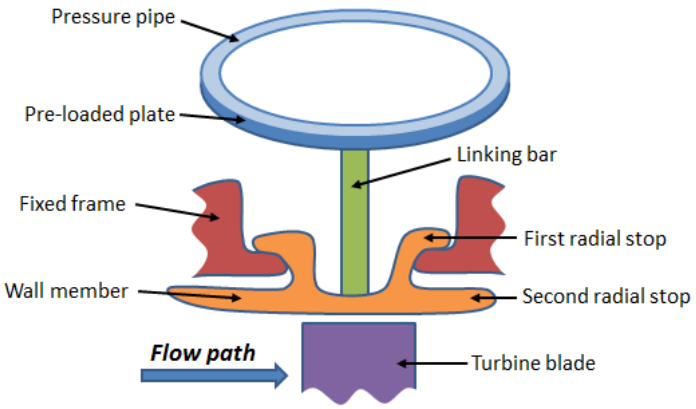

Figure 2.2 - Active pneumatic clearance control system [9].

There are several drawbacks related to this design. For instance, the deflectable surfaces are highly sensitive to fatigue. The correct pressure balance for the pneumatic actuation is also difficult to be maintained, since the overall load seen by the shroud segments may be subjected to very fast variations. Moreover, the price of the active control is to use, as a power source, the air bled from fan or compressor, which negatively affects the engine efficiency.

2.1.4 Thermal ACCs

As well as for pneumatic active control, thermal ACCs require a certain amount of air bled from the upstream engine components. This time, the air is blown on the turbine case to regulate its thermal expansion or contraction.

The type of air bleed applied to the turbine depends, first of all, on cost-benefit considerations. The efficiency improvement is more critical for the High Pressure Turbines (HPT) than for the LPTs. Indeed, while a 10-mils clearance reduction for HPTs may reduce of 1% the SFC, the same reduction in LPT clearances leads to the smaller, but not negligible, contribution of -0.1% Specific Fuel Consumption (SFC) [4]. Consequently, the thermal clearance control for HPTs may use the more expensive air from the compressor, in addition to the air from the fan, to ensure a more effective heat transfer. On the contrary, the case cooling for the LPTs is achieved by using the fan air, at low pressures and temperatures. The compressor air could be used on the LPT case to heat it up when the rotor expands. The introduction of this second contribution would allow achieving a faster thermal response by the turbine casing, thus reducing the requirement in terms of cold clearance, which is needed to avoid blade damage, during manufacturing. Unfortunately, the usage of compressor air is not a cost-effective solution, so it is avoided. Moreover, the thermal ACC exhibits a slow response time, since around a minute is needed to obtain the desired clearance variations, which is not fast enough to be effective during pinch point events.

Thermal ACCs are composed by a system of pipes, which are placed externally the main engine components and deliver the cooling air from the bleeding source to the turbine case [10].

The present research focuses on these systems, whose characteristics and room for further improvements will be identified in the next paragraphs related to the literature review.

2.1.5 ACC by Plasma Actuators

The usage of plasma actuators in aerospace applications seems to be promising in flow control problems. In particular, a concept has been proposed for tip leakage reduction purposes [11]. The working principle of a generic plasma actuator consists into forming a low-temperature plasma between a pair of electrodes. In Figure 2.3, a sheet-type plasma actuator is shown. It is composed by two asymmetric electrodes, one of them exposed to the surrounding air, and separated by a dielectric barrier. As a high-voltage AC signal is applied, the air

molecules near the exposed electrode are ionized and accelerate through the electrical field generated by the imposed voltage. These molecules, while moving towards the electrode, drag other neutral air particles into an induced flow. In other words, electrical energy is directly converted into flow kinetic energy, with the advantage that no moving mechanical parts are needed. The force that can be produced with this mechanism is related to the pressure near the exposed electrode region, since it is related to the air density, thus to the molecules available for ionization. This principle could be applied to delay boundary layer separation along aircraft wing profiles.

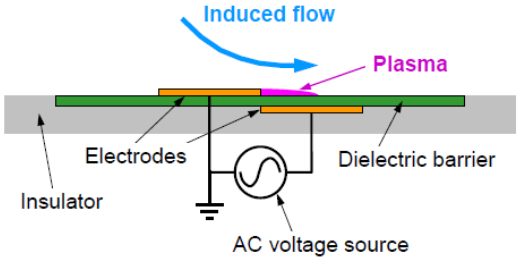

Figure 2.3 - Generic plasma actuator [11]

For applications with the aim to reduce tip leakages, some arrangements are needed, in order to adapt the actuator to the engine environment. Sun et al [11] propose a ring-type plasma actuator, shown in Figure 2.4, left. Here, the second electrode sheet has been replaced by an insulated copper wire. The turbine tip application (see Figure 2.4, right), which is circumferentially extended around the shroud, is composed by several wires to improve the obtained effects.

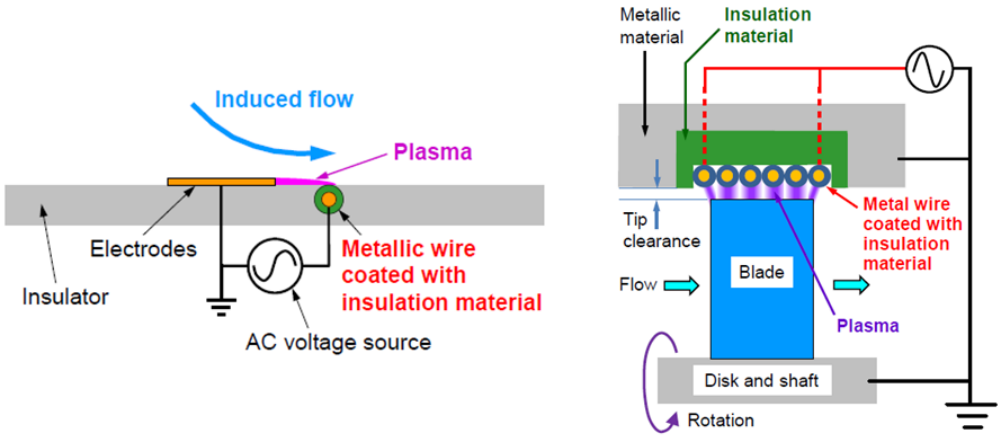

Figure 2.4 - 'Ring-type' plasma actuator: concept (left); turbine tip (right).

This concept ensures the tip leakage reduction by accelerating the air near the blade tips, which forms a vortex that is capable to partially block the lekage air flow. The real effectiveness of this proposal has been experimentally tested on a rig that reproduces a single stage of a rotating turbine. The authors have utilized driving voltages from 3000 to 6000 V, and a low axial speed (around 2 m/s), while the rotating part has been set either to the static contition or to a velocity of 180 RPM. This system proved to be very effective in stopping the leakage flow in static conditions, especially when high input voltages have been applied, i.e.

above 5000 V. However, the degrade in terms of efficiency, recorded when the rotating velocity has been introduced, was not negligible. Since the tested rotating speed was far below the LPT operative conditions, the authors concluded that further tests are needed to investigate the effects under conditions more similar to the actual ones (higher rotation speeds).

2.1.6 Electro-Thermal FACC

The electro-thermal active control is one of the FACC concepts here discussed. The reference paper [12] discusses this design in terms of kinematic and structural feasibility. In particular, this study is composed by a preliminary design phase, involving analytical and numerical methodologies, and, after, by an experimental campaign that confirms the predicted results.

The electro-thermal clearance control is exerted by a truss actuator, which is placed between the inner engine case and the turbine shroud, extending in the circumferential direction (see Figure 2.5). The clearance variations are obtained by applying a thermal load on the actuator structure, i.e. resistive heating that causes expansion or contraction through air cooling. Since the actuation structure is subdivided into shroud elements, it allows a non-symmetric displacement that is a desirable feature, when it is important to properly compensate the asymmetric engine loads.

The truss, made in Inconel 718 alloy, has been realized with a certain pattern, whose basic component is a cell made by four dual-tetrahedron elements, shown in Figure 2.6, top. The clearance variation is obtained as a consequence of the displacements exhibited by the diagonal edges of the cell, when subject to a thermal load (see Figure 2.6, bottom).

The authors pointed out that the angle ω is the major design parameter, since its choice is a trade-off among displacement amplification, structural stiffness and low-mass density. They found that a value around 35 degrees was a good compromise.

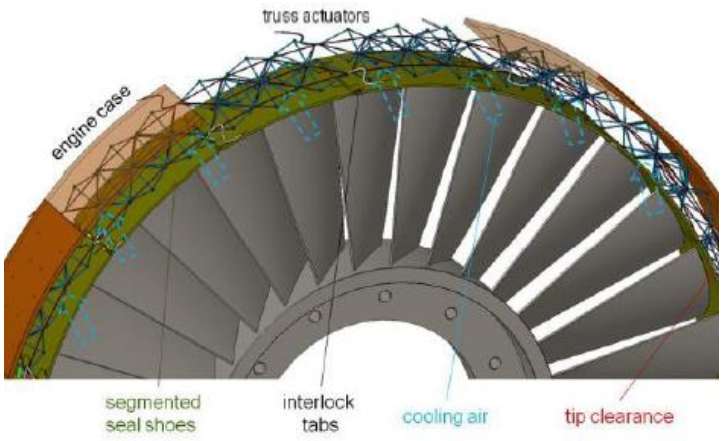

Figure 2.5 - Electro-thermal clearance control concept [12].

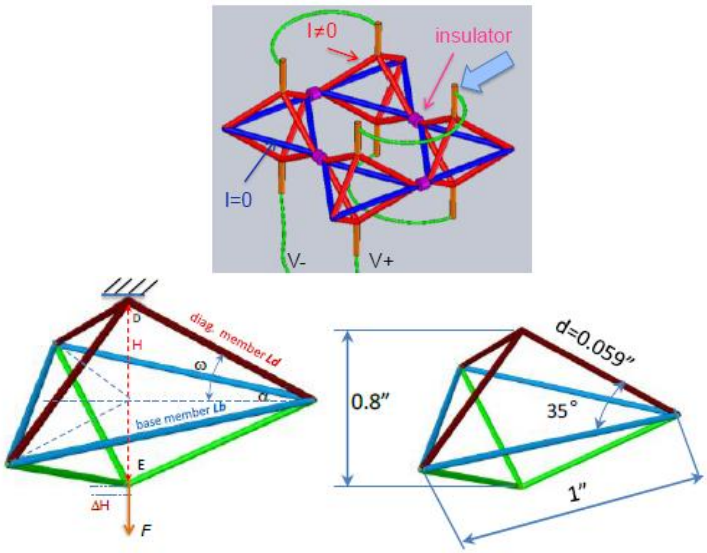

Figure 2.6 - Dual-tetrahedron element: basic cell (top); geometry detail and clearance displacement (bottom) [12].

The most interesting feature of this system is the possibility to reduce the ACC response time, from around a minute (for current thermal ACCs) to a few seconds, disclosing the possibility to reduce the cold clearances in turbines. As for the current thermal ACCs, the cooling air line is still necessary to cool down the truss for clearance reduction. Moreover, an accurate position control is still problematic for this concept and detailed investigations are needed, to characterize in detail the local heat transfer phenomena, which occur in the diagonal elements.

2.1.7 Mechanical FACC

Another typology of FACC system performs the control of the engine clearance by means of mechanical actuators, as a recent study suggests [13]. The approach is to start with a well known, reliable, short-term solution (i.e., electro-hydraulic actuators, shown in Figure 2.7, top), until a long-term solution, more efficient, can be proposed. In particular, the ultimate objective is to develop piezo-electric actuators (Figure 2.7, bottom).

Whatever solution is adopted, the mechanical active clearance control is exerted by a series of actuators, which are circumferentially deployed along the turbine case. The number of actuators can be chosen on the basis of a trade-off that depends on the actuation force required, reliability, positioning accuracy and overall system weight.

Despite these configurations are promising to provide a very fast and accurate clearance control, their application in current large turbofan engines has to face several constraints.

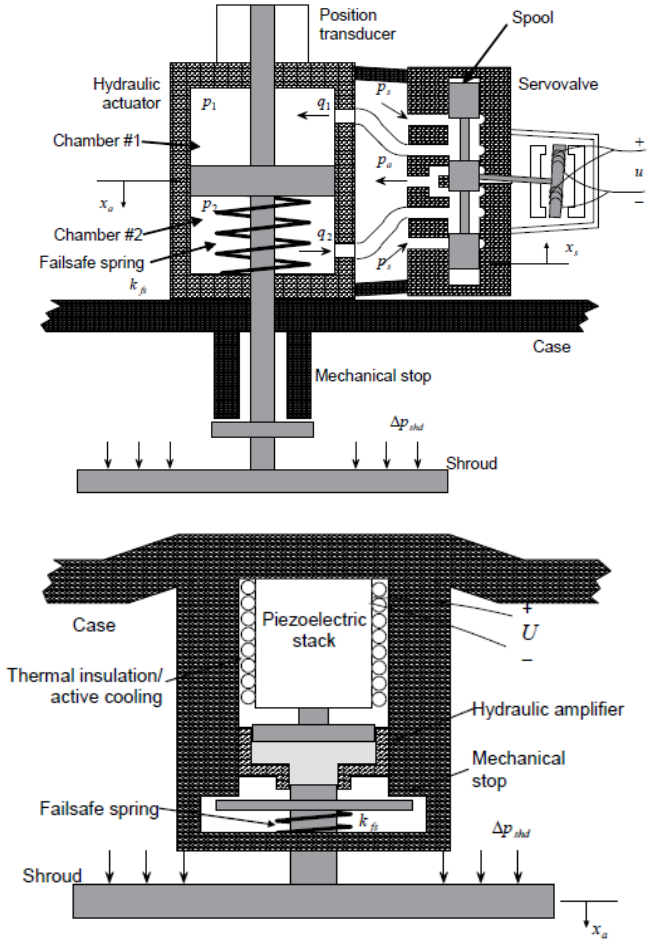

Figure 2.7 - Mechanical actuators: electro-hydraulic (top) and piezo-electric (bottom) [13]

To begin with, it is necessary to develop a very accurate numerical control method for the electronic system, in order to fully exploit the advantages of a fast-response system. Many efforts have been spent in this direction, searching for control method capable of a fast response, high stability and with a reduced positioning error [13, 14]. This problem is further complicated by the possibility to exert a non-uniform clearance control along the engine circumference. Another requirement to be fulfilled, in terms of electronic control, is the improvement of the sensors currently employed to measure clearances. Since these devices provide the reference values to calculate the positioning errors, their measurements should be accurate, both in terms of magnitude and time frequency [15].

Another major issue is represented by the harsh engine environment. The region between the turbine shroud and the turbine case is indeed characterized by temperatures, which are too high for currently available electro-hydraulic actuators. A solution to this problem is to install the actuators in the undercowl region, outside the turbine case (as in Figure 2.7, top). This way, the clearance control would be accomplished by an actuation rod that, in order to move the shroud, passes through a hole drilled on the case surface. Drilling holes on the engine case is not a good solution, since the unavoidable leakage of hot gas that

would be generated would both reduce the engine efficiency and increase the risk of damage to other components.

The high ambient temperature could be a problem also for the long-term solution with piezo-electric materials. However, there are many new materials under study, whose performance appears to be promising for this kind of application [13, 16]. In other words, once the piezo-electric materials have been improved enough, these actuators could be installed inside the turbine case, solving the issue encountered with the electro-hydraulic solution.

2.2 LPT ACC Systems

As mentioned before, the present work will be focused on the thermal ACC system, widely utilized for current large aircraft engines. The numerical modeling of the system has been based on the information provided by the literature, in particular by the patent [10]. The LPT ACC system has a bird-cage structure that envelops the turbine casing, as shown in Figure 2.8. More in detail, there is a main feeding pipe that delivers the cooling air on the turbine case region. It starts with an off-take (not visible in the figure), which collects the air bled from the fan, and its shape is adapted to the space available within the engine external case. At the end of the feeding pipe, there is a wye junction, where the cooling air is split into the two manifold branches. The manifold is a circular, large pipe that distributes the air to a certain number of axial headers, which are linked to the spider rails. These circumferential small pipes are located near the regions where the clearance control is required and have a large number of nozzles to perform the impinging jet cooling [10].

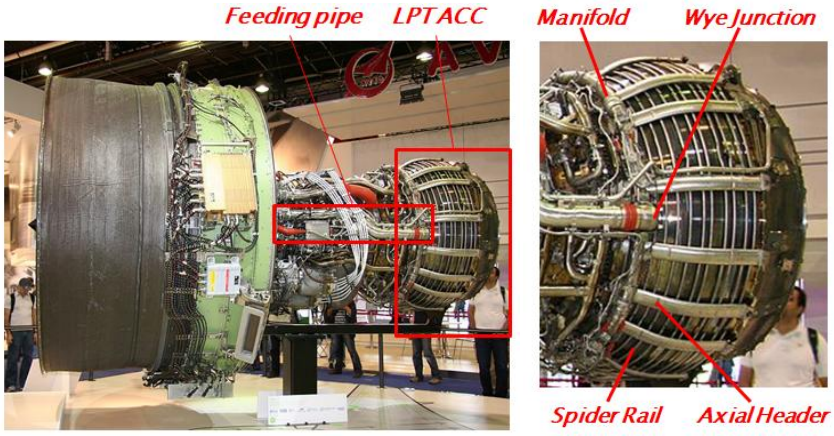

Figure 2.8 - Thermal LPT ACC system for large turbofan engines [17].

The impinging jets do not directly modify the LPT clearances, but operate in the way summarized in the scheme in Figure 2.9 [10, 18]. The ACC system is placed in the undercowl chamber, i.e. the space between the external engine cowl and the turbine case. The cooling jets impinge on the turbine case in a particular region, where the case is linked, by means of a bolt, to a mechanical component placed near the blade tips. As the jets cool down the impinged region, this region shrinks and the linking bolt moves towards the engine axis. Consequently, the

other stationary component, which faces the flow path and the blade tips, moves in the same direction, closing the clearance.

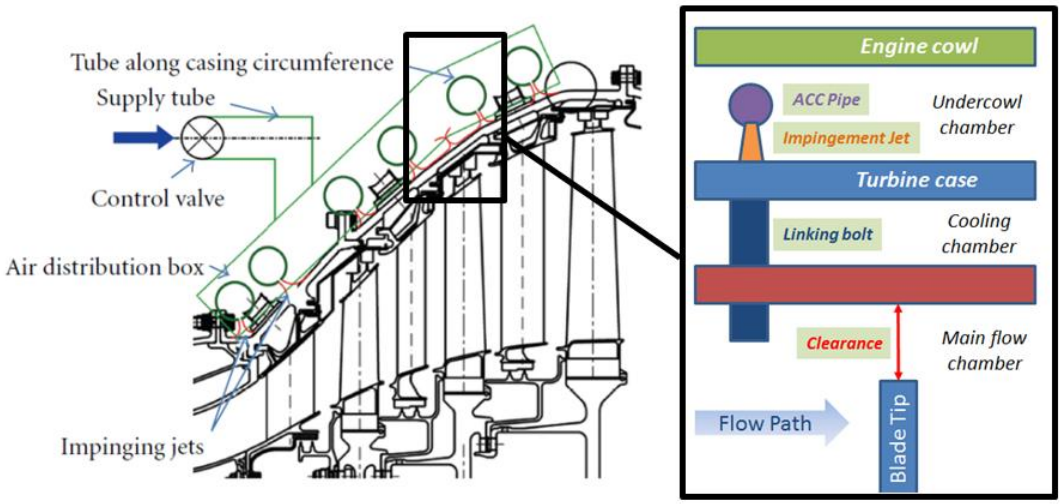

Figure 2.9 - LPT ACC operating scheme [18].

There are several topics concerning this architecture, each of them with a significant impact on the system performance:

- The choice of the air bleeding source (already discussed in the subparagraph 2.1.4);
- The pressure losses occurring along the pipelines;
- The heat pick-up occurring while delivering the cooling air;
- The case cooling by impinging jets.

2.2.1 Pressure Losses

All the other parameters being equal, the cooling by means of impinging jets is more effective when the pressure ratio available at the nozzle discharge is higher. This ratio is defined by two pressure values, which are influenced by a large number of factors:

$$\beta = \frac{p_{M,0}}{p_{UC}} \tag{2.1}$$

One of the two values is the ambient pressure in the discharge chamber, i.e. the undercowl static pressure p_{UC}. It depends on the operative conditions of the engine, which also influence the temperature and the entity of the cross flow. In the following, the cross flow can be intended as a generic stream of air, which flows axially in the undercowl chamber, towards the engine nozzle. The cross flow interacts with the impinging jets, deflecting their trajectories. The effects of this mechanism will be explained in detail in the part related to the jet physics. For the present discussion, it is important to know that the cross flow is originated by upstream flow leakages, due to other engine components or to other rows of impinging jets.

The other pressure value is the total pressure available upstream the discharge $p_{M,0}$. First, this value is determined by the total pressure available at the bleed source. For the present LPT ACC system, the air is bled from the fan. This means that the atmospheric air undergoes a low compression, thus, the total pressure at the ACC intake is not too much higher than the atmospheric value. However, during the long way from the system intake to the jet arrangement, the cooling air pressure is strongly affected by the pressure losses, related to the system design, and by the heat pick-up, due to presence of other engine components operating at high temperatures.

The pressure losses are typically divided into two contributions, the first one due to the friction, known as major head losses, and the second one related to the particular geometry of some components of the system, generally referred to minor losses. Since the ACC system behaves like a plenum and the flow velocity is small, the losses due to friction are lower than those related to the geometry of the system. Practically, the air velocity is maintained at a low value, preferable at a Mach number below 0.15.

Since the air, bled from the fan, has high velocities, it is necessary to slow it down to a condition that can be suitable for the ACC system. After the system intake, composed by a louver, there is a diffuser that converts the air dynamic pressure into static pressure, realizing the plenum condition. The conversion, for subsonic diffusers, is obtained by increasing the cross section at the outlet, so these elements have a conical shape. The efficiency of the conversion process can be expressed by means of the recovery factor R_F, defined as:

$$R_F = \frac{p_2 - p_1}{\frac{1}{2}\rho U_1^2} \tag{2.2}$$

where p is the static pressure, ρ is the air density, U is the air velocity and the subscripts 1 and 2 indicate the diffuser inlet and outlet, respectively. A high recovery factor is typical of high efficiency diffusers, and it is strongly affected by the component design. The Idel'chick's handbook provides a good estimation of the pressure losses related to the chosen design parameters [19].

On the other hand, the second contribution to the pressure losses includes all those discrete losses related to the geometrical configuration, i.e. the pipe shapes and the junctions among the several elements composing the ACC system. Since many mechanisms generating these pressure losses are well-known in the literature, one can use once again the Idel'chick [19] to determine the discrete loss coefficients.

Besides the available pressure ratio in the impingement region, the pressure losses also influence the circumferential flow distribution inside the ACC system. The desirable operating condition is to utilize amounts of cool air, which are roughly similar along the whole circumference of the turbine case. In order to ensure this condition, proper flow uniformity has to be guaranteed. This feature applies when the air splits from the manifold to the axial headers, from a single axial header to its spider rails and, finally, from a given spider rail to the

impinging nozzles. According to Miller [20], the flow uniformity is strictly related to the loss ratio. This value is defined as the ratio between the total area of the branches, through which the air exits, and the cross-section area of the pipe, which feeds all the branches. Another geometrical parameter that influences the flow uniformity is the length of the feeding pipe. Loss ratios, which are below 0.5, usually guarantee good flow uniformity, regardless of the pipe length. Otherwise, flow uniformity becomes poor, especially for very long feeding pipes.

An example can be done for the spider rails, which feed the impinging jets. While the cooling air is delivered to the nozzles, the pressure decreases along the spider rail. This means the available pressure drop for the last nozzles is lower than the one seen by the first nozzles. Obviously, this could affect the circumferential uniformity of the ACC system. In order to reduce this negative effect, it is important to choose, during the system design, the proper number of axial headers utilized to feed the spider rails. This choice is, basically, a trade-off between the overall weight and flow uniformity. Da Soghe et al [18] provide several design guidelines with their analyses, which are both numerical and experimental. In particular, they found that a ratio above five, between the area of the feeding pipe and the cumulative area of the impinging nozzles, guarantees a good uniformity in the mass flow split and, consequently, in terms of heat transfer. Another factor that improves the uniformity of the mass flow split is a higher pressure ratio.

Another parameter that could be included in the pressure losses, which the ACC system exhibits, is the nozzle discharge coefficient. However, this coefficient is influenced by other effects, which are related to the nature of the impinging jet, so it will be discussed in the paragraph dedicated to the jet physics.

2.2.2 Heat Pick-up

The air that is utilized to cool down the LPT case is bled from the fan at relatively low temperatures. However, the main pipeline of the ACC goes axially through the whole engine, passing near its core, where the temperatures can be very high. Flowing inside the pipes to reach the turbine casing, the air increases its temperature, because it adsorbs part of the heat released by the other engine components at higher temperatures. This phenomenon, known as heat pick-up, negatively affects the performance of the ACC system, since it reduces the efficacy of the cooling air delivered to the arrangement of impinging jets. The heat pick-up involves all the heat transfer mechanisms, which are well known in the literature [21].

To begin with, the engine components, which are near the ACC pipeline, transfer a certain amount of energy to its external wall by means of radiation. The heat flux is described by the Stefan-Boltzmann law:

$$Q_{R,E-P} = VF_{E-P}\varepsilon_E\sigma\left({T_E}^4 - {T_P}^4\right) \tag{2.3}$$

where $\sigma = 5.6703 \cdot 10^{-8}\ W/(m^2K^4)$ is the Stefan-Boltzmann constant, T_E is the temperature of a given engine component, T_P is the temperature of the ACC pipes, VF_{E-P} is the view factor of the engine case from the ACC pipes and ε_E is the engine case emissivity. A reasonable value of emissivity is 0.8, being these parts made in stainless steel exposed to a harsh environment, due to the high temperatures in the surroundings [22].

Convection is involved between the external ACC pipe and the air flow inside the undercowl chamber. The heat transfer occurring during this phase can be described with good accuracy by using the correlations for external flows, which have been widely well-known in the literature [21].

Then, the heat flux, which has been absorbed by the outer wall of the ACC pipe, is transferred to the inner wall by conduction. This mechanism is described by the Fourier's law, where the thermal conductivity of the stainless steel is a function of the metal temperature. This temperature dependence has been analyzed in many literature studies and, for the present work, the graph reported by Incropera and his coauthors [23] has been chosen as a reference.

The last step of the heat pick-up mechanism consists in the heat transfer by convection between the cooling air and the inner walls of the ACC pipes. The Nusselt number has been calculated by means of a Dittus-Boelter correlation, which has been corrected with a term including the ratio between the pipe hydraulic diameter and its length [24]:

$$Nu = 0.023 \cdot Re^{0.8} Pr^{0.33} \left[1 + \left(\frac{d_h}{L}\right)^{0.7}\right] \tag{2.4}$$

where d_h and L are the pipe hydraulic diameter and length, respectively.

2.3 Impinging Jets

This last paragraph of the literature review concerns the several topics related to the impinging jets utilized in an ACC system. After a short overview about the physics of the single jet, those phenomena, which occur when multiple jets and cross flows are involved, are described. Then, the most significant correlations are shown, which have been proposed, in the literature, to characterize the discharge coefficient and the heat transfer of impinging jets. Finally, the methods that can be utilized to enhance the heat transfer on the impinged surface are discussed.

Before starting with the literature review, it is useful to define some geometrical parameters that will be introduced later (they are also shown in the Figure 2.10):

- Although slot jets are very common in scientific publications, they are mainly adopted in cooling for electronics, while the nozzles of the ACC system are circular. Consequently, all the references that have been listed in the present work mainly concern circular jets. The nozzle diameter is d.
- The length of the nozzle is *t*.

- The vertical distance between the nozzle and the target surface is S_y.
- The streamwise spacing between two rows of jets is S_x. The rows can be arranged in patterns that can be either in-line or staggered (in the latter case, with a certain spanwise distance i). Typically, the jet arrangement of an ACC system exhibits single o double rows of impinging jets per spider rail, so the value of S_x can be significantly high, compared to the jet diameter.
- The spanwise spacing between two adjacent jets is S_z. The three parameters S_x, S_y and S_z are more commonly utilized in a non-dimensional form, divided by the jet diameter.

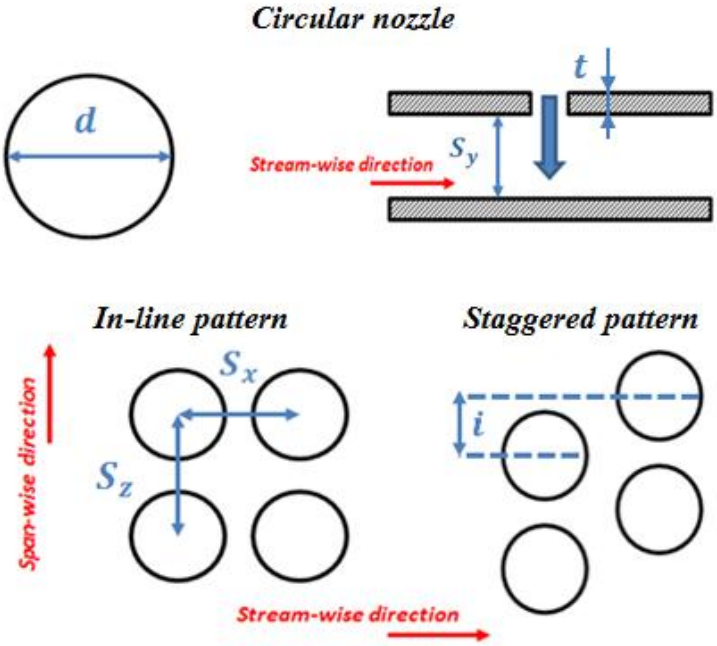

Figure 2.10 - Geometrical parameters of the impinging jet arrangement.

2.3.1 Physics of the Single Jet

Referring to a single jet, impinging on a target surface, the observed flow field can be divided into several regions, shown in the Figure 2.11 [25].

The region of flow establishment, or region I, extends from the nozzle exit to the apex of the potential core. This is the flow portion characterized by a constant velocity, equal to nozzle exit value. So, the region I exhibits a constant axial velocity in the jet centerline and has an extension of about six or seven jet diameters.

Once the potential core is exhausted, the established flow region starts. Here, the velocity at the jet centerline gradually decreases under the effect of the turbulent dissipation, with a value that is inversely proportional to the distance from the nozzle.

The next region, where the jet reaches the target surface, is the stagnation region. This portion is characterized by the deflection of the jet from an axial to a tangential direction.

Once the jet has been deflected, the wall jet region develops. Here, the heat transfer efficacy is primarily determined by the nature of the boundary layer (laminar or turbulent) and by the vortex large-scale structures.

These structures, which originate in the jet peripheral region, have two main effects on the flow field. The first effect, occurring in both free and impinging jets, is the vortex-induced total temperature separation. This effect consists in the appearance of regions with different values of total temperature around those vortices, which develop in the peripheral region of the jet, and is due to the entrainment of air external to the jet. This process, unsteady and inviscid, can be explained recurring to the adiabatic energy equation for a perfect gas:

$$c_p \frac{dT_t}{dt} = \frac{1}{\rho}\frac{\partial p}{\partial t} \tag{2.5}$$

This equation relates the total temperature variation of a particle, along its path, to the temporal variation of the static pressure, which depends on the relative movements between the particle and the vortex core structure.

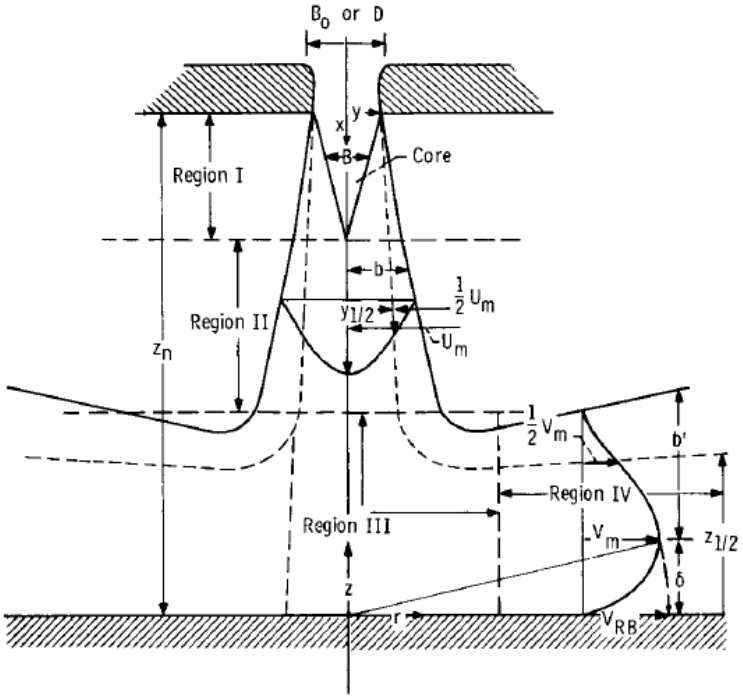

Figure 2.11 - Single impinging jet: jet development regions [25].

As shown in the Figure 2.12 [26], there are several possibilities for the fluid particles:

- The A-type particles, entrapped by the vortex rings, rotate around these vortices and move downstream. As the particle follows its path, it reaches point 1, moving apart the jet center. Here, its pressure gradient is negative, so the total temperature decreases. As the particle moves back towards the jet center (point 2), the vortex, which is moving downstream, affects it with a positive pressure gradient, thus, the total temperature increases. In

other words, the total temperature reaches a maximum near the jet center and a minimum near the jet edge.

- The B-type particles are also entrained from the external ambient. As the vortex moves downstream, the particles are shifted towards the jet centerline, where their total temperature increases.
- The particles of the group C are near the jet center and they are practically unaffected by the vortex structures.

Consequently, the region near the nozzle, is characterized by low entrainment, where the prevailing effects are those due to the C particles near the center and to the A particles in the periphery, with excesses and deficits in the total temperature. Further downstream, the entrainment increases and the B particles increase the jet center total temperature. Around this region there is an annular region of lower total temperature.

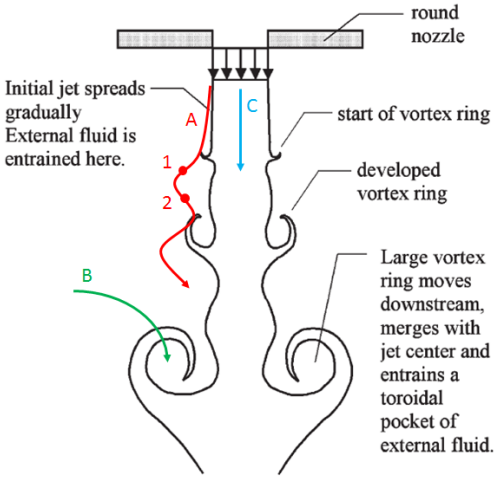

Figure 2.12 - Free jet: entrainment of external fluid [26].

The second effect related to the vortex structures is the vortex-induced unsteady separation and is typical of impinging jets [27]. When a vortex ring formed at the nozzle (primary vortex) approaches the target surface, its unsteady adverse pressure gradient may induce the separation of the wall boundary layer, which forms a secondary counter-rotating vortex (see Figure 2.13). This vortex, since it moves downstream along the plate in phase with the primary vortex, creates an ordered unsteady flow structure. This phenomenon, independent of Mach and Reynolds numbers, strongly depends on the S_y/d ratio:

- For small values of this ratio, the primary vortex reaches the wall near the stagnation point. Here, the boundary layer has a low momentum, so the adverse pressure gradient around the primary vortex is strong enough to induce the boundary layer separation.
- As the S_y/d ratio increases (approximately beyond the potential core region), the primary vortex approaches the wall far downstream the stagnation point, where the boundary layer momentum is higher and the secondary vortex generation does not occur.

A strong vortex-induced separation worsens the heat transfer, not only in quantitative terms, but also in quality, since the appearance of unsteady structures

reduces the heat transfer uniformity over time. Despite the vortex-induced separation is independent of Reynolds number, the primary vortex structure, which generates this effect, may affect the vortex frequency. This parameter plays a fundamental role on how the entire flow field develops and its control could improve the performance of jet cooling techniques, as will be discussed later in this subparagraph.

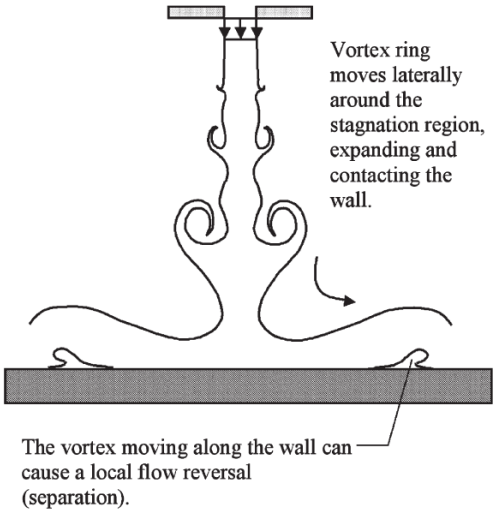

Figure 2.13 - Impinging jet: vortex-induced separation [27].

2.3.2 Multiple Jets and Cross Flow

When the impinging jets are more than one, they interact, originating a complex flow field (see Figure 2.14, [28]). The observable flow structures mainly depend on the geometrical parameters characterizing the jet arrangement, i.e. the values of the spacing in the three spatial directions, divided by the jet diameter. Multiple jets can be arranged in rows or in arrays, when multiple rows of jets are put together. The main advantage of multiple-jet cooling is a more uniform heat transfer over the target surface. However, if compact arrays are considered, higher mass flow rates are required for the system operation.

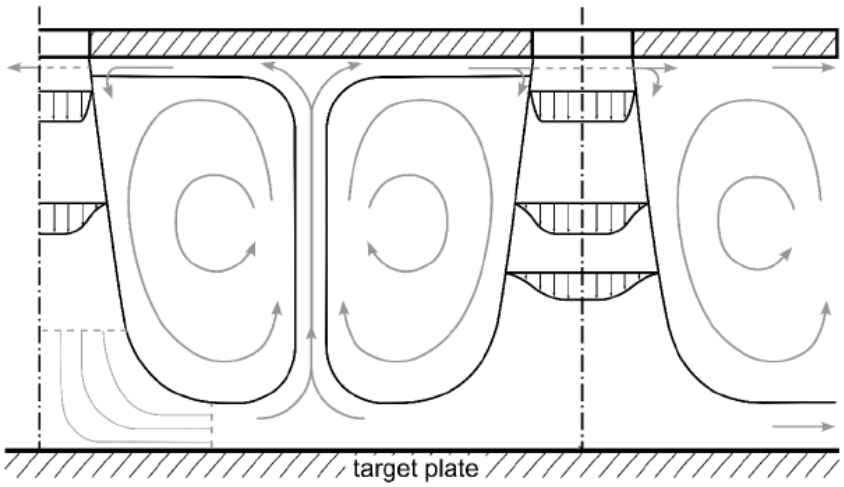

Figure 2.14 - Interactions between two adjacent impinging jets [28].

The presence of multiple jets also generates a cross flow, since the spent air of upstream jets may interact with the other impinging jets. Actually, referring to an ACC system placed inside the undercowl chamber, the cross flow may receive further contributions by various engine leakages. Whatever the origin of the cross flow, its effect is to deflect the trajectory of the centerline of the jet, with the consequent displacement downstream of the impingement point. This deflection results in a non-orthogonal angle of impingement on the target surface, which reduces the effectiveness of the heat transfer, as Perry found in his study on oblique impinging jets [29]. A large number of publications, describing jets that interact with an external cross flow, are available in the literature.

Karazogian [30] describes the main flow structures that could be observed when a free jet interacts with a cross flow, as shown in Figure 2.15. A large structure, known as counter-rotating vortex pair (CVP), is the prevailing phenomenon in the jet cross section. Other mechanisms of interaction are the shear layer vortices, which become more pronounced as the jet flows downstream, and the horseshoe vortices, which wrap the entire jet column. Finally, there are also wake vortices that introduce fluid from the wall boundary layer into the jet.

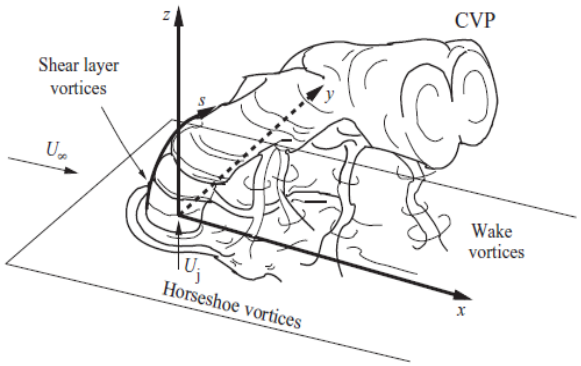

Figure 2.15 - Jet in a cross flow: flow structures [30].

When the cross flow interacts with an impinging jet or, as in the majority of the practical applications, with an array of impinging jets, it affects the effectiveness of this cooling technique. In particular, a strong cross flow may deflect the jet away from the target surface, especially when the nozzle-to-plate distance is large. As Florschuetz and Su [31] found in their experimental studies, the cross flow has two effects. It enhances the heat transfer through forced convection, but it also deflects the jets, thus reducing their effectiveness. In order, to compare the strength of the cross flow to the one of the jet, the authors introduced the cross-flow-to-jet mass velocity ratio:

$$G_c/G_j = (\rho u)_c/(\rho u)_j \tag{2.6}$$

The condition $G_c/G_j = 0$ represents the case without cross-flow, while in the range $0 < G_c/G_j < 1$ the jet is stronger than the cross flow. Here, the jet deflection may occur, resulting in a non-symmetric distribution of the streamwise-average Nusselt number, with the stagnation point located downstream the nozzle.

Generally, this effect is detrimental for the heat transfer, thus the Nusselt number decreases as the cross flow increases. In the range $G_c/G_j > 1$, the cross flow is stronger than the jet, eventually leading to a condition where the forced convection due to the cross flow becomes prevalent and the Nusselt number increases again. Besides this general trend, the authors observed that in presence of weak cross flow, the Nusselt number can be higher than the value recorded in the absence of cross flow. This behavior can be explained considering that the first effect of the cross flow overcomes the second negative contribution related to the jet deflection.

Similar conclusions have been observed by Goldstein and Behbahani [31], who performed experimental tests on a jet impinging to a normal surface, placed at $S_y/d = 6$ and $S_y/d = 12$, under several schemes of cross flow that have been defined in terms of jet-to-cross-flow mass velocity ratio, *MVR*:

$$MVR = (\rho u)_j/(\rho u)_c = 1/(G_c/G_j) \tag{2.7}$$

The authors found that, under moderate cross flow ($MVR > 9$), the maximum Nusselt number increases, compared to the case without cross flow, for the configuration with $S_y/d = 6$. The Reynolds number for their experiments was in the range $33000 < Re_j < 120000$.

Experimental studies on the deflection of a free jet under external cross flow have been carried out by Kamotani and Greber [32]. They developed two correlations to define the jet trajectory, both in terms of velocity and temperature.

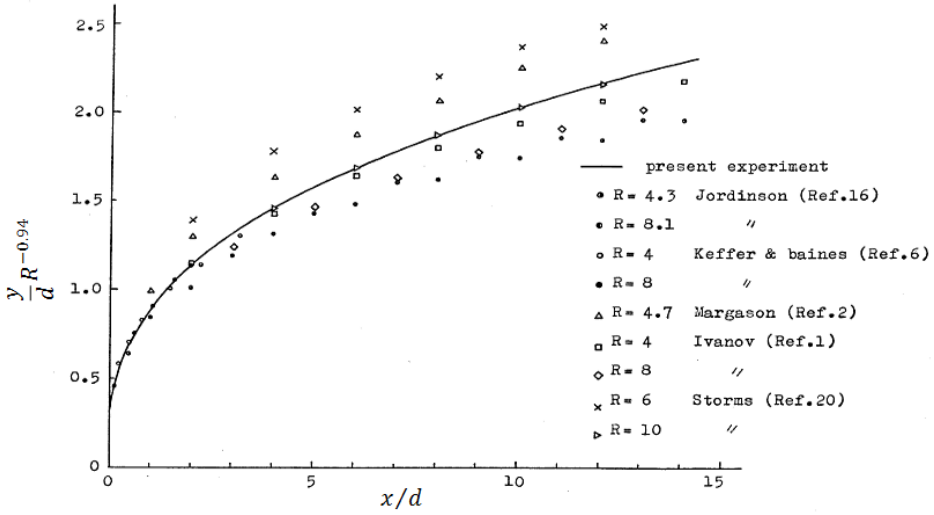

Figure 2.16 - Jet in a cross flow: velocity trajectories defined by several authors in the literature (the present experiment is by Kamotani [32]).

The authors compared their results to other literature works, noting that there was no large spread among the several correlations proposed until then, as shown in Figure 2.16. An effective way to represent the velocity trajectories is indeed to scale them with the jet diameter. Here, x and y are the axial and vertical coordinates of the jet centerline, respectively, while $R = u_j/u_c$ is the velocity ratio between the jet and the cross flow velocity.

According to the authors, the developed correlations not only apply to free jets, but also to other configurations, such as impinging jets. However, jet impingement applied to turbine case cooling usually involves stiffer jets, with higher momentum than those cases that have been analyzed in their work. When an ACC system is designed, it is important to provide adequate pressure to the impinging jets, since this value determines the exit velocity of the air through the nozzles. Higher exit velocities guarantee stiffer jets in the presence of strong cross flows.

2.3.3 Jet Performance: Parameters and Correlations

The performance of an impinging jet can be quantified by means of those non-dimensional parameters that have been widely utilized in the literature to describe fluid-dynamics and heat transfer phenomena in the most general way.

For the impinging jet, the definition of the Reynolds number, which compares the inertial forces to the viscous contribution, is based on the nozzle diameter as the characteristic length:

$$Re_j = \frac{\rho_j u_j d}{\mu_j} = \frac{4\dot{m}_j}{d\pi\mu_j} \tag{2.8}$$

In order to define the Reynolds number for the jet, it is needed to know the value of the product $\rho_j u_j$ or (it is basically the same) of the nozzle mass flow rate $\dot{m}_j$. The latter can be seen as the *real* mass flow rate, to be compared with an *ideal* value:

$$C_D = \frac{\dot{m}_j}{\dot{m}_{j,IDEAL}} \tag{2.9}$$

In this relation, $\dot{m}_{j,IDEAL}$ is the ideal mass flow rate, i.e. the value flowing through an orifice under isentropic conditions. It can be calculated by using the formulation of Saint Venant [34]:

$$\dot{m}_{j,IDEAL} = \frac{p_{j,0} \cdot A}{\sqrt{T_{j,0}}} \sqrt{\frac{2\gamma}{R(\gamma-1)}\left[\left(\frac{1}{\beta}\right)^{2/\gamma} - \left(\frac{1}{\beta}\right)^{(\gamma+1)/\gamma}\right]} \tag{2.10}$$

The ratio between the two mass flow rates is the discharge coefficient C_D. This value can be determined by experiments or estimated with good accuracy recurring to several literature correlations. For an impinging jet under cross flow, the discharge coefficient usually depends on the pressure ratio β (see Equation 2.1) and on the momentum ratio between jet and cross flow.

Florschuetz and Isoda [35] analyzed several configurations of jet arrays. For each setting, they defined a constant value of the discharge coefficient. Then, when the cross flow strengthened, they noticed that the C_D decreased as the G_c/G_j ratio became higher.

Schultz et al [36] studied the behavior of film cooling holes. In their work, they investigated several parameters that could affect the discharge coefficient, such as the Mach numbers of the cross flow and of the hole feeding line, the orientation of the jet (i.e. the angle of the jet with respect to the feeding line) and the angle between the jet and the target surface. The experimental data have been obtained for different values of β. Basically, higher values of the pressure ratio improve the discharge coefficient, while a stronger cross flow has the opposite effect.

Andreini and Da Soghe [37] developed a correlation valid for an ACC system, where the discharge coefficient is composed by two contributions:

$$C_D = C_{D,S} C_{D,C} \tag{2.11}$$

The first one, $C_{D,S}$, can be considered the static part, which includes the effect of the pressure ratio, in the absence of cross flow. This term is also influenced by a function depending on the nozzle length to diameter ratio t/d [38]. The second contribution, named $C_{D,C}$, is related to the cross flow and it is expressed as a function of the mass velocity ratio indicated in Equation 2.7. This correlation has also been validated on the experimental data produced by Schulz [36].

Once one of these correlations has been utilized to calculate the discharge coefficient, Equation 2.9 can be rearranged in order to obtain the real mass flow rate as the product between the isentropic mass flow rate and the C_D.

The other Reynolds number that could be utilized in these analyses is the one defined for the cross flow. Similarly to the value, which is based on the jet, it is defined by using the hydraulic diameter d_{Hc}, which represents the section of the undercowl chamber:

$$Re_c = \frac{4\dot{m}_c}{d_{Hc}\pi\mu_c} \tag{2.12}$$

The second non-dimensional number that will be useful to characterize the jet is the Prandtl number. It expresses which one, between the momentum and the energy transport, is preponderant in the hydrodynamic boundary layer:

$$Pr_j = \left(\frac{c_p \mu}{k}\right)_j \tag{2.13}$$

Since air is the fluid involved in the present study, its Prandtl number, which depends on temperature and weakly on pressure, can be determined by using the tables that can be easily found in the literature [39].

Another common non-dimensional parameter, useful to characterize the heat transfer during the impingement on the target surface, is the Nusselt number, whose most general expression is:

$$Nu = \frac{HTC\ d}{k} \tag{2.14}$$

Here, *HTC* is the convective heat transfer coefficient, which is evaluated as:

$$HTC = \frac{q}{(T_w - T_{j,0})} \tag{2.15}$$

Besides the most generic definition provided by Equation 2.14, the Nusselt number for impinging jets can be estimated by using one of the many correlations, which basically show this structure:

$$Nu = c\ Re_j^m Pr_j^n \tag{2.16}$$

Among all the available literature studies, it is important to choose the most suitable one, because each correlation may have a limited range in terms of Reynolds number, nozzle-to-plate distance and (when multiple jets are considered) spacing between jets. An interesting survey about the correlations developed for impinging jets has been provided by Livingood [25]. This report comprehends many of the studies then available on single or multiple jets. One example is the research performed on the single impinging jet on a heated surface by Gardon [40].

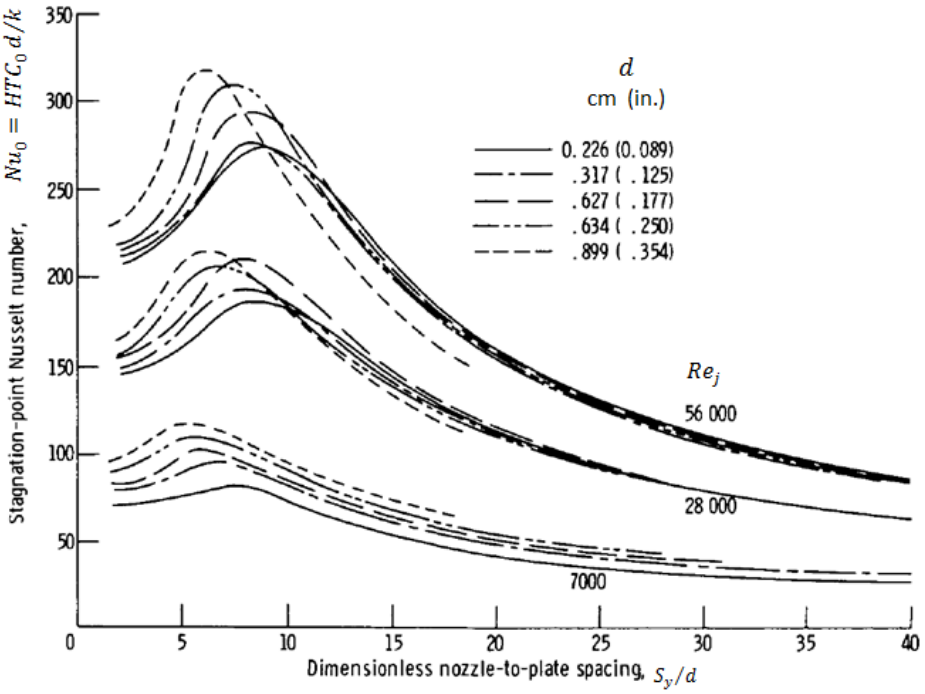

Figure 2.17 - Impinging jet: Nusselt number at stagnation point against S_y/d, at different Reynolds numbers [40].

As shown in Figure 2.17, the author investigated the behavior of the Nusselt number at the stagnation point, Nu_0, while changing the jet diameter, the Reynolds number and the nozzle to plate spacing. The peak roughly occurred in the range $4 \leq S_y/d \leq 8$, shifted lower S_y/d values for larger diameters. While

the Reynolds number had no significant impact on the peak position, it was recorded that higher Reynolds numbers (i.e. higher feeding pressures, when the jet diameter is fixed) improved the heat transfer.

The author also analyzed the radial shape of the Nusselt number, finding that the curve presented the local maxima for $S_y/d < 4$, instead of the typical structure with a peak located at the stagnation point (see Figure 2.18).

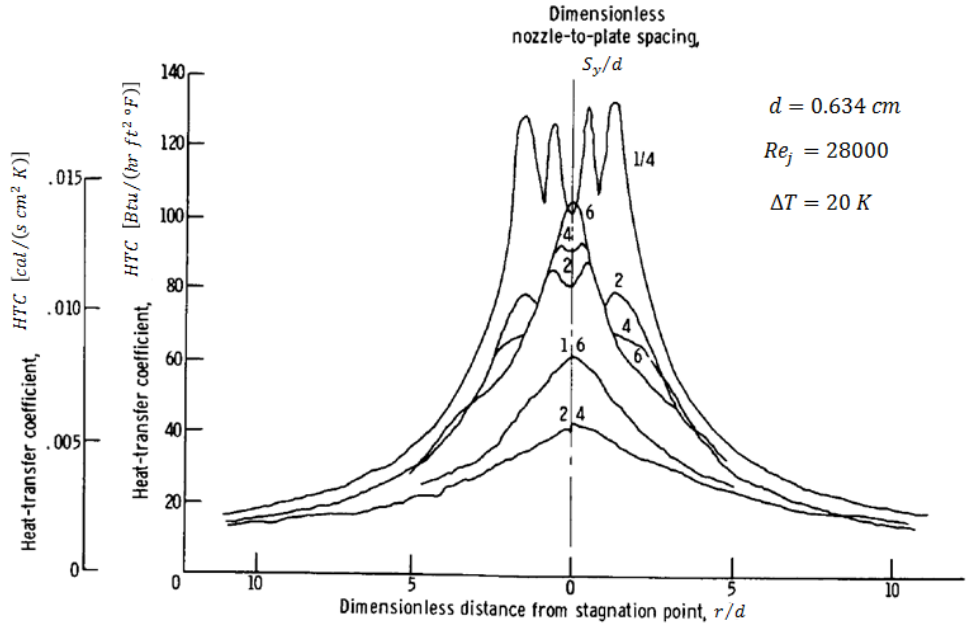

Figure 2.18 - Impinging jet: radial Nusselt number against S_y/d [40].

Goldstein et al [41] explained the reason for this higher Nusselt number in the peripheral region of the jet, at small values of S_y/d. Since the target surface is still located inside the potential core region of the jet, there is a vortex ring that wraps the jet. As the S_y/d ratio increases, the heat transfer remains high near the stagnation point, while it decreases in the peripheral region, since the vortex becomes weaker.

When multiple jets are involved, the heat transfer is influenced by both the jet-to-jet interactions, which depend on the spacing among the jets and between the jets and the target surface, and the cross flow generated by the spent air of the other jets. Florschuetz et al carried out extended investigations [33, 42], in order to develop Nusselt number correlations capable to describe the heat transfer of jet arrays under cross flow. Their research also included the effect related to the choice of the array pattern, which could be in-line or staggered. The proposed correlations allowed calculating the average Nusselt number on the surface cooled down by using the jet array. They both had the form shown in Equation 2.16, where the term c is a function of the array geometry and of the G_c/G_j ratio. The correlation developed in 1980 [33] is detailed, but also quite complicated to be utilized:

$$Nu = A\left\{1 - B\left[\frac{S_y}{d}\frac{G_c}{G_j}\right]^n\right\} Re_j^m Pr_j^{1/3} \qquad (2.17)$$

where all the parameters A, B, m, n are functions of coefficients, which are listed in tables in the authors' publication:

$$A, B, m, n = C\left(\frac{S_x}{d}\right)^{n_x}\left(\frac{S_z}{d}\right)^{n_z}\left(\frac{S_y}{d}\right)^{n_y} \tag{2.18}$$

The same authors proposed, the following year, a simpler correlation [42]:

$$\frac{Nu}{Nu_1} = 1 - C\left(\frac{S_x}{d}\right)^{n_x}\left(\frac{S_z}{d}\right)^{n_z}\left(\frac{S_y}{d}\right)^{n_y}\left(\frac{G_c}{G_j}\right)^{n} \tag{2.19}$$

In the experiments performed by the authors, the cross flow was entirely generated by the spent air from the jets. The value Nu_1 is indeed the Nusselt number for the first row of the jet array, which is not affected by the cross flow. It has been utilized to normalize the overall Nusselt, *Nu*, and can be calculated as:

$$Nu_1 = 0.363\left(\frac{S_x}{d}\right)^{-0.554}\left(\frac{S_z}{d}\right)^{-0.422}\left(\frac{S_y}{d}\right)^{0.068} Re_j^{0.727} Pr_j^{1/3} \tag{2.20}$$

2.3.4 Heat Transfer Enhancement: Flow Control

Jets are unsteady phenomena involving complex vortex structures. A better knowledge of these mechanisms may allow to control and to utilize them in order to improve the performance of the jet arrangement, in terms of heat transfer.

As discussed in the previous parts (in particular, with the references [27, 41]), the S_y/d ratio appears to be critical in determining the generation and the strength of the secondary vortex, an unsteady structure that periodically hits the peripheral region of the target surface. In this mechanism, the S_y/d ratio is not the only important parameter. The strength of the secondary vortex is indeed related to the frequency of the primary vortex, which forms in the jet periphery, where the entrainment occurs (see the Figure 2.19 [43]).

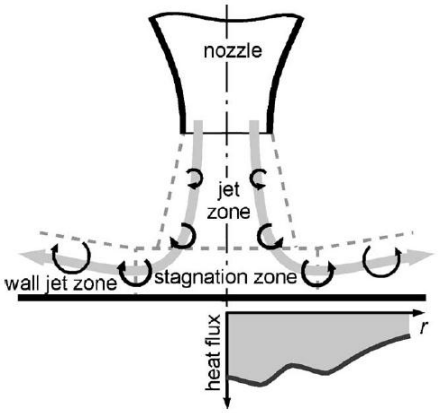

Figure 2.19 - Scheme of the vortex structures in an impingement jet [43].

Under the right frequencies, two primary vortices may merge to form a larger structure, a phenomenon known as vortex pairing, whose consequence is the

generation of a strong secondary vortex that worsens the heat transfer on the target surface. On the contrary, the prevention of the vortex pairing, which can be achieved by using the jet control techniques, improves the heat transfer uniformity near the stagnation point. In the literature, two typologies of jet control techniques have been proposed (see the Figure 2.20):

- The acoustic jet excitation, that is, to force the jet with acoustic waves generated into an upstream chamber [43 - 45].
- The secondary shear flow control, which consists into adding a secondary flow around the main jet, by means of a concentric nozzle [45].

Liu and Sullivan [44] performed experimental tests on the jet excitation technique. By setting the jet excitation frequency, they observed the effects that this choice had on the secondary flow structure. Their result was that the heat transfer uniformity in the region near the stagnation point, where $1 \leq r/d \leq 2$, could be improved or worsened (as shown in the Figure 2.21, where f_N and f_e are the natural and the excitation frequencies, respectively). In particular, a better wall heat transfer uniformity has been achieved when the excitation frequency generated a non-stable vortex pairing. By breaking the regular formation of a large primary vortex, the secondary flow turned out to be a sort of *lump-eddy*, i.e. a structure with random small-scale turbulence features, thus, better heat transfer capabilities, rather than a well-organized sequence of vortices.

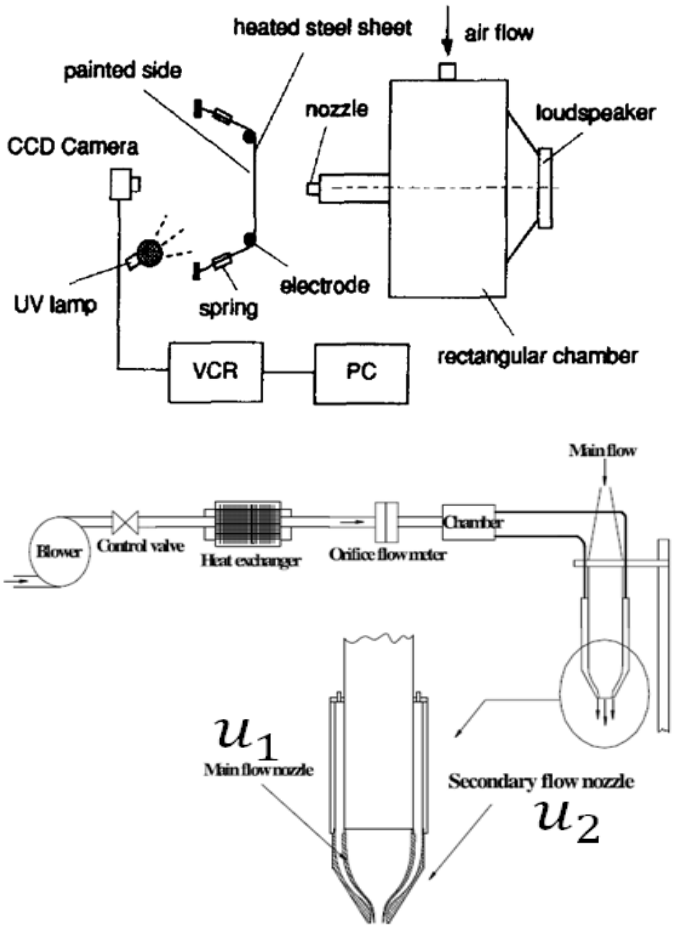

Figure 2.20 - Experimental apparatus for jet flow control: acoustic excitation (top) and shear flow control (bottom) [45].

The authors explained this phenomenon by considering that the wall heat flux is made of three contributions. The first one is the heat flux produced by the mean flow, which does not include the part associated with the turbulence, even if it implicitly depends on it, since the turbulent fluctuations may change the mean flow. Then, the heat flux due to the turbulent fluctuations is related to the two other effects. One part is generated by the organized vortices, while the last one is induced by the incoherent flow structures.

On one hand, the organized vortices in the wall region entrain the colder ambient fluid into the boundary layer and eject the hot fluid away from the wall. So, the wall is cooled and this contribution enhances the local heat transfer. On the other hand, the ambient fluid entrained by these coherent vortices has a low momentum, so the mean shear rate near the wall decreases and the separation eventually occurs, if the vortices are strong enough. This contribution associated to the coherent structures has a detrimental effect on the term that represents the mean heat flux. On the contrary, the small-scale random turbulence near the wall, due to the incoherent vortices, always increases the wall heat transfer. Overall, the balance of these three parts results in an improved or worsened heat transfer.

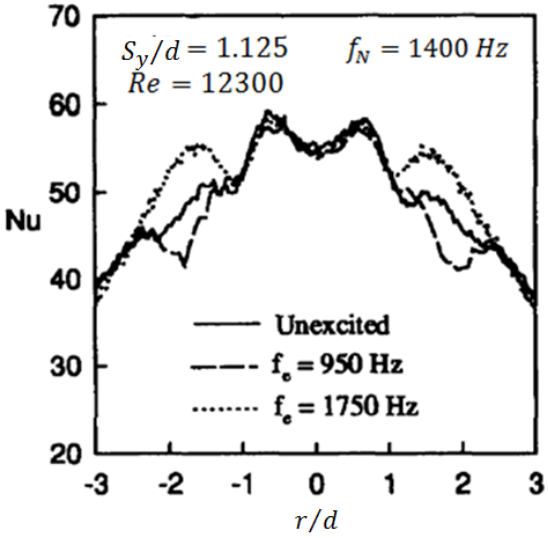

Figure 2.21 - Effect of jet excitation on the radial Nusselt number [44].

Hwang et al. [45] provided experimental data for both the acoustic excitation and the shear flow control techniques.

The acoustic jet control was performed considering several forcing frequencies, compared to jet without excitation. The data have been analyzed by using the Fast Fourier Transform (FFT). The FFT analysis of the non excited jet revealed a fundamental frequency associated to the primary vortex generation and a sub-harmonic related with the vortex pairing phenomenon. These peaks were more relevant at very low S_y/d values, disappearing around $S_y/d = 6$. With this configuration, the frequency distribution appeared to be more uniform.

When the excitation frequency was introduced, the obtained result was that the jet potential core became longer, if the excitation frequency was chosen to suppress the vortex pairing and the jet development, while the turbulence intensity was lower. However, at lower S_y/d ratios, the excited jet, despite the extended

core, showed a lower Nusselt number at the stagnation point, due to the low turbulence intensity. On the contrary, at higher spacing, the effect of a more extended potential core prevailed, with higher heat transfer.

The authors also tested the secondary shear flow control, by using a smoothly contoured nozzle, in order to obtain a uniform velocity profile (see the Figure 2.20, bottom). The following relation, between the velocities at the exit of the two concentric nozzles, is useful to understand the obtained results:

$$P_F = \frac{u_1 - u_2}{u_1 + u_2} \tag{2.21}$$

Here, u_1 represents the average exit velocity at the main nozzle, while u_2 is the same value for the secondary, or concentric, nozzle. This means that, when P_F is lower than 1, the secondary air jet is in co-flowing conditions, thus the two air flows are in the same direction. For P_F higher than unity the second nozzle is in counter-flowing (air suction) conditions. The condition $P_F = 1$ is the case with no secondary flow. The authors examined both the co-flowing and counter-flowing conditions. Compared to case $P_F = 1$, the co-flowing secondary flow delayed the disappearance of the potential core. In other words, the formation of outer vortices, between the secondary air flow and the ambient, inhibited the vortex pairing and the entrainment of the ambient air for the main flow. On the contrary, the counter-flowing condition promoted a stronger shear between the main and the secondary flows, anticipating the main flow development, with the consequent disappearance of the potential core and the worsening of the heat transfer.

2.3.5 Heat Transfer Enhancement: Case Roughening

Despite the interesting results, the jet control techniques appear to be not so easily applicable to the ACC impingement system. Moreover, it should be noted that, in the applications seen in subparagraph 2.3.4, the ambient temperature is similar to the jet temperature, while the target surface is heated up. Consequently, the entrainment of external fluid in the region near the impingement surface exerts a positive contribution in terms of cooling effectiveness. However, in the application of a LPT ACC system, the external flow (i.e. the undercowl flow) is typically hotter than the cooling air injected through the nozzles. For this reason, an increased entrainment of external air can lead to a worsening of the heat transfer on the impingement surface. Overall, the utilization of flow control techniques could be more indicated for other applications, rather than the one studied in the present work.

An alternative method, which seems to be promising in terms of heat transfer enhancement, is the use of roughening elements on the case surface, in the impingement region. In literature, there are a large number of studies about impinging jet on roughened target surfaces.

El-Gabry and Kaminski [46] analyzed an array of impinging jets on a target surface with random roughness. The experimental tests have been carried out at

different Reynolds number, jet angles (at 90, 60 and 30 degrees with the target surface) and S_y/d ratios (equal to 1 or 2, with jets close to the target surface), comparing the roughened surface to the smooth one. In each condition, the former performed better than the latter, with higher average Nusselt number and a more uniform heat transfer, as shown in the Figure 2.22.

Taslim et al [47] performed a set of experimental tests, on a rig representing the airfoil leading edge. The objective was to increase the heat transfer achievable by using impinging jets. The authors proposed several geometries, such as conical bumps, to increase the heat transfer area on the impinged surface. The obtained results showed that heat transfer was generally enhanced by an amount similar to the increase in terms of wetted area.

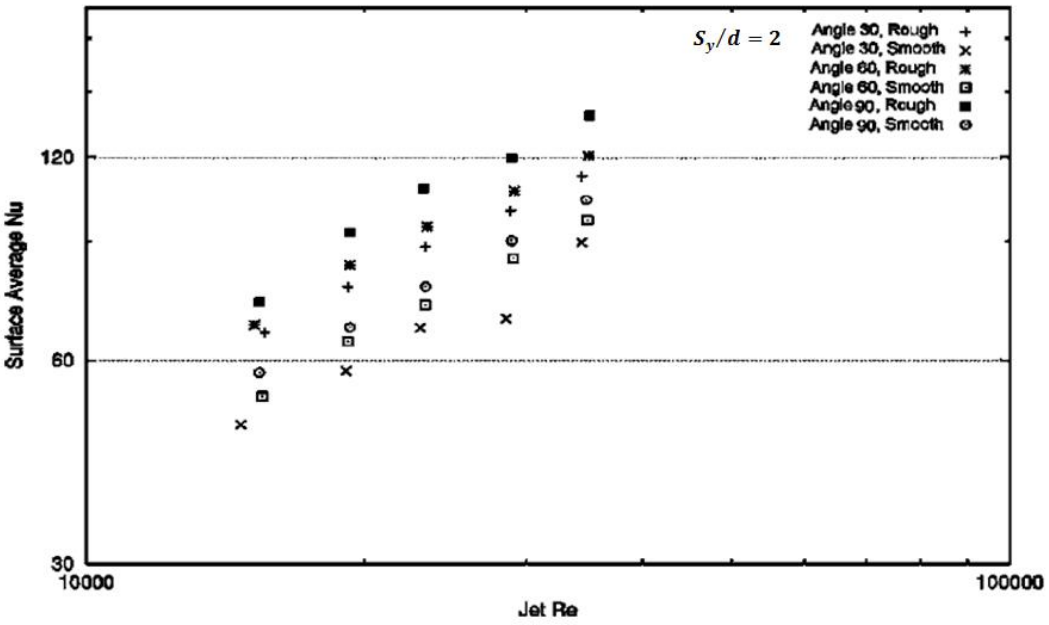

Figure 2.22 - Effect of roughness on the average Nusselt number [46].

Kanokjaruvijit and Martinez-Botas [48] studied the heat transfer occurring when an array of jets impinged on a dimpled surface, under different cross flow schemes. The impacts related to the spacing of the array and to the dimple geometry have been investigated. The authors found that the presence of dimples enhanced the heat transfer of the order of fifty percent, depending on the Reynolds number, the cross flow scheme and the dimple geometry. In particular, shallow dimples exhibited higher average Nusselt number than the deeper ones. This result was explained with two reasons. The first one is that shallow dimples were at a smaller distance from the nozzle, thus, the impinging jets had higher momentum. The second reason is that deep dimples promoted larger recirculation zones, while, for the shallow ones, it was easier to transfer downstream the vortices that originated during the impingement.

Gau and Lee [49] investigated the behavior of a slot jet impinging on a target surface with several configurations of ribs (see the scheme in the Figure 2.23). In particular, the ratio between the slot width and the rib height was found to be significant in determining an improvement or a worsening of heat transfer, compared to the flat surface. Generally, in the cavity formed between two

adjacent ribs, a bubble of stagnant air was observed. This bubble prevented the jet flow two impinge inside the cavity, reducing heat transfer. However, when the flow became turbulent, the jet flow was able to penetrate inside the cavity. The air circulation that was created led to higher heat transfer than the flat surface. It turned out that a small rib height, compared to the slot width, promoted the turbulence and enhanced heat transfer.

Other studies have also been performed on the rib shape, such as Yu et al [50]. They investigated the effect of W-shaped micro-ribs on heat transfer of a target surface, impinged by a dense jet array, for applications in electronics cooling (see the Figure 2.24). The proposed pattern increased the overall Nusselt number by 8%, despite the wetted area increased by only 5.4%.

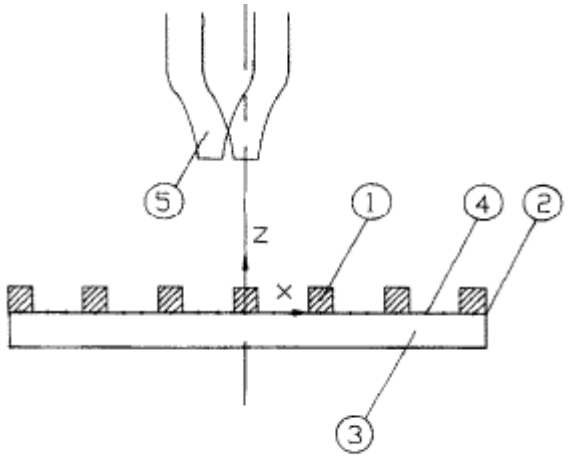

FIG. 1. Schematic of apparatus: (1) square rib, (2) stainless steel foil, (3) Plexiglas plate, (4) thermocouples and (5) rectangular nozzle.

Figure 2.23 - Experimental apparatus utilized by Gau and Lee [49].

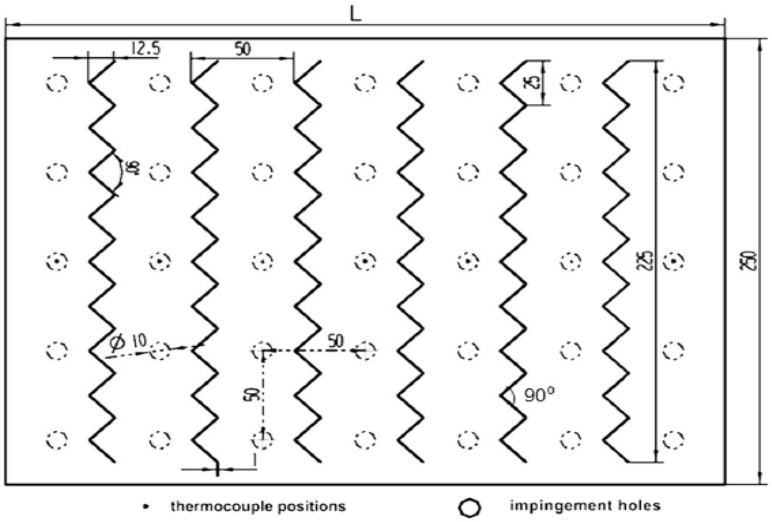

Figure 2.24 - Experimental apparatus utilized by Yu et al [50].

Chapter 3

ACC Fluid-Dynamics

The first step of the PhD activity consisted into analyzing how the mass flow rate was affected by the main design parameters of the ACC system. Since the objective of the research is to improve the efficiency of this system during cruise (i.e. the longest among the phases of a flight mission, at least for a civil aircraft), the following analyses always will refer to this phase, in terms of boundary conditions.

To accomplish this task, a Design of Experiment (DoE) was utilized, carrying out a set of numerical simulations with a flow network solver, which was capable to replicate the main features of the air flow inside the ACC pipes. The results, which have been provided by the simulations, have been compared in terms of mass flow rate, evaluating the effects of the several parameters analyzed, while fixed boundary conditions have been chosen. In particular, the robustness of the ACC system has been tested under changing design conditions.

3.1 Numerical Modelling

The numerical model has been developed by using a commercial software that performs 1D analyses of internal flows in complex pipe systems. The software calculates the flow characteristics inside the pipes and returns a pressure field that ensures the continuity equation.

More in detail, the pipes are modeled as 1D elements with a given length and discretized into subsections. In order to calculate the Reynolds number, the cross-section of the pipe must be defined either in terms of diameter (for circular pipes) or by means of its area and wetted perimeter (for non-circular cross-sections). The calculation of the pressure losses requires the definition of a value for the surface roughness (friction losses) and of a coefficient for the head losses. The latter includes both the distributed and the concentrated losses, which have been described in the subparagraph 2.2.1 and evaluated by using the Idel'chick [19].

The modeling of the pipe is completed with the definition of the temperatures of the inner walls, which are provided as boundary conditions.

As seen in Paragraph 2.2, the LPT ACC system here described is a bird-cage configuration [10, 17]. Consequently, the passage of the airflow from one pipe to another involves a discrete loss. These losses are generally included as discrete loss coefficients in the definition of the pipes or, when a sudden reduction in the cross-section occurs, modeled as orifices with a certain discharge coefficient.

The boundary conditions needed for the simulations are the total pressure at inlet, the static pressure at outlet and the total temperature. These values can be estimated basing on the air properties during cruise. Assuming that the cruise altitude is at 35000 ft, the static pressure and temperature can be estimated by using the International Standard Atmosphere (ISA) equations for the troposphere [51]:

$$T_{cruise} = T_{SL} - h \cdot L_h = 218.6\ K$$
$$p_{cruise} = p_{SL}\left(\frac{T_{cruise}}{T_{SL}}\right)^{\frac{g}{L_h R}} \cong 23800\ Pa \tag{3.1}$$

where the subscript SL indicates the sea level reference conditions ($T_{SL} = 288\ K$ and $p_{SL} = 101300\ Pa$), $L_h = 0.0065\ K/m$ is the lapse rate and R here is the gas constant for air.

Since the ACC system delivers the cooling air in the undercowl region, the outlet static pressure can be assumed slightly higher than the atmospheric pressure. On the other hand, the intake total pressure is determined by the pressure at the exit of the engine fan. For the fan of a large aircraft engine, the design practice is to utilize a single stage with a Fan Pressure Ratio (FPR) in the range $1.4 < FPR < 1.8$, with the lower limit set to prevent instabilities of the fan, especially in off-design conditions, and the higher limit imposed in order to avoid local supersonic effects [52]. Considering $FPR = 1.7$, the inlet pressure is of the order of 40 kPa, plus the addition of the recovery factor contribution. This factor (see Equation 2.2) is related to the design of the diffuser and it is mainly affected by the ratio between its inlet and exit areas. In terms of numerical modeling, its effect has been included into the inlet pressure boundary, rather than as a geometrical modification:

$$p_{IN,0} = p_{IN,static} + R_F \cdot p_{IN,dynamic} \tag{3.2}$$

where the recovery factor has been assumed to be $R_F = 0.3$, basing on the indications found in the reference [19].

The ACC system that has been utilized for the DoE has been developed on the basis of the literature data and reproducing an arrangement similar to the bird-cage structure shown in Figure 2.8. In particular, the elements composing the pipeline system are sixteen axial headers and ten spider rails per each axial header, besides the main pipeline and the manifold.

The main pipeline starts with the off-take, which diverts part of the secondary airflow, generated by the engine fan, to supply the ACC system. The properties of the secondary air are represented by setting the total pressure, the static pressure and the total temperature at the inlet boundary, as previously discussed. The off-take is modeled as a discrete loss, which depends on the number of louvers and on their pitch angle. Considering an off-take made by five louvers with a small pitch angle of ten degrees, the loss coefficient that can be estimated by using the Idel'chick is $k_{OT} = 0.2$ [19]. Once the air is taken, the flow is deflected from the vertical direction towards the axial one, by using a 90-degree bend. Then, the air dynamic pressure is partially converted into static pressure by means of a diffuser, where the pipe cross-section is also changed from a rectangular to a circular shape. In the numerical model, these parts are represented by two tube elements with non-constant cross-sections. The effect of both the ninety-degree turn and the rectangular-to-circular transition are modeled as discrete losses, by assigning proper head loss coefficients (always calculated by using reference [19]). All this portion of the ACC system is shown in Figure 3.1.

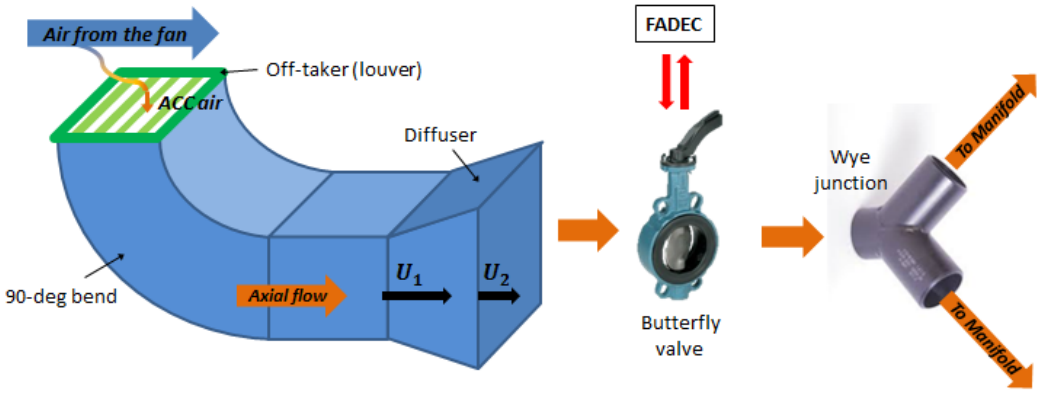

Figure 3.1 - ACC main pipeline (images from [53, 54]).

Downstream the diffuser, there is the valve that regulates the air mass flow rate, which is required to control the LPT clearance. The control valve of the ACC system is driven by the FADEC and it is of the *butterfly* type. The control scheme of the LPT ACC valve is shown in Figure 3.2, top. By using the information about the main engine parameters, the Engine Control Unit (ECU) of the FADEC controls the Hydro Mechanical Unit (HMU), which sends a pressure signal to a linear actuator (see Figure 3.2, bottom, in the red circle). The linear actuator moves a rack that regulates the butterfly valve position, based on the engine operating configuration. Two Rotary Variable Differential Transformers (RVDT) send a feedback signal on the valve position to the ECU [55].

The curves plotted in Figure 3.3, known as valve characteristics, represent the relationship between the valve position and the flow rate. A generic control valve regulates the air flow rate by changing the open area, through which the gas passes. For example, in a linear flow characteristic, the flow rate changes of the same amount of the valve position. This means that the increase in the open area remains constant during the entire stroke of the valve. However, the flow characteristic that best describes the ACC valve is the *equal-percentage* curve. This type of flow characteristic is nonlinear and its slope increases when the valve

is more opened. In other words, the open area exhibits a greater increase in the ending part of the stroke.

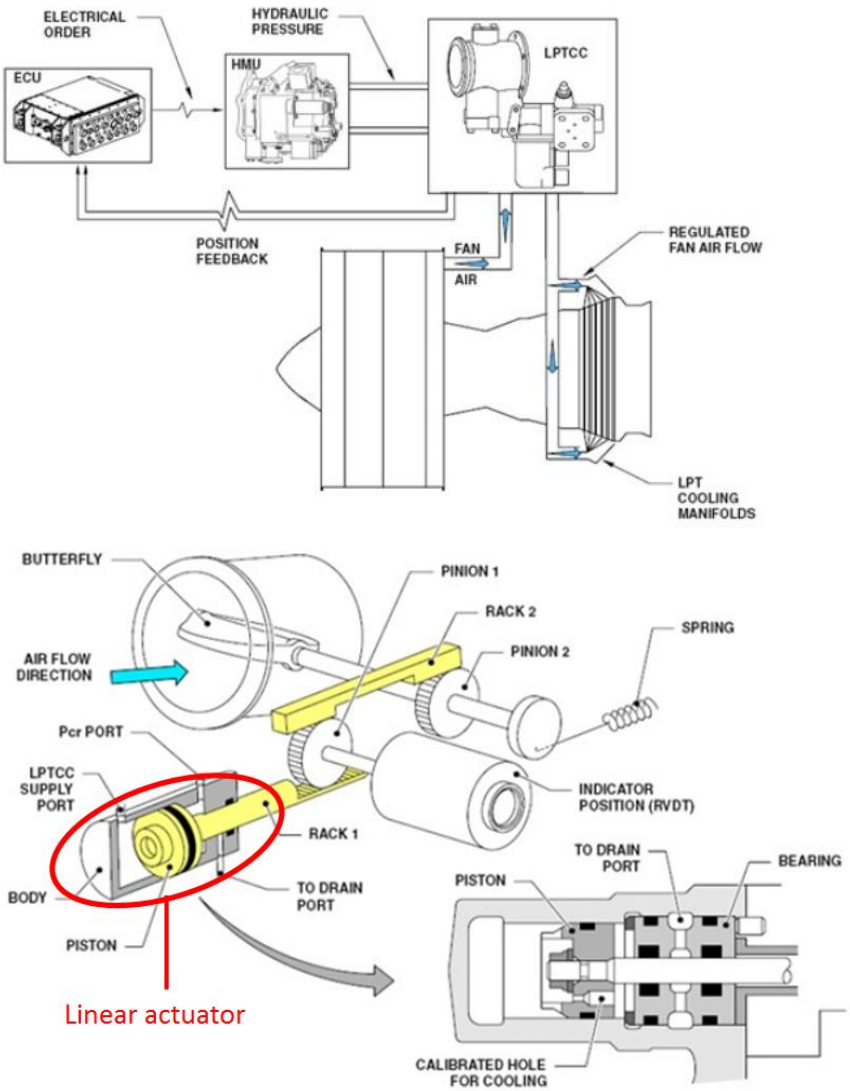

Figure 3.2 - LPT ACC valve: control scheme (top), design (bottom) [55].

The butterfly valve is numerically modeled as an orifice with a fixed discharge coefficient $C_{D,V}$, representing the performance of the valve at full stroke. Since $C_{D,V}$ is fixed, its value in itself is not very important for the purpose of the present analysis. On the contrary, the effect of its variation on the system performance has been evaluated in the DoE.

Once the amount of cooling air has been properly regulated by the FADEC, it flows through the next section of the main pipeline and, then, is split into the two branches of the manifold by means of a wye junction. Despite its design is efficient, this device introduce a discrete head loss, which is included in the tube element that represents the last part of the main pipeline.

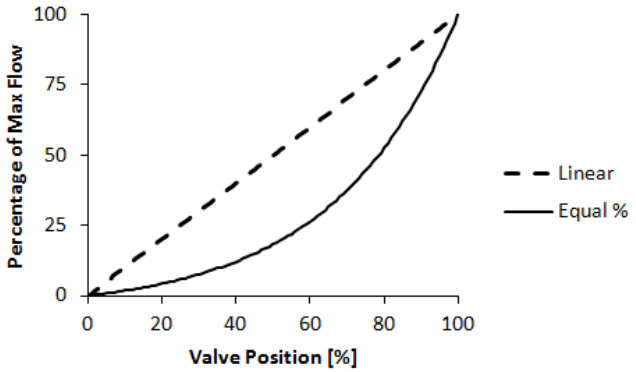

Figure 3.3 - Equal percentage and linear flow characteristics [56].

As previously shown in Figure 2.8, the cooling air is fed to the impinging nozzles by the birdcage arrangement. The supply line starts from the two branches of the manifold and, through the sixteen axial headers, ends with the spider rails (ten per each header) that envelop the whole circumference of the LPT casing.

The split of the air mass flow at the inlet of an axial header can be represented by the more generic condition of a main flow partially deflected into a minor lateral branch, characterized by a discrete head loss (estimated by using the reference [19]).

The passage from an axial header to one of its spider rails is modeled with an orifice, since the air enters the spider rail by means of a slot with a certain shape. Note that the axial header feeds the spider rails in their middle section, so the cooling air splits into two branches for each spider rail. Finally, the impinging jets (around ten thousand in total) are discharged into the undercowl chamber. The nozzles are modeled by orifice elements with a discharge coefficient that can be estimated by using the literature correlations [35, 36 and 37].

3.2 DoE Factors

The previously-described numerical model has been utilized to perform a DoE, in order to identify those parameters of the system, which mainly affect the available mass flow rate in the ACC system. The DoE is full factorial, with six factors and two levels for each factor, consisting in a total of sixty-four runs. For the entire set of simulations, the static pressure in the undercowl chamber is the same and the geometries of the spider rails and impinging nozzles have not been changed. The analyzed factors are listed in Table 3.1, showing their nominal value and the two levels utilized to run the DoE, defined as nominal values or fractions of the nominal value.

To begin with, the off-take loss coefficient and the valve discharge coefficient have been included as factors of the DoE, in order to test how the mass flow rate of the system is affected by their variations. Note that the effect related to the loss coefficient of the off-take has been evaluated by using its inverse $1/k_{OT}$. Concerning the valve, an important observation has to be pointed out, considering that its characteristic is non-linear, as shown in Figure 3.3, while this parameter is represented in the DoE with only two levels. The utilization of two levels for all

the analyzed parameters turned out as a compromise between a contained simulation time and an acceptable representation of their effects, within a certain range. On one hand, the introduction of a third level for the discharge coefficient of the valve would have the advantage to point out the non-linearity of the valve characteristic, leading to a more accurate evaluation of its impact on the mass flow rate of the system. On the other hand, this choice would have increased by 50 percent the whole simulation time. Considering that the objective of the present analysis is to compare the effects of the several parameters and to assess the robustness of the ACC system, two levels have been utilized for all the parameters. More importantly, since the range of the valve stroke, which has been analyzed in the DoE, is relatively small (between 80 and 100 percent of the valve stroke), the linear approach could be considered an acceptable approximation.

The recovery factor (defined in Equation 2.2) represents the increase in static pressure obtained through a diffuser, at the expense of the air dynamic pressure. The current ACC diffuser is designed to obtain a recovery factor $R_F = 0.3$. This means that the 30% of the dynamic pressure is currently recovered, thus converted into static pressure. The two levels analyzed in the DoE represent, respectively, the case of an ACC without diffuser, $R_F = 0$, and a recovery factor that could be reasonably achieved with the optimization of this component in the near future. As discussed in the part concerning the 1D model, the effect of R_F is included in the inlet boundary as an additional contribution to the total pressure.

Table 3.1 - Factors and levels of the full factorial DoE

Factor	Nominal value (NOM)	Low level	High level
Off-take, loss coefficient	$1/k_{OT} = 5$	0.9 · NOM	1.05 · NOM
Valve, discharge coefficient	NOM	0.8 · NOM	NOM
Recovery factor	0.3	0	0.5
Pipe internal roughness	NOM	0.83*NOM	3.3*NOM
Main pipe diameter	0.15 m	0.83 · NOM	NOM
Axial header tapering	1 (No tapering)	0.5 · NOM	NOM

The pipes of the ACC system exhibit a low roughness, of the order of the micrometer. In the present work, a small range of roughness has been investigated and it is expected that this range is too small to generate significant differences in the flow field. However, these parameters have been included in the DoE in order to evaluate their effects in terms of heat transfer. This aspect will be discussed in the next chapter, in which the 1D coupled model will be introduced. In the numerical model, the contribution of the pipe roughness to pressure losses is taken into account in each tube element, where the friction factor is calculated by using the Colebrook-White equation [57].

Obviously, the diameters of the main pipe and of the manifold branches will significantly affect the available mass flow rate. However, larger pipes also increase the overall weight of the ACC system, a drawback that could negatively compensate the advantage gained. On the contrary, smaller pipes are lighter but need higher velocities to ensure the same mass flow rate. In the present work, the diameter of the main pipe in the DoE is represented by a smaller pipe as low level

(83% diameter of the current value) and by the current diameter as high level. This diameter reduction is applied in the same proportion to the manifold branches. In this way, it is possible to investigate the robustness of the ACC system in terms of available mass flow rate under a reduction of its main diameter.

The last parameter included in the DoE is the tapering ratio for the axial header, i.e. the ratio between the ending area and the inlet area of the axial header:

$$\lambda_{AH} = \frac{A_{AH,end}}{A_{AH,in}} \tag{3.3}$$

When $\lambda_{AH} = 1$, the axial headers are not tapered, while the low level has been set to 0.5. This value has been chosen considering that the cross section of the axial header in its ending part should not be too small, when compared to the inlet slot for the last spider rails. In particular, the ratio between these two areas should be higher than three, in order to properly supply the air for the impinging jets and to maintain the plenum condition.

3.3 DoE Results

The obtained results are shown in Tables 3.2 and 3.3, where the number of the run is indicated, together with the level of each factor. The comparison has been made considering the mass flow ratio *MFR*, i.e. the ratio between the mass flow rates obtained for each run and the value of the current design:

$$MFR = \frac{\dot{m}_{Run}}{\dot{m}_{NOM}} \tag{3.4}$$

By observing the two figures, several trends clearly emerge. For example, the recovery factor appears to be important in determining the performance of the ACC system, because it affects its overall pressure ratio. However, besides some basic guidelines such as this, the impact of each factor analyzed need to be more accurately defined. A method that could be useful to fulfill this purpose is to quantify the importance of each factor, by comparing the variations recorded in terms of mass flow rate to the ranges of variation implemented for each parameter. In the present work, this importance has been measured by defining a *derivative* for each factor of the DoE. These derivates have been calculated through the following steps:

- First of all, the percentage variations considered for each factor have been calculated:

$$\Delta\%_{i,j} = \frac{F_{i,j} - F_{i,NOM}}{F_{i,NOM}} \cdot 100 \tag{3.5}$$

where $F_{i,j}$ is the level for a given factor, i is the factor index (from 1 to 6) and j is the level index (1 for the low level, 2 for the high level), while the subscript *NOM* indicates the current design, chosen as the reference value.

Table 3.2 - DoE results: mass flow rate compared to the nominal case, $R_F = 0$ (runs from #1 to #32).

#RUN	R_F	$1/k_{OT}$	$\varepsilon_{R,P}$	d_{MP}	λ_{AH}	$C_{D,V}$	$\dot{m}_{Run}/\dot{m}_{NOM}$
NOM	0.3	0.2	NOM	15 cm	1	NOM	1.000
1	L	L	L	L	L	L	0.850
2	L	L	L	L	L	H	0.869
3	L	L	L	L	H	L	0.854
4	L	L	L	L	H	H	0.874
5	L	L	L	H	L	L	0.898
6	L	L	L	H	L	H	0.920
7	L	L	L	H	H	L	0.902
8	L	L	L	H	H	H	0.924
9	L	L	H	L	L	L	0.850
10	L	L	H	L	L	H	0.869
11	L	L	H	L	H	L	0.854
12	L	L	H	L	H	H	0.873
13	L	L	H	H	L	L	0.898
14	L	L	H	H	L	H	0.920
15	L	L	H	H	H	L	0.903
16	L	L	H	H	H	H	0.924
17	L	H	L	L	L	L	0.864
18	L	H	L	L	L	H	0.884
19	L	H	L	L	H	L	0.868
20	L	H	L	L	H	H	0.886
21	L	H	L	H	L	L	0.914
22	L	H	L	H	L	H	0.937
23	L	H	L	H	H	L	0.919
24	L	H	L	H	H	H	0.942
25	L	H	H	L	L	L	0.863
26	L	H	H	L	L	H	0.883
27	L	H	H	L	H	L	0.868
28	L	H	H	L	H	H	0.887
29	L	H	H	H	L	L	0.912
30	L	H	H	H	L	H	0.936
31	L	H	H	H	H	L	0.918
32	L	H	H	H	H	H	0.941

L Low level
H High level
< 0.90
< 0.95
< 1.00
> 1.00

- The next step is to calculate the average values of the mass flow rate, for each level of each factor. For example, the average mass flow rate for the factor 1 at the level 1 (low level) would be:

$$\dot{m}_{1,1} = mean\left(\dot{m}\left(F_{1,1}, F_{2,j}, F_{3,j}, F_{4,j}, F_{5,j}, F_{6,j}\right)\right) \tag{3.6}$$

  In other words, this value is the average among all the mass flow rates for those 32 simulations, where the factor 1 is set at its low level.
- Once all the values $\dot{m}_{i,j}$ have been calculated, the derivative α_i for each factor is given by Equation 3.7:

$$\alpha_i = \frac{\frac{\dot{m}_{i,2} - \dot{m}_{i,1}}{\dot{m}_{mean}}}{\frac{F_{i,2} - F_{i,1}}{F_{i,NOM}}} \tag{3.7}$$

where $\dot{m}_{mean}$ is the mean mass flow rate obtained as the average among all the results of the DoE. Both $\dot{m}_{mean}$ and $F_{i,NOM}$ ensure non-dimensionality, thus, it is possible to directly compare the effect of all the analyzed factors.

Table 3.3 - DoE results: mass flow rate compared to the nominal case, $R_F = 0.5$ (runs from #33 to #64).

#RUN	R_F	$1/k_{OT}$	$\varepsilon_{R,P}$	d_{MP}	λ_{AH}	$C_{D,V}$	$\dot{m}_{Run}/\dot{m}_{NOM}$
NOM	0.3	0.2	NOM	15 cm	1	NOM	1.000
33	H	L	L	L	L	L	0.950
34	H	L	L	L	L	H	0.970
35	H	L	L	L	H	L	0.954
36	H	L	L	L	H	H	0.975
37	H	L	L	H	L	L	1.000
38	H	L	L	H	L	H	1.023
39	H	L	L	H	H	L	1.005
40	H	L	L	H	H	H	1.028
41	H	L	H	L	L	L	0.950
42	H	L	H	L	L	H	0.970
43	H	L	H	L	H	L	0.955
44	H	L	H	L	H	H	0.974
45	H	L	H	H	L	L	1.000
46	H	L	H	H	L	H	1.023
47	H	L	H	H	H	L	1.005
48	H	L	H	H	H	H	1.028
49	H	H	L	L	L	L	0.965
50	H	H	L	L	L	H	0.986
51	H	H	L	L	H	L	0.970
52	H	H	L	L	H	H	0.991
53	H	H	L	H	L	L	1.016
54	H	H	L	H	L	H	1.040
55	H	H	L	H	H	L	1.022
56	H	H	L	H	H	H	1.045
57	H	H	H	L	L	L	0.963
58	H	H	H	L	L	H	0.985
59	H	H	H	L	H	L	0.969
60	H	H	H	L	H	H	0.990
61	H	H	H	H	L	L	1.016
62	H	H	H	H	L	H	1.040
63	H	H	H	H	H	L	1.022
64	H	H	H	H	H	H	1.046

L Low level
H High level
< 0.90
< 0.95
< 1.00
> 1.00

Table 3.4 - Non-dimensional derivates in the analyzed ranges.

Factor	α_i	$\Delta\%_{i,1}$	$\Delta\%_{i,2}$
R_F	+0.0650	-100%	+66.7%
$1/k_{OT}$	+0.1094	-10%	+5%
$\varepsilon_{R,P}$	-0.0002	-16.7%	+178%
d_{MP}	+0.3273	-16.7%	0%
λ_{AH}	+0.0100	-50%	0%
$C_{D,V}$	+0.1069	-15%	+5.9%

The values of the non-dimensional derivatives, calculated for each analyzed factor, have been listed in Table 3.4, together with the non-dimensional ranges of the analyzed factors, which are $\Delta\%_{i,1}$ and $\Delta\%_{i,2}$ for the low and the high levels, respectively. The Figure 3.4 shows the $MFR_{i,j}$ vs $\Delta\%_{i,j}$ plots, where the former represents in detail the impact of each parameter, while the latter compares all the factors together. The slope of each line provides a quite accurate idea of the non-dimensional derivatives.

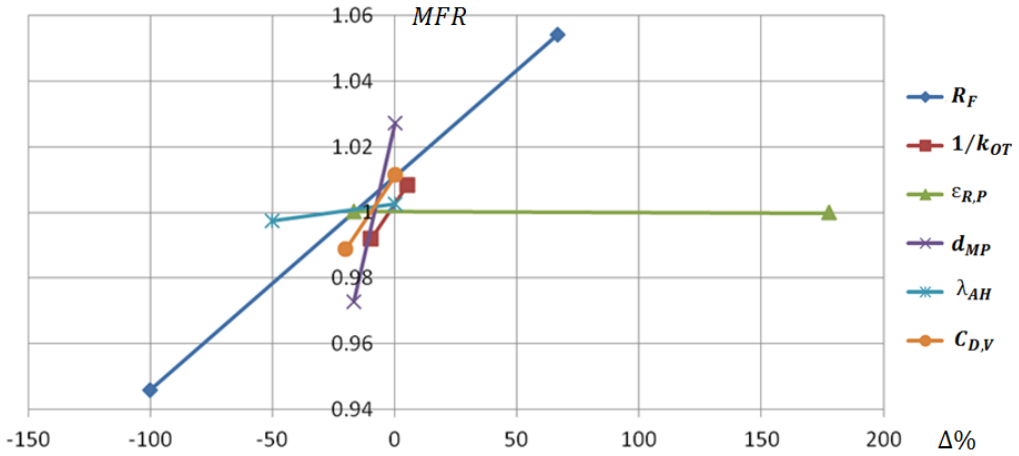

Figure 3.4 - MFR vs non-dimensional ranges.

The results that emerge from the analysis performed with the non-dimensional derivatives are clearer than those shown in the Tables 3.2 and 3.3, where the recovery factor appeared to be the most significant parameter in the ACC design. Actually, several interesting points can be noticed:

- Except for the roughness, all the calculated derivatives are positive, meaning that a positive increase of the considered factor returns a positive increase in terms of mass flow rate.
- The inverse of the off-take loss coefficient and the valve discharge coefficient have a relevant influence on the mass flow, as their derivatives show.
- The recovery factor is also relevant, but not what appears to be at a first glance. Its derivative is small, if compared to the effect given by the variations of the pipe diameter and discharge coefficients.
- As expected, the roughness has a negligible impact on the ACC fluid-dynamics. Indeed, the analyzed range includes values of roughness that are too small when compared to the large diameters of the main pipe or manifold. However, it was not obvious that this consideration would also apply when the relative roughness is calculated referring to the diameter of the spider rails. In this case, the ratio $\varepsilon_{R,P}/d_{SR}$ remains below $2.5 \cdot 10^{-4}$, where d_{SR} is the hydraulic diameter of the spider rail. According to the results recorded by means of the DoE, the Reynolds numbers based on d_{SR} are in the low turbulent regime, in the order of 10^3. With these data, it is possible to notice, on the Moody diagram in Figure 3.5 [58, 59], that the ACC pipes exhibit a very low friction factor. Although roughness is not significant in the analysis of the mass flow rate, it may affect significantly the heat pick-up, discussed in the next chapter.

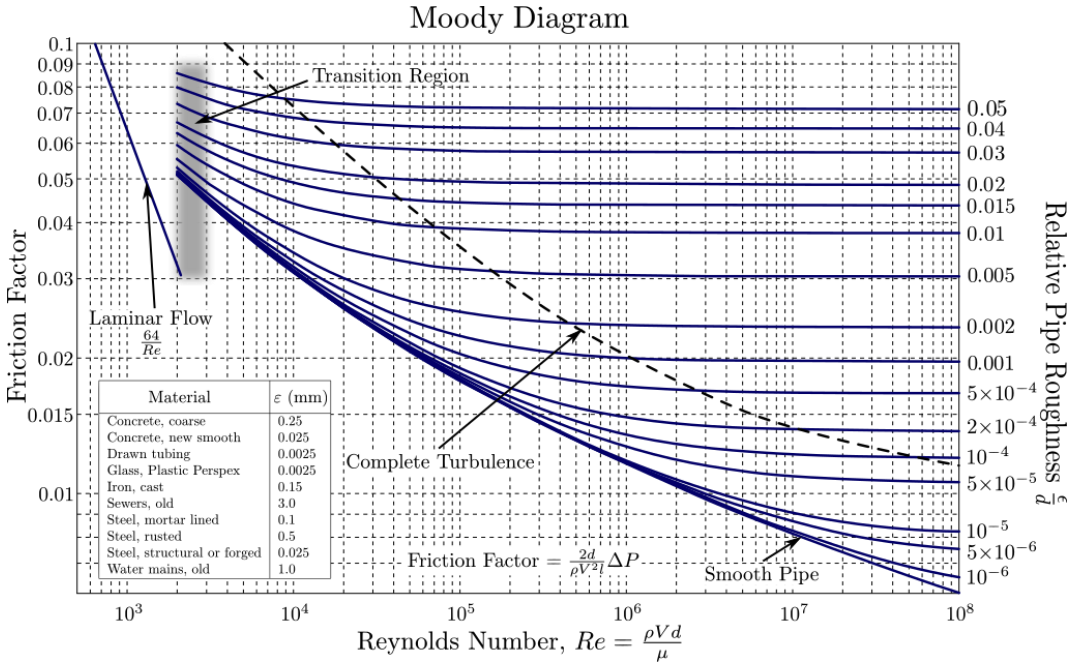

Figure 3.5 - Moody diagram [58, 59].

- The usage of tapered axial headers does not affect the mass flow rate. This result is really interesting, because it means that smaller axial headers (thus lighter) may be employed without affecting performance in a negative way.
- The diameters of the main pipe and the manifold diameter have the strongest impact on the mass flow rate. Unfortunately, this means that, in order to achieve a weight reduction by utilizing smaller pipelines, all other design parameters must be strongly improved to maintain similar mass flow rates.
- Finally, a consideration about costs and benefits has to be made from the manufacturers' point of view. It is easy to change the main pipe diameter, the pipe roughness and to produce tapered axial headers. On the contrary, it is quite more complex to design more efficient valves or off-takes.

Besides the indications given by the analyses on the derivatives, the obtained results can be also compared in terms of design robustness. In other words, the recorded data have been utilized to test the performance of the system under a reduction of the diameter of the main pipe. Although this reduction allows a significant weight decrease, it is expected to reduce the available mass flow rate. Consequently, the system is robust if the mass flow rate reduction can be balanced by increasing the positive effects related to the other design parameters. In Table 3.5, all the results with the high level of recovery factor are listed (runs from #33 to #64). Since the most significant parameter related to weight reduction is the diameter of the main pipe d_{MP}, each row couples two runs, where only d_{MP} changes, while all the other factors (i.e. R_F, $1/k_{OT}$, $\varepsilon_{R,P}$, λ_{AH} and $C_{D,V}$) have the same level. Considering those cases with reduced d_{MP} and $MFR > 0.98$ with a performance similar to the nominal case, the runs #50, #52, #58 and #60 are interesting results. As previously discussed, the roughness and the tapering of the axial headers are not significant in determining the MFR, while the reduction of

the mass flow rate relative to the usage of smaller d_{MP} has to be compensated by improving both the diffuser and the off-take (note that the high level for $C_{D,V}$ is the nominal value). In particular, the obtained results state that, in order to obtain a 17% reduction in d_{MP}, an improvement of 67% in terms of recovery factor is required, in combination with a 5% reduction in the loss coefficient of the off-take (considering the low and high levels reported in Table 1).

Table 3.5 - DoE results: comparison for weight reduction.

#RUN	L Low level / H High level					> 0.98 / > 1.00	
						$\dot{m}_{Run}/\dot{m}_{NOM}$	
L/H	R_F	$1/k_{OT}$	$\varepsilon_{R,P}$	λ_{AH}	$C_{D,V}$	$d_{MP,1}$	$d_{MP,2}$
33/37	H	L	L	L	L	0.950	1.000
34/38	H	L	L	L	H	0.970	1.023
35/39	H	L	L	H	L	0.954	1.005
36/40	H	L	L	H	H	0.975	1.028
41/45	H	L	H	L	L	0.950	1.000
42/46	H	L	H	L	H	0.970	1.023
43/47	H	L	H	H	L	0.955	1.005
44/48	H	L	H	H	H	0.974	1.028
49/53	H	H	L	L	L	0.965	1.016
50/54	H	H	L	L	H	**0.986**	1.040
51/55	H	H	L	H	L	0.970	1.022
52/56	H	H	L	H	H	**0.991**	1.045
57/61	H	H	H	L	L	0.963	1.016
58/62	H	H	H	L	H	**0.985**	1.040
59/63	H	H	H	H	L	0.969	1.022
60/64	H	H	H	H	H	**0.990**	1.046

The weight reduction that can be achieved by reducing the main pipe diameter can be estimated by comparing the areas of the cross-sections for the two levels of diameter. The area of the pipe cross-section is given by:

$$A_{MP} = \left[\left(\frac{d_{MP}}{2} + t_P\right)^2 - \left(\frac{d_{MP}}{2}\right)^2\right]\pi \tag{3.8}$$

where t_P is the thickness of the pipes of the ACC system. Considering a small thickness (from 0.5 to 2 mm), the weight reduction obtainable on the main diameter and on the manifold is about 16% per length units.

Chapter 4

Heat Pick-up

The analyses discussed in the previous chapter had the purpose to improve the efficiency of the ACC system in terms of mass flow rate and they were mainly aimed to study the system from a fluid-dynamic point of view. The next step of the research activity was to include into these analyses the thermal effects related to the surroundings of the ACC system. In other words, the 1D flow network model has been coupled to a 1D thermal tool in order to include the heat pick-up.

This tool, initially developed in Excel VBA, allows evaluating the heat pick-up for a generic pipe section, with or without branches. In the present work, the tool has been arranged to calculate the heat pick-up for the whole ACC pipeline, properly divided into sections. Moreover, an interface has been developed, which is capable to convert the results provided by the flow network solver into inputs for the thermal tool, and vice versa. Then, this approach has been applied to the sixty-four runs of the DoE that has been carried out in the previous chapter. In this way, more accurate results were available. In particular, it was possible to detect the non-uniformity in terms of supplied air, when the several axial headers of the ACC system have been compared. This non-uniformity led to a different clearance control along the circumference of the LPT casing.

4.1 Heat Pick-up Model

The 1D thermal tool has been developed in Excel and VBA and is capable to evaluate the thermal effects exerted on a generic pipeline by its surrounding with an analytical approach. These effects change the temperatures of both the walls of the pipe and the fluid that is flowing inside the pipe. The advantage of using this tool is its low computational cost, compared to a complete 3D model. In other words, it provides a fast 1D approach to the preliminary design of a pipeline and one of its possible applications is the analysis of the heat pick-up taking place in the ACC pipes.

In order to perform the calculations, the tool requires, as input data, the geometry and the material of the pipe, as well as the external boundary conditions in terms of temperature.

The upper scheme in Figure 4.1 shows how the tool models a generic pipe. In the axial direction, it is possible to discretize the pipe by using up to fifteen sections, and each of them can be defined with a different geometry and external boundaries. Moreover, a certain number of branches can be associated to each section. These branches represent the split of the ACC air into the several ducts, e.g. when the air from the manifold is distributed among the axial headers. However, when the modeled pipes are the spider rails, the branches represent the impinging nozzles. Here, the mass flow rate that is discharged for each nozzle is calculated with an iterative procedure, using the indications provided by Da Soghe et al [18]. Considering the pipe cross-section, the numerical model does not reproduce the circular shape, but it represents the pipe as it was composed by two plates, one for the upper half and the other for the lower half of the real pipe, which is closer to the engine casing.

About the output data provided by the tool, the temperatures of the two plates and the thermal power that they transfer are calculated at each section. Then, the temperature of the cooling air at the exit of the section is obtained, evaluating how much the heat pick-up affects this value.

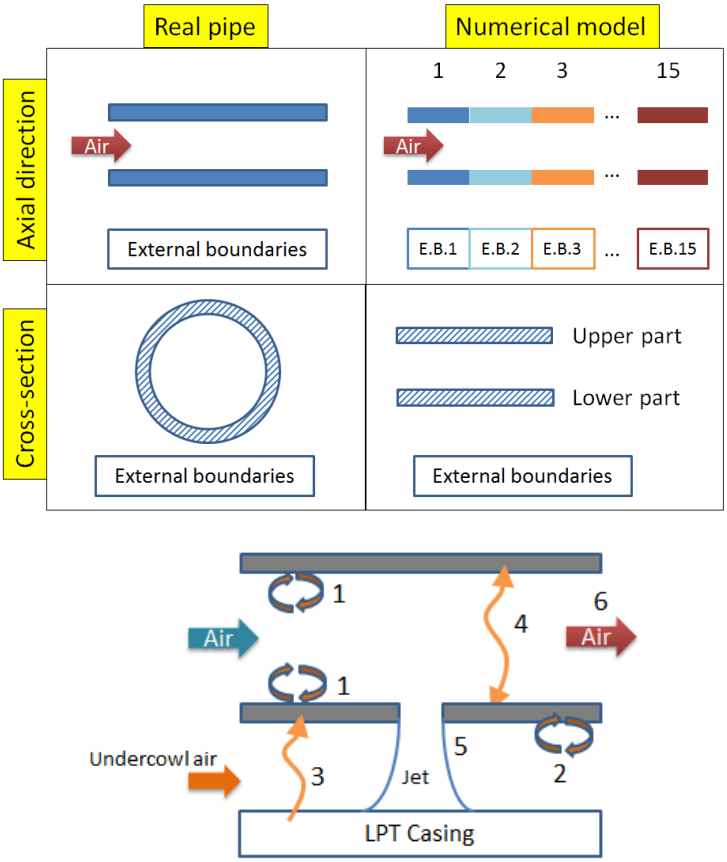

Figure 4.1 - Real pipe vs 1D model discretization (top), heat transfer contributions calculated by the 1D model (bottom).

The bottom of Figure 4.1 illustrates the several heat transfer mechanisms (each of them indicated by a number) involved in the calculations that are carried out by the tool. To begin with, the tool computes the convective heat transfer between the inner walls of the pipe and the cooling air (1) and between the outer walls of the pipe and the undercowl air (2). The temperature of the undercowl air is a boundary condition, and depends on the considered flight phase (the present study is focused on the cruise conditions) and on the surroundings, i.e. this temperature may change depending on the component of the engine that is next to the section of the pipe in question. Heat transfer by radiation occurs between the engine casing and the outer walls of the pipes (3) and between the two plates that model the two halves of the pipe (4). The temperatures of the several sections of the engine casing are boundary conditions that, once again, are determined by the flight phase and by the specific component of the engine considered. A further contribution is included in the calculations, when the spider rails and the impinging nozzles are analyzed. It is the convective heat transfer between the jet downwash and the outer wall of the spider rails (5). While the well-known heat transfer relations utilized to calculate the several contributions have already been shown in subparagraph 2.2.2, the physics behind the calculations that are carried out by the code will be shown here in detail. The heat transfer on each plate occurs on both its outer and inner surfaces and through its thickness: the thermal equilibrium is reached when these three contributions are equal in terms of power.

For the upper plate, the three equations are the following:

$$Q_{u,ex} = HTC_{ex}\frac{S_{ex}}{2}\left(T_{UC} - T_{u,ex}\right)$$

$$Q_{u,w} = \frac{k_m}{t_p}\left(T_{u,ex} - T_{u,in}\right)\frac{S_{ex} + S_{in}}{4} \tag{4.1}$$

$$Q_{u,in} = HTC_{in}\frac{S_{in}}{2}\left(T_{u,in} - T_{air,IN}\right) - \frac{S_{in}}{2}\sigma\frac{1}{2/\varepsilon_P - 1}\left({T_{d,in}}^4 - {T_{u,in}}^4\right)$$

and, similarly, for the lower plate:

$$Q_{d,ex} = HTC_{ex}\frac{S_{ex}}{2}\left(T_{UC} - T_{d,ex}\right) + CC\frac{S_{ex}}{2}\sigma\frac{1}{1/\varepsilon_P + 1/\varepsilon_c - 1}\left({T_{EC}}^4 - {T_{d,ex}}^4\right)$$

$$Q_{d,w} = \frac{k_m}{t_p}\left(T_{d,ex} - T_{d,in}\right)\frac{S_{ex} + S_{in}}{4} \tag{4.2}$$

$$Q_{d,in} = HTC_{in}\frac{S_{in}}{2}\left(T_{d,in} - T_{air,IN}\right) - \frac{S_{in}}{2}\sigma\frac{1}{2/\varepsilon_P - 1}\left({T_{d,in}}^4 - {T_{u,in}}^4\right)$$

In each set of equations, the first one represents the heat transfer on the external surface of the pipe, due to convection on the upper plate and to both convection and radiation (between the ACC pipes and the engine case) on the lower plate. The second equation is the thermal power transferred by conduction within the plate, which has the same thickness of the ACC pipes. The last relation

expresses the convective and the radiative heat transfers occurring in the inner part of the pipes.

The subscripts *u, d, ex, in* stand for up or down (referring to the two plates) and outer or inner (referring to the pipe walls). The surfaces that are subject to the heat transfer are indicated with *S*. Note that they are divided by two because the surfaces of each pipe are equally split between the two plates that represent it. The values k_m, t_m, σ, ε_p and ε_c are the thermal conductivity of the metal (depending on the temperature and calculated according [23]), the thickness of the ACC pipes, the Boltzmann constant and the emissivity of the pipe and the engine case (assumed according [22]). The coefficient *CC* is a corrective factor for the radiation between the ACC pipes and the engine case, which includes the effect of the view factor. The heat transfer coefficients have been calculated by using the literature correlations described in the paragraph 2.2. The temperatures T_{UC} and $T_{air,IN}$ refers to the air of the undercowl and to the cooling air at the inlet of the analyzed section, respectively. The unknowns of the six equations are the temperatures of the plate surfaces ($T_{u,ex}, T_{d,ex}, T_{u,in}, T_{d,in}$) and the heat transferred on each plate ($Q_d$and Q_u).

The thermal equilibrium for a given section is solved by means of an iterative procedure that calculates the values of the four temperatures on the plate surfaces. This procedure is concluded when the root sum squared error of the temperatures, between the i-th and the (i-1)-th iterations, is smaller than a tolerance value:

$$RSS = \sqrt{\sum_{k=1}^{n=4} \left(T_{k,i} - T_{k,i-1}\right)^2} \leq tol = 10^{-6}K \tag{4.3}$$

where the subscript *k* refers to each of the surface temperatures previously defined.

Since the thermal tool allows analyzing only one part of the pipeline at a time, it was necessary to properly divide the ACC system, in order to guarantee an accurate evaluation of the local heat pick-up.

The first part models the main pipeline, which extends from near the engine fan to the LPT. Due to its extension, the thermal boundaries of this part widely change. Moreover, several geometrical variations in the cross-section of the pipe have to be taken into account, as already discussed in the paragraph concerning the flow network model. For these reasons, this part of the ACC has been discretized into eleven sections, the last one with two branches, which represent the split of the manifold.

The manifold is here represented by two parts, one for each of its branches. The first one has been discretized into nine sections and has a constant cross-section. This subdivision is useful, since it allows calculating the temperatures near the inlets of each of the eight axial headers that are connected to this part. The second branch has been modeled with thirteen parts: this higher number is necessary to take into account two variations in the cross-section of the manifold,

due to the interference of the ACC system with other components of the engine. Since the manifold is a circumferential component, the last sections of the two branches are connected to each other.

Each of the axial headers, which are sixteen in total, has been divided into ten sections, as many as the spider rails they supply with the cooling air. The cross-section can be either constant or tapered, as explained in the paragraph 3.2.

Finally, there are ten spider rails per axial header. Each of them is divided into two branches, adding up to 320 parts. Each branch of a spider rail is divided into two sections, with a constant cross-section. The number of impinging nozzles may change, depending on the considered rail.

4.2 Thermal-Fluid Interface

As previously discussed, the thermal tool requires several input data and analyzes one part of the ACC system at a time. In order to perform the calculations for the whole system (composed by 339 parts in total) by using this approach, a continuous and great effort in terms of data to be inserted by the user would be required. Moreover, the air properties calculated at the exit of a certain part could be the input data for another part that is placed downstream, depending on the birdcage structure of the ACC system. Consequently, the user should insert carefully the correct input data for each part, each time. These two reasons make this kind of approach quite prohibitive for a fast preliminary design.

In order to overcome these issues, an interface has been developed, that automates, almost completely, the input and output data management between the thermal part and the flow network model. The functions performed by this interface tool will be explained in the following paragraphs.

The preliminary step to be performed is to run the flow network solver model of the ACC system, in order to solve its fluid-dynamics. Once the simulation has been carried out, an output file will be produced. This file shows a structure in blocks, each of them containing all the data concerning one of the elements composing the ACC system (their types have been described in paragraph 3.1). Each block is indeed identified by the ID number and the type of the element. The first task of the interface tool consists into converting this output file from the 1D into a format that can be read by the thermal tool.

Among the available outputs, the thermal tool requires the mass flow rates, the air pressures and the temperatures at the inlet of each ACC part. Since all the elements of the flow network model are labeled with an ID number, the interface tool has to search the correct ID number and to associate it to the proper section of the thermal model. In this way, the issue of maintaining the correct sequence of the analyzed parts has been solved and automated. It must also be noticed that the subdivisions in parts and sections of the thermal scheme generally replicate the flow network model. Consequently, the geometry of the pipes can also be taken from the 1D fluid model output file. The only exception is the main pipe, which is represented in the thermal model by a larger number of sections than in the flow network model (thirteen sections against five), due to its length and to the

boundary conditions that widely change. For this part, the geometry is properly recalculated, where necessary. Finally, the thermal model requires also other input data, such as some properties concerning the cooling air (i.e., thermal conductivity, Prandtl number, kinematic viscosity and density) or the material of the pipes (thermal conductivity). Considering their dependence on the local air or metal temperatures, these values are calculated by interpolation from the data available in the literature (for the metal [23], for the air [60]).

Since all the required input data are now available, the interface tool starts the thermal tool, which solves the thermal field for each ACC part. The tool calculates the temperatures of the inner walls of the pipes, considering the effects of the surroundings. For each section, two temperatures are calculated, the first one for the upper half of the pipe and the second value for the lower half (see Figure 4.1, top). The average value between these two temperatures will be inserted as input in the flow network solver. Indeed, this model utilizes the wall temperatures of the pipes as boundary conditions, defined by the user for each tube element. In this way, it will be possible to couple the heat pick-up and the fluid-dynamics of the ACC system.

Now that the temperatures of the inner walls of the pipes are known, it is necessary to generate a new input file for the flow network solver. First of all, these temperatures have to be assigned to the correct element in this model. The interface tool performs this task by using the unique ID element, similarly to what was done when the input data for the thermal tool was collected. Then, it is necessary to convert again all the data into a format that can be utilized as an input file for the flow network solver. Since these files can be usually opened with the *Notepad* application for Windows, in spite of their extensions, it is sufficient that the interface tool creates a set of data that can be saved in a *.txt* file, which will be then renamed by the user with the extension of the input files of the flow network model.

Finally, the interface tool also shows the main results and saves the data of the accomplished simulation.

4.3 Results of Heat Pick-up Analysis

By using the 1D coupled model, the fluid-dynamics and the heat pick-up of the ACC system can be simulated together. This model has been utilized to analyze a DoE, which involved the same parameters and levels seen in chapter 3 and reported in Table 3.1. The objectives of this analysis were two. In the first place, the effect of heat pick-up on the derivatives for the investigated parameters has been analyzed and compared to the results provided by the DoE with only the fluid-dynamics. Secondly, the distribution of the air mass flow rate and of the temperatures for air and metal has been considered, providing a circumferential view of these quantities.

4.3.1 Derivatives for the Factors of the DoE

As explained in paragraph 3.3, the non-dimensional derivates are coefficients that allow comparing the effects of the parameters analyzed in the DoE. In this way, it is possible to highlight which parameter affects the most the performance of the ACC system in terms of mass flow rate.

The first interesting result is the comparison between the two DoE in terms of mean mass flow rate $\dot{m}_{mean}$. The ratio between the two mean mass flow rates is given by:

$$\frac{\dot{m}_{mean,coupled}}{\dot{m}_{mean.fd}} = 1.0094 \tag{4.4}$$

where the subscripts *fd* and *coupled* indicate the DoE performed with only the flow network solver and the one carried out with the coupled model, respectively. As shown in Equation 4.4, a slight increase in the mean mass flow rate has been recorded when the fluid-dynamic/thermal integration has been introduced. This means that, by applying this procedure, the ACC pipes turned out to be, on average, slightly colder than those considered with fixed boundaries, which have been assigned to the tube elements in the flow network model. As a consequence of these lower temperatures, the air density, and thus the mass flow rate, is higher.

Then, a more detailed comparison has been performed, underlining the variations in terms of non-dimensional derivatives. These values are compared in Table 4.1, together with the percentage variations that have been recorded between the two DoE. The percentage variations have been calculated with the Equation 4.5:

$$\Delta\alpha_{\%} = \frac{\alpha_{i,coupled} - \alpha_{i,fd}}{\alpha_{i,fd}} \cdot 100 \tag{4.5}$$

Table 4.1 - Non-dimensional derivates for the two DoE.

Factor	$\boldsymbol{\alpha_{i,fd}}$	$\boldsymbol{\alpha_{i,coupled}}$	$\boldsymbol{\Delta\alpha_{\%}}$
R_F	+0.0650	+0.0662	+1.8
$1/k_{OT}$	+0.1094	+0.1145	+5.1
$\varepsilon_{R,P}$	-0.0002	-0.0003	+71.4
d_{MP}	+0.3273	+0.3132	-4.2
λ_{AH}	+0.0100	+0.0077	-21.8
$C_{D,V}$	+0.1069	+0.1114	+4.3

The presence of the heat pick-up does not substantially modify the impact of the analyzed factors: the conclusions reported in chapter 3, when only the fluid-dynamics have been considered, are still valid for the coupled DoE.

However, it is interesting to analyze how the derivatives have changed, referring to the value $\Delta\alpha_{\%}$, shown in the last column of Table 4.1:

- To begin with, the derivative of the recovery factor has a negligible variation.
- As expected, the derivative of the roughness showed a large increase, due to its higher impact on the heat transfer. Nevertheless, the derivative still exerts a negligible effect on the mass flow rate.
- The variations of the derivatives associated to the discharge coefficient of the valve and the loss coefficient of the off-take are about +5%. This effect is related to the fact that the average temperatures, calculated with the coupled model, are slightly lower than the previously recorded values. Since the mass flow rates now are slightly higher, the increase of these discharge coefficients has a greater impact in terms of their variations.
- Both the derivatives that are related to variations in the cross-sections of the pipes decrease. This is a positive fact, since reducing the diameter of the main pipe and the manifold has a less negative effective on the performance, while the same weight reduction still applies. Similarly, the impact of tapered axial headers is even smaller than the negligible effect recorded in the DoE with only the fluid-dynamics. These reductions can be explained considering that a larger pipe implies a larger surface for the heat transfer. Consequently, a large diameter is more sensitive to heat pick-up.

4.3.2 Distributions of Mass Flow Rate

The next step consists in the analysis of the distribution, in terms of mass flow rate, among the sixteen axial headers of the ACC system. In order to obtain an effective visualization of this distribution, radar charts have been utilized for the post-process of the results. Generally, radar charts allow displaying three or more variables on a two-dimensional plot. Here, their axes start from the same point, i.e. the center of the graph, while their relative position and angle provide no information. In the present work, radar charts have been utilized to represent the variations of a certain parameter on all the axial headers at the same time. In this way, it is possible to know whether the mass flow rate distributes in a uniform way or not.

First of all, it is necessary to define a parameter that will be useful to compare how the mass flow rate splits among the sixteen axial headers. This parameter is the split ratio of the mass flow rate $MFS_{AH\ \#i}$, defined as:

$$MFS_{AH\ \#iX} = \frac{\dot{m}_{AH\ \#iX}}{\dot{m}_{mean,AH}} \tag{4.6}$$

where $\dot{m}_{mean,AH} = \dot{m}_{total}/16$ is the mean mass flow rate per axial header, that is the total mass flow rate of the analyzed ACC configuration, divided by the number of the axial headers. In addition, the subscript *AH#iX* indicates the axial header with the number *#iX*. Here, *i* ranges from 1 to 8 and represents the progressive order from the inlet of the manifold to its end, and *X* can be A or B, indicating one of the two manifold branches. When $MFS_{AH\ \#iX} > 1$, the considered axial header has a mass flow rate that is greater than the mean value.

On the contrary, $MFS_{AH\ \#iX} < 1$ indicates a condition where there is a mass flow rate lower than the mean value.

The radar charts for the mean value of the DoE and for the six parameters investigated are shown in Figures 4.2 and 4.3. The graphs have seventeen axes, one for each axial header plus one for the manifold inlet, labeled *IN*. Each plot shows the behavior of $MFS_{AH\ \#iX}$ for a certain parameter and contains the two curves, which are the results for the low and high levels, in blue and red, respectively. These results have been calculated with the same procedure described in chapter 3 using the Equation 3.6, with the difference that, this time, the calculated values of mass flow rate refer to each axial header and not to the entire ACC system. An ideal condition, in which all the axial headers are fed with the same amount of air, is represented by the black circle with $MFS_{AH\ \#iX} = 1$.

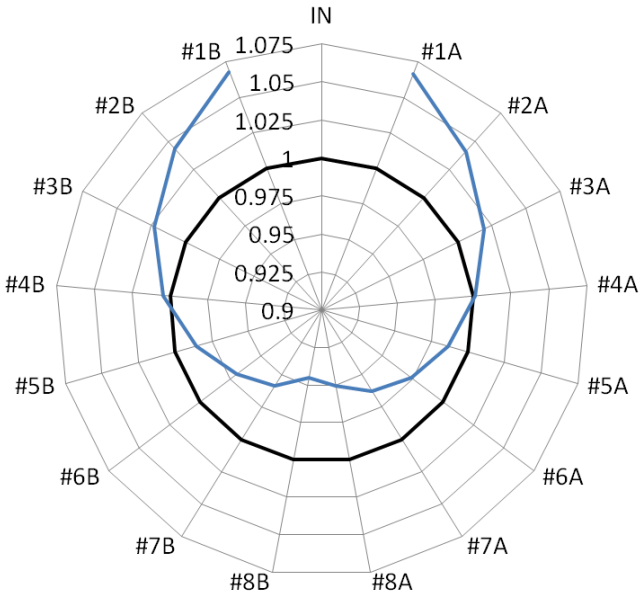

Figure 4.2 - Radar chart with $MFS_{AH\ \#iX}$ for the mean value, calculated for the entire DoE.

The radar chart in Figure 4.2 shows the average distribution for the entire DoE. It clearly appears that the mass flow rate does not split in a uniform way along the two branches of the manifold. In particular, the first three axial headers exhibit $MFS_{AH\ \#iX} > 1$, while the fourth approaches the ideal value (near the unity). The other headers, from the fifth to the eighth, show a gradual decrease in the quantity of supplied air, leading to conditions in which $MFS_{AH\ \#iX} < 0.95$.

Moreover, a slight asymmetry can be noticed between the two manifold branches. It is related to a geometrical modification on the branch B of the manifold, due to the interference with other engine components. This local cross-section reduction influences the pressure losses and, thus, the available mass flow rate is lower than in the branch A.

The graphs in Figure 4.3 provide more detailed information, since the parameters are considered one at a time:

- The most of the analyzed factors do not affect the uniformity in terms of mass flow rate, since the two curves for the low and high levels are practically coincident. This conclusion applies to the discharge coefficients of the valve and the off-take. Since they are placed upstream, they just influence the available mass flow rate, without any effect on the distribution among the axial headers. Neither the roughness is significant, being it applied to all the pipes of the ACC system. Also the tapering ratio of the axial headers has no effect on this distribution.
- A slightly better uniformity can be achieved by increasing the static pressure in the system, i.e. when the recovery factor R_F is higher.
- The diameter of the main pipe and manifold is the most significant factor in determining how the mass flow rate split among the headers. Reducing this value resulted into a worsened distribution. Considering the diameter of the manifold, it has been reduced by 17%. In terms of area, this variation implies a 31% reduction between the high and the low levels of d_{MP}. On the contrary, the cross-section of the axial headers at the inlet has not been changed in the DoE. Consequently, the cross-section of the manifold becomes smaller, when compared to the sum of the area of the headers, resulting in the worse uniformity that has been recorded.

Besides the results provided by the radar charts, another method to measure the uniformity in the distribution of the mass flow rate is to compare the highest and the smallest values of $MFS_{AH\ \#iX}$ (the values of the axial headers #1A and #8B, respectively):

$$\Delta_{AH} = MFS_{AH\ \#1A} - MFS_{AH\ \#8B} \tag{4.7}$$

The formula in Equation 4.7 is a generic definition that could be applied, by specifying the proper subscripts, either to the levels of a parameter or to a single run.

Similarly to the mass flow rates in Equation 3.6, the values of Δ_{AH} are two for each parameter, since they are calculated for both the low and the high levels. Repeating the procedure already seen to define the non-dimensional derivatives for the mass flow rate, it is possible to calculate the derivatives for the uniformity of the split among the axial headers:

$$\alpha_{AH,i} = \frac{\Delta_{AH,i,2} - \Delta_{AH,i,1}}{\frac{F_{i,2} - F_{i,1}}{F_{i,NOM}}} \tag{4.8}$$

where the subscript i is the factor index, while 1 and 2 indicate, respectively, the low and the high levels of the considered factor.

The obtained results are summarized in Table 4.2. By comparing all the parameters with this non-dimensional approach, it is clear that all the parameters, except the diameter of the main pipe, exert a negligible effect on the split of the mass flow ratio among the headers. In particular, the negative derivative means that the uniformity is improved by a positive variation of the considered factor,

i.e. a larger diameter for both the main pipe and manifold enhances the uniformity, as shown with the radar charts.

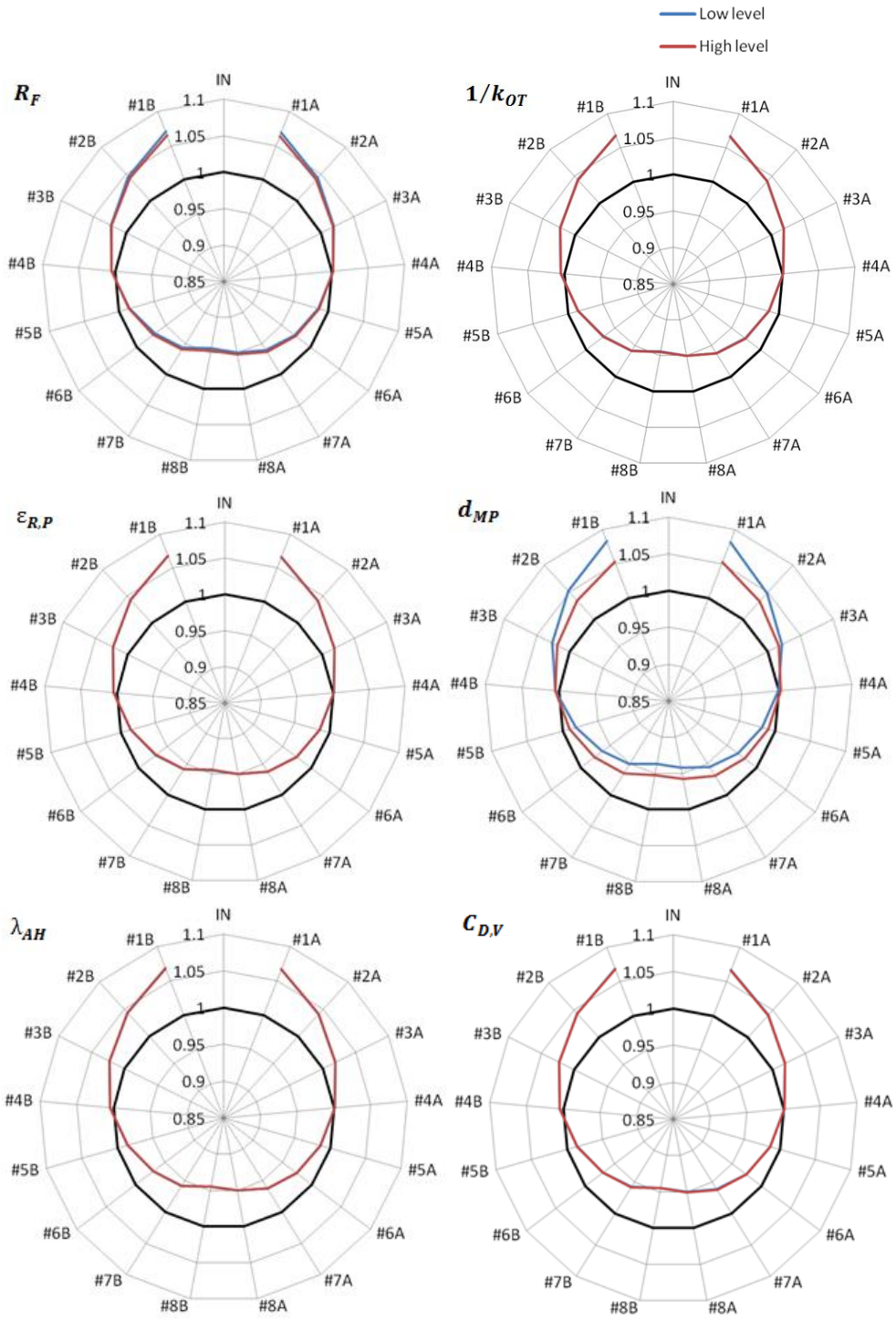

Figure 4.3 - Radar charts with $MFS_{AH\ \#iX}$ for the DoE parameters.

Table 4.2 - Results for uniformity, depending on the DoE parameters.

Factor	$\Delta_{AH,i,1}$	$\Delta_{AH,i,2}$	$\alpha_{AH,i}$
R_F	0.1256	0.1176	-0.0080
$1/k_{OT}$	0.1222	0.1210	-0.0076
$\varepsilon_{R,P}$	0.1214	0.1218	0.0002
d_{MP}	0.1441	0.0991	-0.2700
λ_{AH}	0.1215	0.1217	0.0006
$C_{D,V}$	0.1224	0.1208	-0.0076

Table 4.3 - Coupled DoE results, $R_F = 0$ (runs from #1 to #32).

	Low level
L	
H	

$\dot{m}_{Run}/\dot{m}_{NOM}$	
	< 0.90
	< 0.95
	< 1.00
	> 1.00

Δ_{AH}	
	> 0.150
	< 0.150
	<0.125
	< 0.100

#RUN	R_F	$1/k_{OT}$	$\varepsilon_{R,P}$	d_{MP}	λ_{AH}	$C_{D,V}$	$\dot{m}_{Run}/\dot{m}_{NOM}$	Δ_{AH}
NOM	0.3	0.2	NOM	15 cm	1	NOM	1.000	0.097
1	L	L	L	L	L	L	0.860	0.149
2	L	L	L	L	L	H	0.880	0.147
3	L	L	L	L	H	L	0.863	0.149
4	L	L	L	L	H	H	0.882	0.151
5	L	L	L	H	L	L	0.905	0.103
6	L	L	L	H	L	H	0.928	0.103
7	L	L	L	H	H	L	0.909	0.102
8	L	L	L	H	H	H	0.933	0.101
9	L	L	H	L	L	L	0.858	0.152
10	L	L	H	L	L	H	0.879	0.149
11	L	L	H	L	H	L	0.862	0.150
12	L	L	H	L	H	H	0.881	0.151
13	L	L	H	H	L	L	0.905	0.102
14	L	L	H	H	L	H	0.927	0.105
15	L	L	H	H	H	L	0.909	0.102
16	L	L	H	H	H	H	0.932	0.101
17	L	H	L	L	L	L	0.874	0.147
18	L	H	L	L	L	H	0.895	0.146
19	L	H	L	L	H	L	0.876	0.152
20	L	H	L	L	H	H	0.898	0.149
21	L	H	L	H	L	L	0.921	0.103
22	L	H	L	H	L	H	0.946	0.100
23	L	H	L	H	H	L	0.926	0.101
24	L	H	L	H	H	H	0.951	0.100
25	L	H	H	L	L	L	0.873	0.149
26	L	H	H	L	L	H	0.895	0.146
27	L	H	H	L	H	L	0.875	0.152
28	L	H	H	L	H	H	0.897	0.150
29	L	H	H	H	L	L	0.922	0.101
30	L	H	H	H	L	H	0.945	0.105
31	L	H	H	H	H	L	0.926	0.101
32	L	H	H	H	H	H	0.950	0.100

The obtained results can be also analyzed in terms of single runs, in order to identify the best and the worst conditions of uniformity. The data are shown in Tables 4.3 and 4.4, including the levels that have been set for each run, the mass flow rate ratio MFR (see Equation 3.4) and the parameter for uniformity Δ_{AH}. Note that these results refer to the coupled DoE, thus the values of MFR reported are different from the ones shown in Tables 3.2 and 3.3. However, as shown in Equation 4.4, the variations between the two DoE are very small.

Table 4.4 - Coupled DoE results, $R_F = 0.5$ (runs from #33 to #64).

#RUN	R_F	$1/k_{OT}$	$\varepsilon_{R,P}$	d_{MP}	λ_{AH}	$C_{D,V}$	$\dot{m}_{Run}/\dot{m}_{NOM}$	Δ_{AH}
NOM	0.3	0.2	NOM	15 cm	1	NOM	1.000	0.097
33	H	L	L	L	L	L	0.963	0.140
34	H	L	L	L	L	H	0.984	0.138
35	H	L	L	L	H	L	0.966	0.142
36	H	L	L	L	H	H	0.988	0.139
37	H	L	L	H	L	L	1.010	0.097
38	H	L	L	H	L	H	1.034	0.096
39	H	L	L	H	H	L	1.014	0.097
40	H	L	L	H	H	H	1.038	0.096
41	H	L	H	L	L	L	0.962	0.141
42	H	L	H	L	L	H	0.984	0.139
43	H	L	H	L	H	L	0.965	0.142
44	H	L	H	L	H	H	0.987	0.139
45	H	L	H	H	L	L	1.010	0.098
46	H	L	H	H	L	H	1.034	0.096
47	H	L	H	H	H	L	1.014	0.098
48	H	L	H	H	H	H	1.038	0.096
49	H	H	L	L	L	L	0.978	0.139
50	H	H	L	L	L	H	1.000	0.137
51	H	H	L	L	H	L	0.982	0.139
52	H	H	L	L	H	H	1.003	0.137
53	H	H	L	H	L	L	1.027	0.098
54	H	H	L	H	L	H	1.052	0.095
55	H	H	L	H	H	L	1.032	0.096
56	H	H	L	H	H	H	1.057	0.095
57	H	H	H	L	L	L	0.978	0.139
58	H	H	H	L	L	H	1.000	0.137
59	H	H	H	L	H	L	0.981	0.139
60	H	H	H	L	H	H	1.003	0.137
61	H	H	H	H	L	L	1.027	0.097
62	H	H	H	H	L	H	1.052	0.094
63	H	H	H	H	H	L	1.032	0.096
64	H	H	H	H	H	H	1.056	0.097

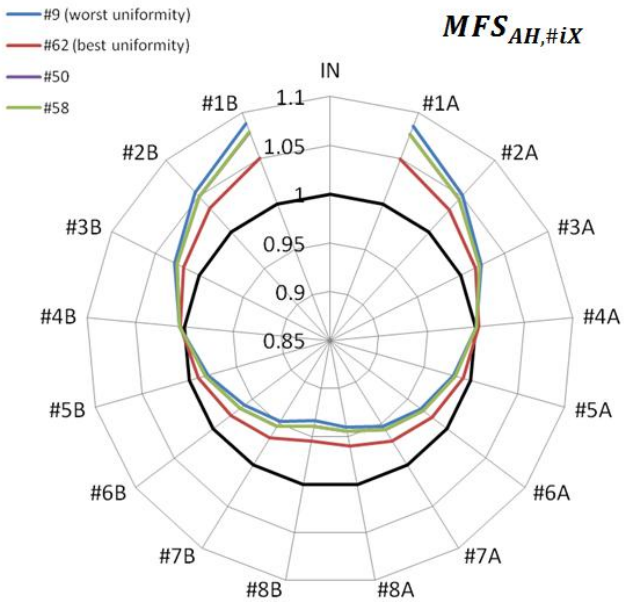

Figure 4.4 - Flow uniformity: radar chart with the most significant runs.

In particular, the two configurations numbered as #50 and #58, circled in Table 4.4, are interesting solutions. They exhibit a reduced weight, since both have the smallest pipe diameter and tapered axial headers. The available mass flow rates are similar to the one recorded under nominal conditions. However, the price to be paid for weight reduction is a penalty in terms of uniformity, since the last axial headers are fed with less air than in nominal conditions. Among all the runs, the number #9 and #62 turned out to be the worst and the best cases, in terms of uniformity. All these cases are shown in the radar chart in Figure 4.4. Note that the curves for runs #50 and #58 are practically coincident.

4.3.3 Distribution of Air Temperature for the Axial Headers

The analyses performed on the air temperature distribution are similar to the ones performed for the mass flow in the previous subparagraph. Here, the air temperatures have been recorded at the inlet and at the end of each axial header and compared on the radar charts (see Figure 4.5). However, none of the analyzed parameters appeared to be effective on the temperature distribution. The two radar charts describe indeed the behavior of the air temperature at the two locations and are practically identical for all the DoE parameters, with low and high levels almost coincident. Overall, it can be noticed the circumferential non-uniformity. This difference is due to the fact that the air, in order to reach the last axial headers, has a longer permanence, thus a higher heat pick-up. For the same reason, the air temperature becomes higher at the end of the axial headers (as shown in the radar chart in Figure 4.5, right).

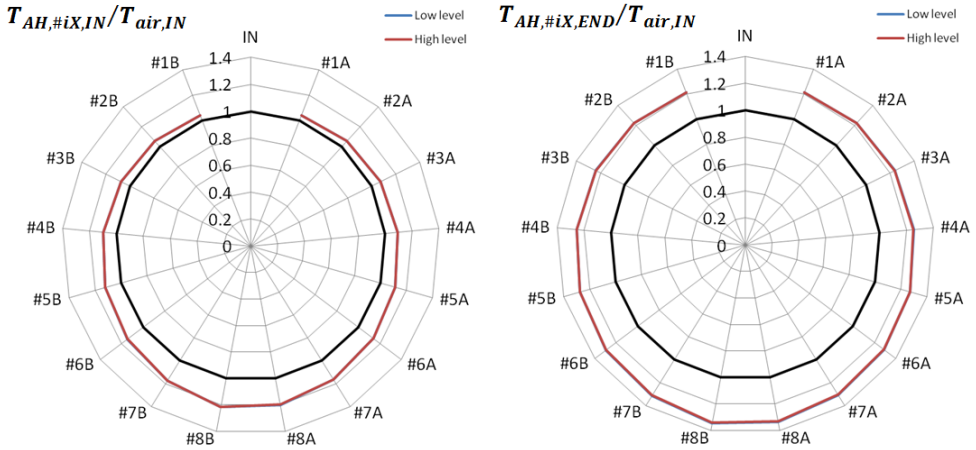

Figure 4.5 - Distribution of air temperature: radar charts at inlet and end of the axial headers.

The calculation of the non-dimensional derivatives led to negligible values for all the considered parameters, as shown in Table 4.5:

$$\alpha_{AH\,T,i} = \frac{\Delta T_{AH,i,2} - \Delta T_{AH,i,1}}{\frac{F_{i,2} - F_{i,1}}{F_{i,NOM}}} \qquad (4.9)$$

$$\Delta T_{AH,i,j} = T_{AH\,\#1A,i,j} - T_{AH\,\#8B,i,j}$$

Table 4.5 - Derivatives for the distribution of the air temperature.

Factor	$\alpha_{AH\,T\,IN,i}$	$\alpha_{AH\,T\,END,i}$
R_F	0.0068	0.0028
$1/k_{OT}$	0.0061	0.0024
$\varepsilon_{R,P}$	0.0000	0.0000
d_{MP}	0.0243	0.0235
λ_{AH}	0.0005	-0.0025
$C_{D,V}$	0.0065	0.0026

4.3.4 Distribution of Temperatures for the Spider Rails

Finally, the heat pick-up for the spider rails has been analyzed. Since none of the parameters investigated within the DoE had a significant effect on the distribution of the temperature in the axial headers, it can be assumed that all the analyzed ACC configurations behave in a very similar way when the temperatures of the spider rails are considered.

The circumferential uniformity in terms of temperatures can be analyzed with a statistical approach, by using normal distributions [61]. For each spider rail, two normal distributions have been plotted, referring to the temperatures of the metal and of the air, respectively. For example, the graph at the top in Figure 4.6 refers to the Rail 1. Here, all the first spider rails for all the sixteen axial headers of all the run of the DoE have been considered. The temperatures, which have been normalized with the air temperature at the inlet, are calculated according to the subdivision described in paragraph 4.1. In other words, each spider rail is composed of two branches and each branch is modeled with two sections, for a total of four values of temperature per part.

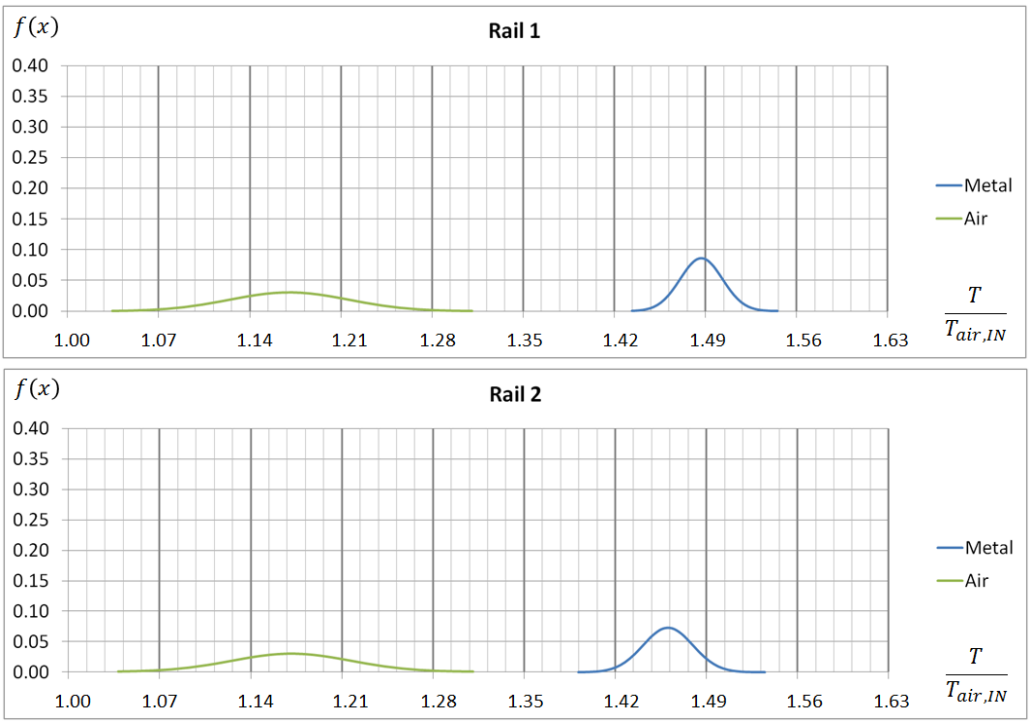

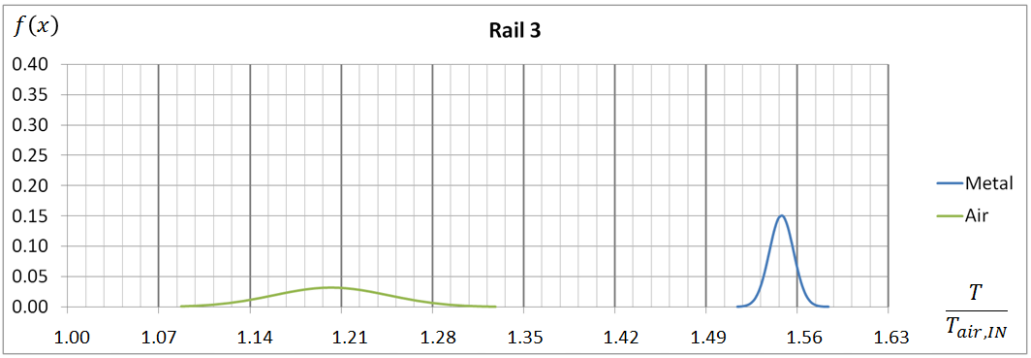
f(x)
Rail 3
0.40
0.35
0.30
0.25
0.20
0.15
0.10
0.05
0.00
1.00
1.07
1.14
1.21
1.28
1.35
1.42
1.49
1.56
1.63
Metal
Air
T / T_air,IN

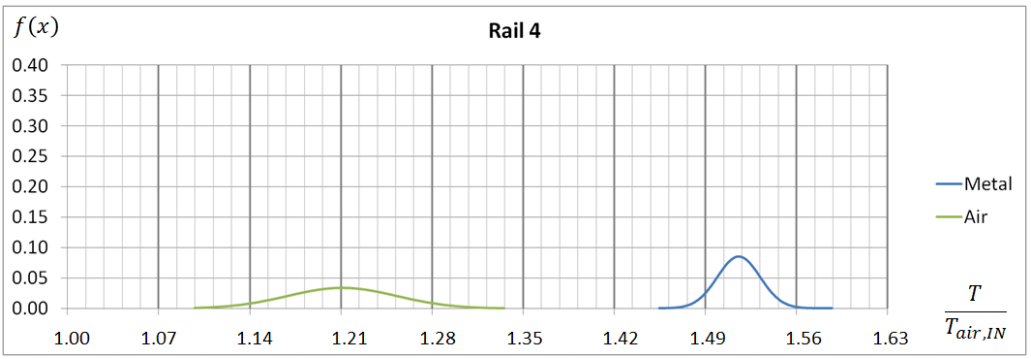
f(x)
Rail 4
0.40
0.35
0.30
0.25
0.20
0.15
0.10
0.05
0.00
1.00
1.07
1.14
1.21
1.28
1.35
1.42
1.49
1.56
1.63
Metal
Air
T / T_air,IN

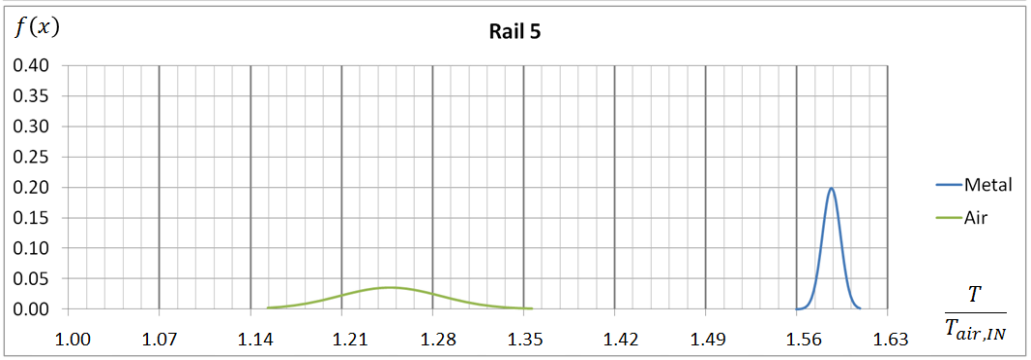
f(x)
Rail 5
0.40
0.35
0.30
0.25
0.20
0.15
0.10
0.05
0.00
1.00
1.07
1.14
1.21
1.28
1.35
1.42
1.49
1.56
1.63
Metal
Air
T / T_air,IN

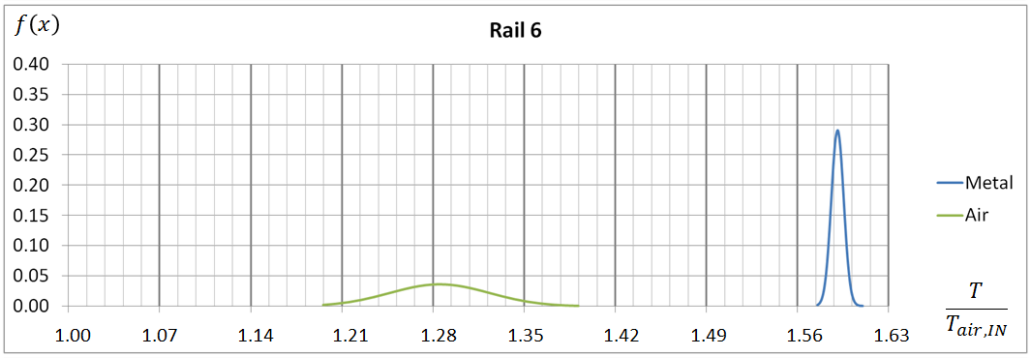
f(x)
Rail 6
0.40
0.35
0.30
0.25
0.20
0.15
0.10
0.05
0.00
1.00
1.07
1.14
1.21
1.28
1.35
1.42
1.49
1.56
1.63
Metal
Air
T / T_air,IN

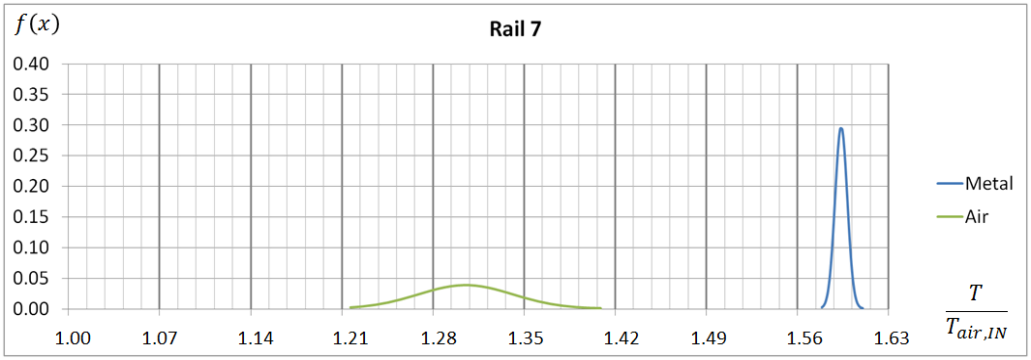
f(x)
Rail 7
0.40
0.35
0.30
0.25
0.20
0.15
0.10
0.05
0.00
1.00
1.07
1.14
1.21
1.28
1.35
1.42
1.49
1.56
1.63
Metal
Air
T / T_air,IN

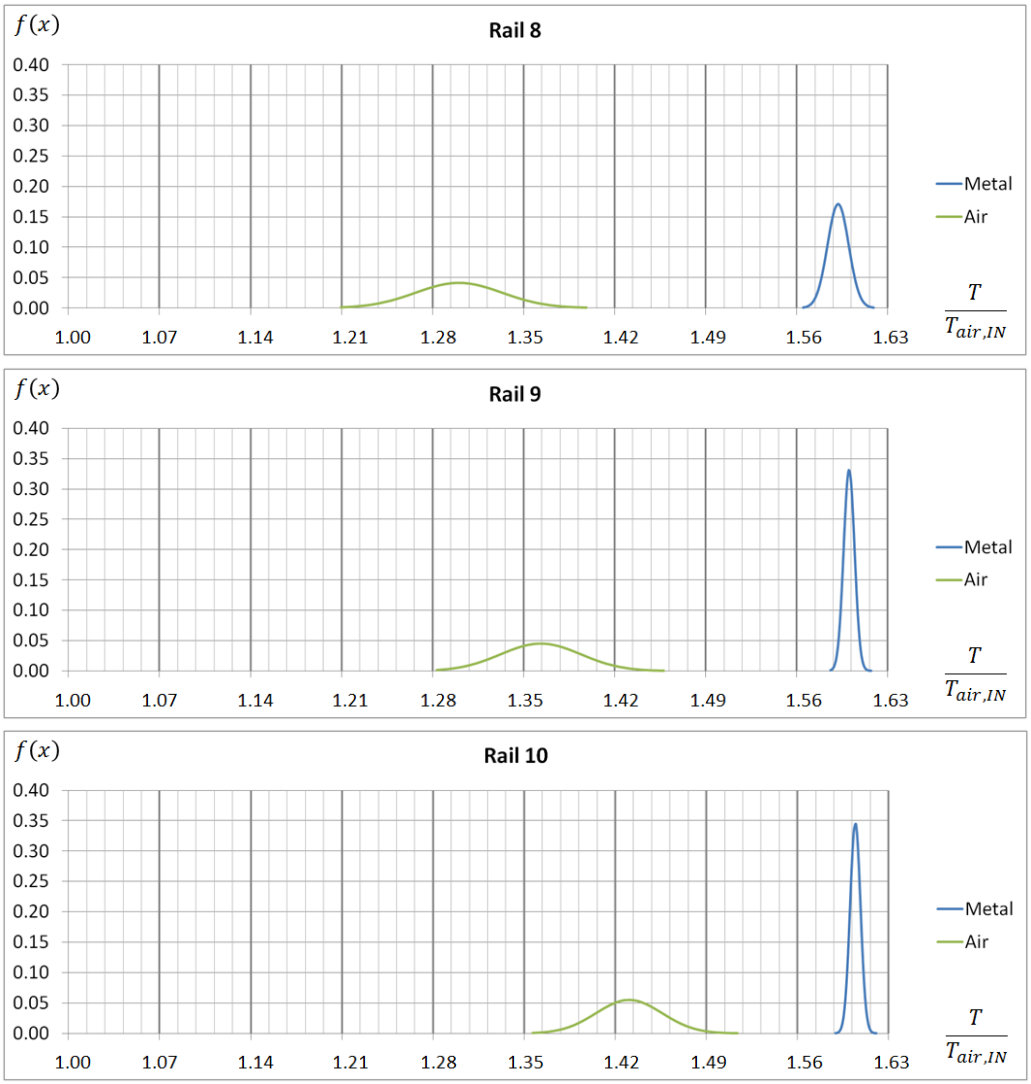

Figure 4.6 - Normal distributions of the temperatures in the region of the spider rails.

The first information, provided by each of these graphs, concerns the effect of the circumferential position. Instead, the impact of the parameters of the DoE can be neglected, as explained in the subparagraph 4.3.3, since the air temperature inside the axial headers is not significantly affected by the variations analyzed. The distributions recorded in Figure 4.6 for metal and air temperatures, i.e. the blue and the green curves, respectively, are quite different. The first ones exhibit lower standard deviations, so the data are less spread. On the contrary, the air is strongly affected by the permanence time inside the pipes, thus its temperature distributions have larger standard deviations, meaning a significant effect of the circumferential position.

The results, shown in Table 4.6, provide more details about the circumferential and axial variations of these temperature distributions. For each curve of the air temperatures, the variations have been calculated as:

$$\Delta T = T_{max} - T_{min} \tag{4.10}$$

In Equation 4.10, both the maxima and the minima are the average values, considering all the simulations of the DoE. In addition, the normalized mean values and the split of the mass flow rate inside an axial header are shown. The latter has been provided by the simulations run with the flow network solver.

For the air temperature, the results listed in Table 4.6 show that the circumferential non-uniformity is stronger within the first spider rails and significantly decreases in the last ones. This behavior can be explained considering that, in the initial parts of the axial headers, the temperature differences for the cooling air are more related to the permanence time in the manifold, rather than to the boundary conditions of the LPT region. The first effect is responsible of the large standard deviations recorded in the first rails. As the air flows downstream, the heat pick-up becomes stronger and the mean values of the air temperature increase. Here, the effect of the boundary conditions becomes pronounced, while the air temperature is more uniform along the circumference of the engine, since ΔT_{air} significantly decreases.

Table 4.6 - Air temperature mean values and variations of the normal distributions.

# Rail	$T_{air}/T_{air,IN}$	ΔT_{air} $[K]$
1	1.171	43.7
2	1.172	43.4
3	1.203	41.3
4	1.211	40.9
5	1.248	37.9
6	1.285	36.6
7	1.306	34.7
8	1.301	33.8
9	1.364	29.8
10	1.431	24.8

Chapter 5

Case Roughening

The last part of the PhD activity was focused on the enhancement of the heat transfer in the impingement region. The main methods to fulfil this objective have been presented in subparagraph 2.2.3. Based on the premise that the ACC system of a LPT may have a very large number of nozzles (in the order of ten thousand), the methods that resort to flow control are not easily applicable to this system. On the contrary, the enhancement of the heat transfer by means of adding roughening elements on the turbine casing seems to be more promising. As already seen, this method has been used in cooling for electronics, with compact jet arrangements.

Currently, the LPT casing is realized by casting its segments in titanium alloys [62]. The several segments are then welded by using the electron-beam (EB) technique [63]. Since its design is highly optimized in order to endure the harsh engine environment, it is not allowed to weld roughening elements on its external surface. Indeed, the EB welding without the necessary design precautions can create stress problems in the material [63]. However, the additive manufacturing technique has found a vast number of applications in the production of components for jet engines, e.g. for turbine blades [64]. When this technique will be used to manufacture the LPT casing, it will be possible to create this component as a whole piece that already has the roughening elements. In this way, a large number of possibilities in terms of geometry for the roughening elements are available.

In the present work, several geometries have been proposed and investigated as roughening elements to enhance the heat transfer during the jet impingement on the LPT casing. The analyses have been carried out with the CFD 3D approach. First of all, some interesting literature studies concerning the CFD method applied to impinging jets are discussed. After this step, the numerical model that has been utilized for the simulations is described in detail. Then, the CFD results for the several geometries are presented, including the casing with a flat surface, which is considered as the reference condition. Finally, the most promising alternative to the current design are compared and analyzed more in-deep.

5.1 CFD Modeling of an Impinging Jet in the Literature

As discussed in subparagraph 2.2.3, the impinging jet is an unsteady phenomenon, whose behavior can be affected by a large number of parameters. Besides the enormous number of experimental and analytical studies carried out to describe its physics, another tool that is very useful is the CFD approach.

Zuckerman and Lior [65] provided an exhaustive overview about the features of the available CFD models, which are synthesized in Table 5.1. The authors also discussed in detail the advantages and the drawbacks of each model, providing the references about the studies carried out in the literature.

Table 5.1 - Comparison among the most common CFD turbulence models ('*' for poor features, '**' for excellent features) made by Zuckerman and Lior [65].**

Turbulence Model	Computational cost (computation time required)	Impinging jet transfer coefficient prediction	Ability to predict secondary peaks in Nu
k-ε	**** Low cost	* Poor: Expect Nu errors of 15–60%	* Poor
k-ω	**** Low-moderate	** Poor-fair: Anticipate Nu errors of at least 10–30%	** Fair: May have incorrect location or magnitude
Realizable k-ε and other k-ε variations	**** Low	** Poor-fair: Expect Nu errors of at 15–30%	** Poor-fair: May have incorrect location or magnitude
Algebraic stress model	**** Low	** Poor-fair: Anticipate Nu errors of at least 10–30%	* Poor
Reynolds stress model (full SMC)	** Moderate-high	* Poor: Anticipate Nu errors of 25–100%	** Fair: May have incorrect location or magnitude
SST	*** Low-moderate	*** Good: Typical Nu_0 errors of 20–40%	** Fair
v^2f	*** Moderate	**** Excellent: Anticipate Nu errors of 2–30%	**** Excellent
DNS/LES time-variant models	* Extremely high	**** Good-excellent	**** Good-excellent

The direct numerical simulation (DNS) models allow obtaining an excellent agreement with the experimental data. However, since they require very small grids to solve the turbulence, the required computational time is very long. Consequently, the usage of these models is limited to cases with simple geometries and low Reynolds numbers.

In order to overcome this drawback, the large eddy simulation (LES) approach can be utilized. Here, the Navier-Stokes equations are treated basing on a length scale defined by the user in terms of grid spacing. The turbulence is solved using more detailed, additional sub-grid scales. Although this approach is promising, thanks to the accurate results provided, it is still highly-demanding in terms of computational time, due to the fine discretization needed for both space and time grids.

Besides this class of methods, there are the Reynolds-averaged Navier-Stokes (RANS) models. Typically, the basic $\kappa - \varepsilon$ model exhibits a low computational cost. However, it is not suitable to model the impinging jet, due its poor predictions in the stagnation region and in the wall boundary layer. Some improvements in these regions can be obtained by shifting to the RNG $\kappa - \varepsilon$ or other non-basic $\kappa - \varepsilon$ models, at the cost of a slightly higher computational time. However, these variations are recommended only when the required accuracy is not too high.

The $k - \omega$ model, compared to the $\kappa - \varepsilon$ approach, offers a better solution in the wall region and a moderately better Nusselt number prediction. However, this model requires higher computational time and can be affected by the far field boundary conditions. Moreover, the presence of secondary peaks in the Nusselt number may be predicted at different locations other than those recorded in the experimental tests.

Similarly, also the Reynolds stress transport models (RSTM) are not a good approach to simulate impinging jets, since large errors may occur in the prediction of: the velocity field, the Nusselt number and the locations of its secondary peaks, if any. In addition, the computational time that they require is significantly higher than that needed by the eddy viscosity models.

Another turbulence model is the $v^2 - f$, a four-equation model. The required computational time is relatively high, but this approach is recognized as one of the most promising in predicting the behavior of the local Nusselt number and of its secondary peaks, even at small nozzle-to-plate spacing. Thus, this model is highly recommended to simulate an impinging jet.

Considering that the impinging jet presents three different regions (free jet, stagnation point and wall jet, each of them with its own physical peculiarities), another approach, known as hybrid modeling, can be used to treat this problem. The idea at the basis of hybrid modeling is to combine the features of different turbulence models. In particular, a hybrid model is able to distinguish among the different jet regions, applying those equations that provide the best results. A hybrid model is the shear stress transport (SST), which combines the near-wall capabilities of the $k - \omega$ model with the strength of the $\kappa - \varepsilon$ model in the free jet region. The SST model provided quite accurate results. Compared to the $v^2 - f$ model, the performance are very similar, while the computational cost is lower. In other words, the $k - \omega$ SST model appears to be the best compromise between accuracy and required simulation time. Consequently, this turbulence model has been adopted for the CFD simulations carried out in this research activity.

Andreini et al [66] utilized the $k - \omega$ SST model for a CFD approach applied to an ACC system under different conditions of pressure ratio and cross flow velocity. These numerical analyses were in good agreement with their experimental data.

5.2 CFD Numerical Model

The purpose of the following numerical analyses is to compare the flat surface, which is currently utilized on the LTP casing, to several configurations, where roughening elements have been added to this surface, in order to enhance the heat transfer. Since the research is focused on this objective, the CFD model presents several differences with the real LPT casing and the undercowl chamber that will be soon explained.

The software that has been utilized to carry out the simulations is Ansys CFX 14.5. This commercial software allows performing finite element analysis, applied to engineering problems, with a CFD approach. It utilizes a coupled and parallelized solver and enhances convergence by using an algebraic multi-grid approach [67].

The main geometrical parameters of the jet arrangement are listed in Table 5.2, while the model and the boundary conditions are shown in Figure 5.1.

Table 5.2 - Main geometrical and physical settings for the CFD model.

d	1 mm
t	2 mm
S_x	Single row
S_y	5, 6 mm
S_z	10 mm
d_M	10 mm
L	50 mm
p_{UC}	100000 Pa
$p_{M,0}$	110000 Pa
β	1.1
u_{CF}	0, 5, 10 ,15 m/s
$T_{M,IN}$	298 K
T_{UC}	298 or 328 K
T_w	328 K

To begin with, in the LPT ACC system, the impinging nozzles are arranged in rows along the spider rails. In terms of numerical modeling, it is sufficient to analyze a single impinging jet while imposing lateral periodicity on a domain that has a lateral extension equal to the spanwise jet spacing S_z. The choice of $S_z = 10\ mm$ is realistic for the spider rails, even if the ACC system may operate with more compact rows of jets. In addition, this spacing allows analyzing the interaction between the jet and the roughening element, while no strong downwash related to adjacent jets is introduced.

Secondly, the curvature of the turbine casing has been neglected. This assumption is not strong, since the LPT casing has a large diameter.

The air enters the CFD domain through two inlets (Inlet ACC), which represent the spider rail section and where the total pressure $p_{M,0}$ and the temperature $T_{M,IN}$ have been set. With this choice, the nozzle is fed from both the sides and the pressure decrease occurring along the spider rail is not modeled.

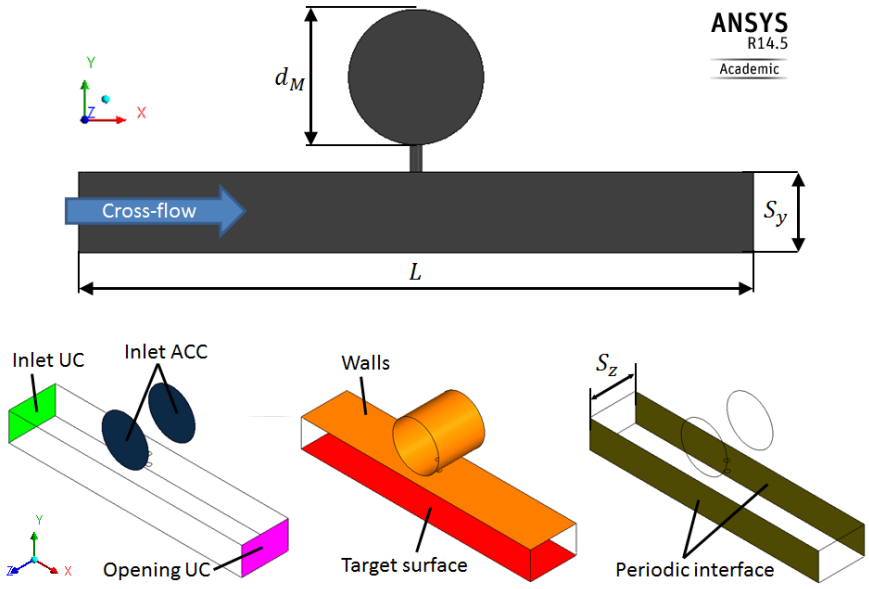

Figure 5.1 - CFD model for the casing with flat surface: lateral view (top) and boundary conditions (bottom).

The inlet cross-sections are circular with diameter d_M, whose choice has been made considering the limit in terms of area ratio discussed by Da Soghe et al [18]. In particular, a ratio, between the area of the feeding pipe and the sum of the ones of the considered impinging nozzles, of at least five was indicated as the minimum value to guarantee flow uniformity among the several nozzles.

Moreover, it has to be noticed that the spider rails are located inside the undercowl chamber, where the impinging jets are discharged and the cross flow acts (see Figure 2.9). This configuration induces local accelerations when the cross flow interacts with the spider rail cross-sections, which disturb the impinging jets. In the present work, the undercowl chamber has been modeled as a channel with constant height, equal to the nozzle-to-plate distance S_y. This way, the interaction between the impinging jet and the cross flow can be modeled while excluding other effects.

The nozzle has a length to diameter ratio $t/d = 2$, which means a good performance in terms of discharge coefficient. The jet impinges on the target surface, which has a constant temperature T_w and no slip conditions, i.e. the air velocity is zero at wall. The other walls are adiabatic.

On the streamwise direction, the CFD domain extends for twenty-five diameters in both ways, in order to avoid effects that could be related to the boundary conditions. These two boundaries are named Inlet UC and Opening UC. While the latter is always an opening boundary with fixed static pressure p_{UC} and temperature T_{UC}, the former can be either an opening with the same conditions as Opening UC or an inlet, depending on the fact that the cross flow is absent or included in the simulation. In case of cross flow, the boundary Inlet UC has assigned the temperature T_{UC} and the cross flow velocity. Considering the channel geometry and the cross flow velocities ranging from 5 to 15 m/s, a fully

developed turbulent velocity profile has been assigned at the inlet, defined with the power-law profile [68], where the local velocity *u* is calculated as:

$$u = u_{MAX}\left(\frac{y}{S_y}\right)^{1/n} \tag{5.1}$$

where *y* is the local vertical coordinate and *n* is the exponent of the power that depends on the Reynolds number of the undercowl channel Re_{UC}, which is calculated as:

$$Re_{UC} = \frac{u_{CF} \cdot d_{UC}}{\nu_{CF}} \tag{5.2}$$

In Equation 5.2, the hydraulic diameter of the undercowl has been assumed to be a wide channel, i.e. $d_{UC} = 4S_y$. The Reynolds number for the undercowl channel ranges from 6300 to 22900. The value $n = 7$ is reported as a fair choice for many practical applications [68]. Finally, the maximum velocity profile u_{MAX} depends on Re_{UC}:

$$u_{MAX} = u_{CF} \cdot \left[1 + 1.33 \cdot (100 \cdot Re_{UC})^{-1/8}\right] \tag{5.3}$$

Since this CFD model has been utilized to calculate the heat transfer occurring during the jet impingement, it is necessary to utilize a fine grid, especially near the stagnation region. Although the grid is generally composed by tetrahedrons, the volume near the walls has been meshed with prisms, which are more suitable to replicate the behavior of the boundary layer, thanks to their better qualities.

In order to obtain a thicker mesh in those regions where high velocity gradients are expected, several *bodies of influence* have been utilized during the meshing phase. These are non-physical bodies that allow utilizing specific mesh settings within their volume, instead of the coarser mesh realized with the global settings. The finest grid has been utilized for the core of the impinging jet, included within a cylindrical body of influence, shown in the left side of Figure 5.2. The region that is upstream the nozzle and the surroundings of the jet core have been modeled with a slightly larger grid, defined by the bodies in the middle of Figure 5.2. Finally, a larger volume, corresponding to a region where the jet still exerts its influence, has been meshed with a grid that is intermediate between the previous ones and the global settings (Figure 5.2, right).

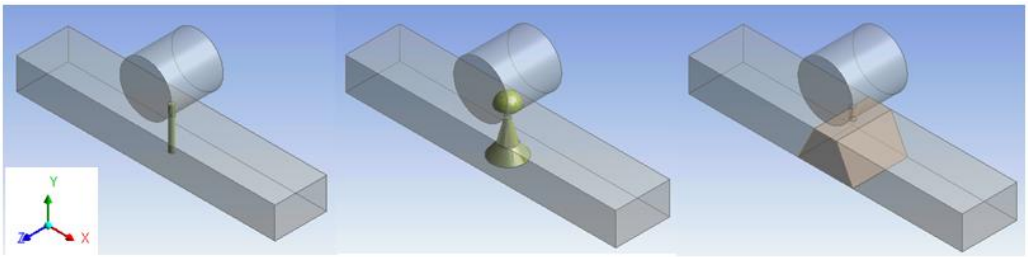

Figure 5.2 - Bodies of influence utilized to thicken the local mesh.

The *inflation* feature has been utilized to define the boundary layer on all the walls of the CFD domain. For each wall, the first layer thickness, the growth rate and the number of layers have been defined. In particular, the impinging nozzle has eight layers, while the other walls have twenty layers. In addition, a *face sizing* has been utilized on the target surface. In this way, it is possible to guarantee a low aspect ratio of the prisms, thus, a better mesh quality.

In order to find a good compromise between computational costs and results accuracy, a mesh sensitivity has been carried out, starting from a very fine mesh and gradually reducing the local sizings, as shown in Table 5.3. The quality of the obtained results has been verified by applying several criteria. The first one is to maintain the root mean square (RMS) residuals below 10^{-3} for all the equations. With a few exceptions, all the meshes exhibit residuals that are below 10^{-4}, as shown in Table 5.4. The second criterion consists into checking the overall domain imbalance for all the equations: conservation can be considered achieved for imbalances below 1%. All the analyzed grids meet this criterion (see Table 5.5).

Table 5.3 - Mesh sensitivity: features of the several models.

Model	#Nodes	#Elements	Time [h]*
Mesh #1	3459628	11951538	52
Mesh #2	1889334	6377104	27
Mesh #3	1223838	4058569	18
Mesh #4	892838	2901206	13
Mesh #5	514215	1656468	8
Mesh #6	359443	1141228	5

* Time required for 2000 iterations.

Table 5.4 - Mesh sensitivity: RMS residuals*.

Model	Momentum-u	Momentum-v	Momentum-w	Continuity	Energy
Mesh #1	0.21	0.05	0.14	0.011	0.07
Mesh #2	0.28	0.07	0.19	0.011	1.50
Mesh #3	0.24	0.07	0.20	0.016	1.20
Mesh #4	1.20	0.51	1.20	0.013	4.50
Mesh #5	0.39	0.13	0.31	0.031	1.30
Mesh #6	0.11	0.05	0.15	0.009	0.70

* All the values have to be multiplied by 10^{-4}.

Table 5.5 - Mesh sensitivity: overall domain imbalances*.

Model	Momentum equations	Continuity	Energy
Mesh #1	≅0	-0.0010	0.0070
Mesh #2	≅0	0.0022	0.3857
Mesh #3	≅0	0.0020	-0.0600
Mesh #4	≅0	0.0900	-0.5400
Mesh #5	≅0	0.0007	-0.0740
Mesh #6	≅0	0.0003	-0.2860

* The imbalances shown are in % of the maximum value recorded among all the boundaries of the CFD domain. Negative values indicate that the imbalance is exiting the CFD domain.

Besides these verifications, the convergence for each model has been verified, checking the local Nusselt number (average value in the streamwise direction, see

Figure 5.6 for the locations where the Nusselt number is calculated) and the mass flow rate through the nozzle. Generally, all the meshes reached steady values within 1000 iterations, except Mesh#1, which required around 1500 iterations to obtain convergence. The monitor values, which have been obtained for all the meshes, have been compared after 2000 iterations. While all the meshes provide very similar values in terms of mass flow rate through the nozzle, as listed in Table 5.6, the local Nusselt number obtained for Mesh#4 is higher than the others in the peak region (see Figure 5.3). This behavior can be explained considering that the RMS residuals recorded for Mesh#4 are considerably higher than the other ones.

Table 5.6 - Mesh sensitivity: mass flow rate through the nozzle, $\dot{m}_j$.

Model	$\dot{m}_j\ [kg/s]$
Mesh #1	$9.536 \cdot 10^{-5}$
Mesh #2	$9.535 \cdot 10^{-5}$
Mesh #3	$9.531 \cdot 10^{-5}$
Mesh #4	$9.571 \cdot 10^{-5}$
Mesh #5	$9.621 \cdot 10^{-5}$
Mesh #6	$9.666 \cdot 10^{-5}$

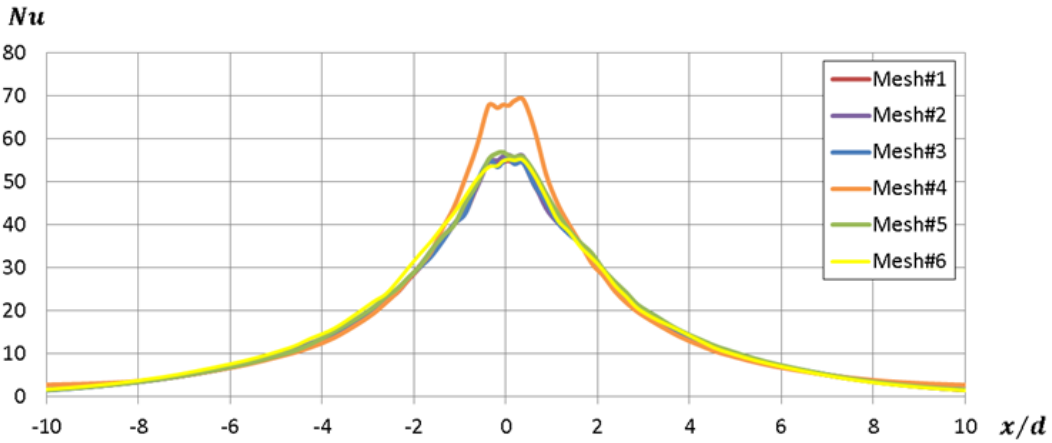

Figure 5.3 - Mesh sensitivity: comparison of the local Nusselt number.

Also, the choice of the proper mesh settings has been influenced by the utilized turbulence model, the SST $\kappa - \omega$, chosen for the advantages pointed out in paragraph 5.1. Since this is a low-Reynolds model, it does not utilize a near-wall function and requires that the boundary layer, including its viscous sub-layer, is fully solved by using a fine grid that guarantees $y^+ < 1$ [69]. It has been verified that this condition is ensured only by meshes #1, #2 and #3. For this reason, Mesh#3 has been chosen as the best compromise between the accuracy of the results and the computational costs for the present study. The main features of Mesh#3 are listed in Table 5.7, referring to the model that represents the flat turbine casing.

Table 5.7 - Mesh#3: settings and features.

Global features	
#Elements	$4.050\ M$
#Nodes	$1.225\ M$
Average Skewness	$0.194\ \pm 0.112$
Body sizing	
Body of influence, finest	$6.25 \cdot 10^{-5}\ m$
Bodies of influence, fine	$1.00 \cdot 10^{-4}\ m$
Body of influence, medium	$1.25 \cdot 10^{-4}\ m$
Global, max size	$4.00 \cdot 10^{-4}\ m$
Inflation	
First layer thickness	$1.00 \cdot 10^{-5}\ m$
Growth rate	1.1
Number of layers	8 (nozzle wall) 20 (other walls)
Face sizing (target surface)	$1.25 \cdot 10^{-4}\ m$

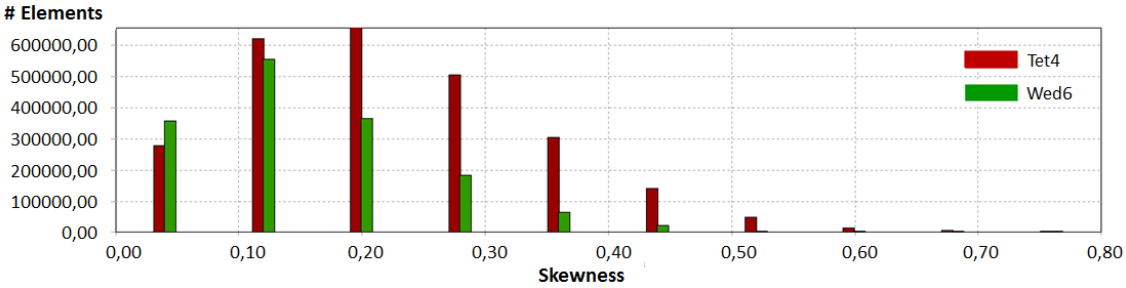

Figure 5.4 - Skewness distribution for the current mesh.

The utilized grid exhibits a low average skewness, while its distribution among the elements is plotted in Figure 5.4 (Tet4 are tetrahedrons, while Wed6 are prisms). The most of the elements, especially for the prisms composing the boundary layer, show a very good skewness [70].

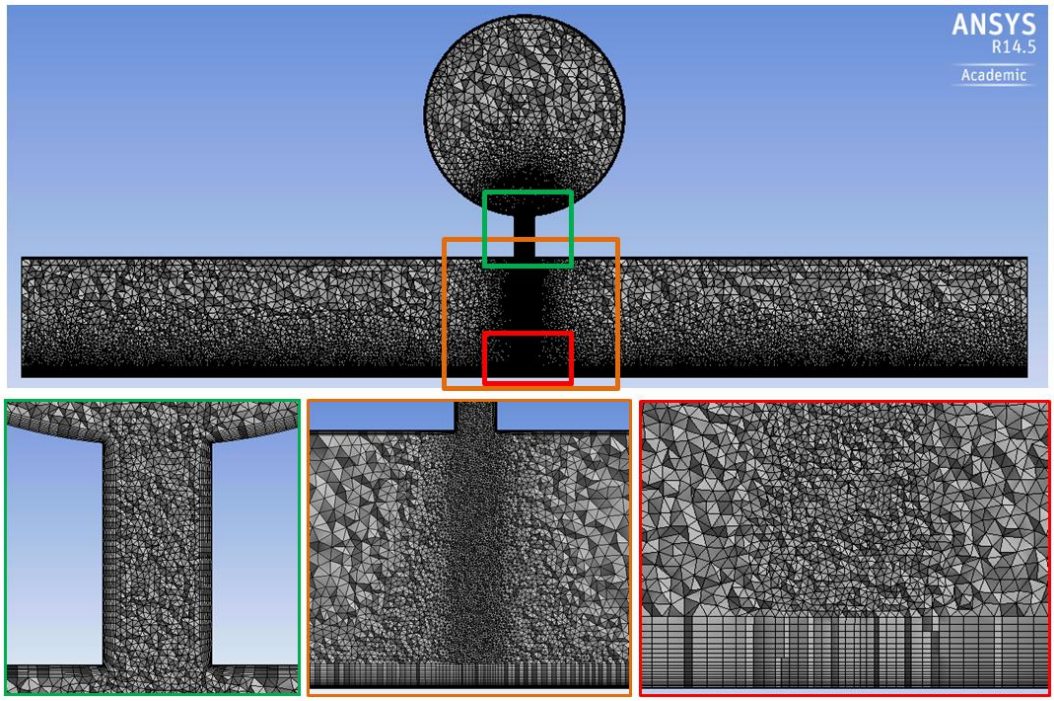

Figure 5.5 - Current mesh with details of the jet region.

The obtained mesh is shown in Figure 5.5, which is a lateral view of the CFD domain with details about the nozzle, the jet core and the stagnation region (the rectangles in green, orange and red, respectively).

Besides the definition of geometry, boundary conditions and mesh, there are also other information about the CFD model to be included.

The analyses are performed at steady-state, on the basis of the energy equation, and considering as working fluid the air supposed as an ideal gas, with its transport properties assumed as functions of the temperature.

The advection scheme is of the second order.

The simulations have been stopped basing on the monitored residuals.

5.3 Analyzed Configurations

In order to calculate the heat transfer coefficients in the CFD model, the target surface has been divided in 48 areas. These subdivisions have been made in the streamwise direction, while each area covers the entire spanwise direction of the CFD domain, as shown in Figure 5.6. The HTCs have been obtained by implementing Equation 2.15 in the Ansys CFX Post and by applying it to each area. Then, by using Equation 2.14, a set of data was available to realize the plot of the local Nusselt number along the streamwise direction for each run. Generally, the curves have been plotted by using the streamwise coordinate divided by the jet diameter x/d, with $x/d = 0$ representing the coordinate below the impinging jet. Moreover, the average value of each curve has been calculated with the following formula:

$$\overline{Nu} = \left[\sum_{i=2}^{n} \frac{Nu_i + Nu_{i-1}}{2}(A_i - A_{i-1})\right] \Big/ A_T \tag{5.4}$$

where the subscripts *i* and *i* - 1 indicate the local points for calculations, i.e. local Nusselt numbers and areas, while A_T is the total portion of the target surface, on which the calculation has been carried out. In Equation 5.4, *n* is the maximum index of the sum that is not necessarily equal to 48 (i.e. all the areas). Indeed, the comparison among the obtained results was more effective when a reduced portion of the target surface was considered, which extended in the range $x/d \leq \pm 5$.

It has to be noticed that the local areas for Nusselt calculations also include the geometries of the roughening elements, where they are present. In general, the increase, in terms of area of the target surface related to the addition of roughening elements, has been calculated in the range $x/d \leq \pm 5$ with the following relation:

$$\Delta A_{\%} = \frac{A_{rough} - A_{flat}}{A_{flat}} \cdot 100 \tag{5.5}$$

where the subscripts *rough* and *flat* indicate the roughened and the flat surfaces, respectively.

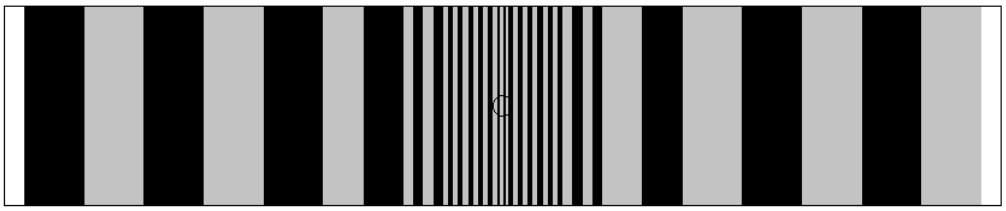

Figure 5.6 - Subdivisions on the target surface of the CFD model.

The Reynolds numbers for the jet and the undercowl have been calculated by using Equation 2.8 (shown in Table 5.8), while the nozzle discharge coefficient has been evaluated with Equation 2.9.

Table 5.8 - Reynolds numbers for the jet and the undercowl.

Re_j	5600			
Re_{UC} $(T_{UC} = 298\ K)$	$u_{CF} = 5\ m/s$	$u_{CF} = 10\ m/s$	$u_{CF} = 15\ m/s$	$u_{CF} = 20\ m/s$
MVR	18	9	6	4.5
$S_y/d = 5$	6300	12700	19100	25500
$S_y/d = 6$	7600	15300	22900	30600

To conclude, an important remark is necessary to point out a difference between the manufacturing process and the numerical modeling. From a practical point of view, the turbine casing cannot be carved. Accordingly, when the study concerns those roughening elements that require carving the surface under the impinging jets (e.g. dimples), they should be manufactured on portions of materials added on the flat surface.

In terms of numerical modeling, the addition of this portion can add further interactions between the cross flow and the impinging jet, adding an effect similar to the local flow acceleration near the spider rails submerged into the cross flow. Since the objective of the CFD analyses was to determine how the designed roughening elements interacted with the impinging jet and with a constant cross flow, this constraint has been removed, and an undercowl channel with a constant height has been considered during numerical modeling.

On one hand, this means, for the flat surface, that the nozzle-to-plate distance is constant and has the same value of the channel height. On the other hand, due to the presence of roughness under the impinging jets, this value may be locally variable. Since the impact of S_y on the heat transfer is very important, these local variations of the nozzle-to-plate distance have to be considered during the comparison of the obtained results.

First of all, the effective distance between the nozzle and the target surface has been defined as:

$$S_{y,eff} = S_y + h_r \tag{5.6}$$

where h_r is the depth of the roughening element under the impinging jet. If the roughening element is not carved, i.e. it is obtained by adding material, h_r will be negative, since the distance between jet and surface lower is than the nominal

value. In general, the roughening elements have been simulated with an undercowl channel with a height equal to 5 mm. In this way, it has been obtained that $5\ mm < S_{y,eff} < 6\ mm$.

Consequently, the simulations for the flat surface consider these two values of S_y, in order to provide a fair comparison with all the conditions with the roughened casing.

5.3.1 Flat Surface

The first part of the CFD analyses has been focused on the flat surface. This case will be the reference condition to be compared to the other results. The simulations have been performed considering the values of S_y and all the cross flow velocities listed in Table 5.2.

The model has been compared to the correlation developed by Florschuetz et al in 1981 [42], in order to assess its fair agreement with the literature data, as shown in Figure 5.7. The graph plots the overall Nusselt number versus the cross flow to jet mass velocity ratio (defined in Equation 2.7). For the CFD calculation, the Nusselt number has been calculated in the streamwise range $x/d \leq \pm 5$ and in the entire spanwise range. The air temperature for the cross flow is $T_{UC} = 298\ K$. To begin with, the condition $S_y = 5\ mm$ exhibits a slightly higher Nusselt number than the geometry with $S_y = 6\ mm$, due to the reduced nozzle-to-plate distance. As the cross flow is strengthened, the heat transfer decreases due its effects on the jet structure, as discussed in subparagraph 2.2.3, with a slope that is in agreement with the literature correlation. The CFD results underestimate the correlation, with a mean relative error (calculated with Equation 5.7) of -14.8% for $S_y/d = 6$ and -10.6% for $S_y/d = 5$.

$$err_{Nu} = \frac{Nu_{CFD} - Nu_{corr}}{Nu_{corr}} \cdot 100 \tag{5.7}$$

This difference can be explained considering that the authors carried out their studies in the range $1 \leq S_y/d \leq 3$. Since in this condition the jet is closer to the target surface, it can be expected that the Nusselt numbers are greater than those recorded in the present work. In order to confirm this explanation, the cases with $S_y/d = 3$ and cross flow velocity of 10 and 15 m/s have been simulated. Here, the recorded Nusselt numbers were closer to the authors' results, with a relative error of about -4% and +0.3%, respectively. Overall, the obtained results are in reasonable agreement with the literature and within the predicted range of accuracy for the SST $k - \omega$ in Table 5.1.

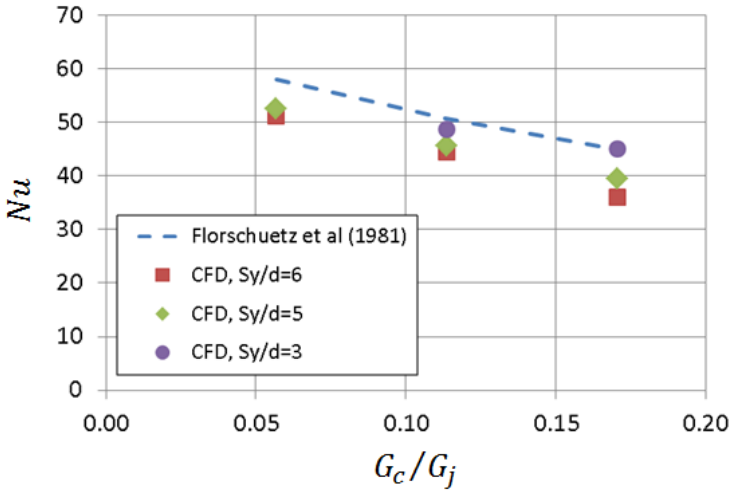

Figure 5.7 - CFD model validation: flat surface, overall Nusselt number under cross flow.

The overall Nusselt numbers for the simulated configurations, calculated in the range $x/d \leq \pm 5$, are reported in Table 5.9.

As already explained, the smaller nozzle-to-plate distance exhibits slightly higher Nusselt numbers in all the conditions. In particular, the graph in Figure 5.8 points out this difference in the peak region.

Also, the data recorded in Table 5.9 tell that the Nusselt numbers recorded for the simulations without cross flow are significantly lower than the others. Generally, it is expected that the cross flow has a detrimental effect on the Nusselt number, with the latter that decreases as the former increases. However, this result is in agreement with the observation made by Goldstein and Behbahani [31]. According to their experimental tests, a moderate cross flow with a small S_y could increase the Nusselt number recorded in absence of cross flow.

In order to provide a more in-depth analysis and to verify the agreement of the present model with the literature, other simulations have been carried out and the obtained average Nusselt numbers along the streamwise direction are shown in Figure 5.9. Larger jet spacings ($S_y/d = 10$ and 12) have been investigated, and a higher cross flow velocity has been involved, $u_{cf} = 20\ m/s$. As found in the literature [31], the maximum value of the Nusselt number under moderate cross flow is higher than the one without cross flow. For the present work, this conclusion applies not only for $MVR > 9$ (as the authors state), but can be extended to the cases with $MVR = 6$, at $S_y/d \leq 6$. The recorded trend becomes less remarked at larger nozzle-to-plate spacings.

This result can be explained considering that the cross flow is cooler than the target surface (more exactly, it has the same temperature of the jet). Consequently, it increases the heat transfer in two ways. The first one is the forced convection that occurs when the cross flow enters the CFD domain and increases with the cross flow velocity. This contribution can be clearly noticed in the graphs plotted in Figure 5.9, referring to the range $-25 \leq x/d \leq -8$. The second effect is the increase of the Nusselt number near the stagnation region. This contribution is

related to the cross flow air entrained by the impinging jet. Being the two temperatures (i.e. jet and cross flow) very similar, the entrainment of external air within the jet shear layer has no negative effect on heat transfer.

A further verification is the case $S_y = 6\,mm, u_{CF} = 0.1\,m/s$ and $T_{UC} = 298\,K$ (shown in the graphs of Figure 5.9). As expected, the Nusselt number distribution is very similar to the one recorded in the case without cross flow.

An additional run, simulated with $S_y = 6\,mm, u_{CF} = 10\,m/s$ and $T_{UC} = 328\,K = T_w$ confirms this explanation. The curve representing its local Nusselt number is plotted in Figure 5.10, together with those of the same case at $T_{UC} = 298\,K$ and of the run without cross flow. It can be clearly noticed the detrimental effect of the higher air temperature on the performance of the impinging jet (as shown in Figure 5.11, where the contours of the static temperature for the two runs are plotted). The overall Nusselt number, for the configuration $T_{UC} = 328\,K$, is equal to 15.4.

Table 5.9 - Overall Nusselt numbers obtained from CFD, flat surface.

	$u_{CF} = 0\,m/s$	$u_{CF} = 5\,m/s$	$u_{CF} = 10\,m/s$	$u_{CF} = 15\,m/s$
$S_y/d = 6$	28.8	51.2	44.5	36.0
$S_y/d = 5$	29.5	52.5	45.7	39.5
$S_y/d = 3$	-	-	48.7	-

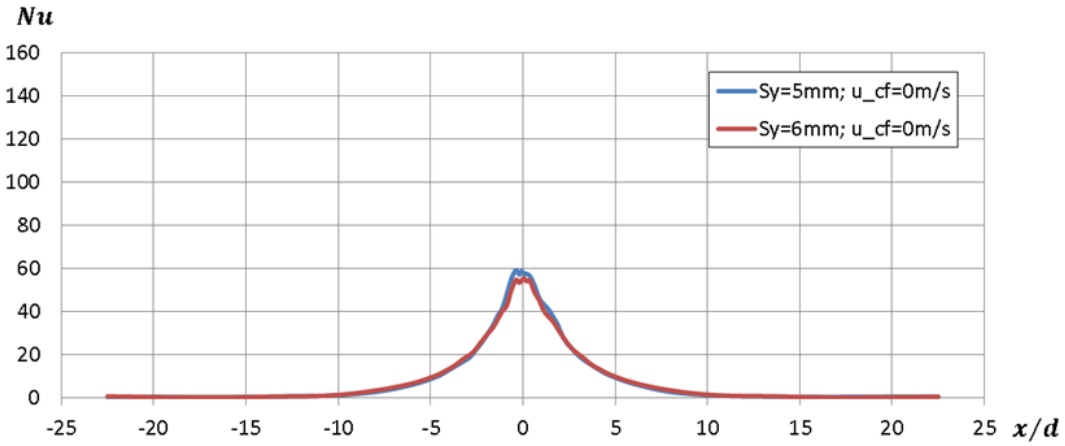

Figure 5.8 - Nusselt number without cross flow, flat surface.

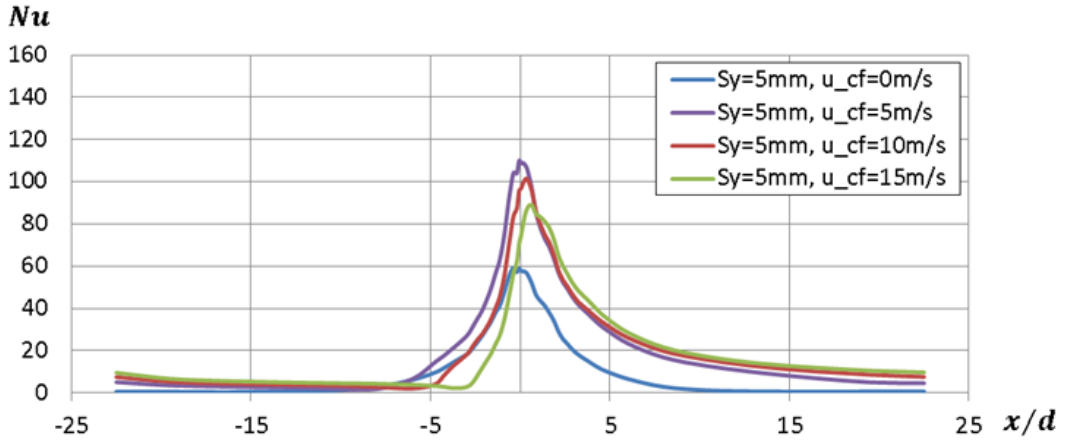

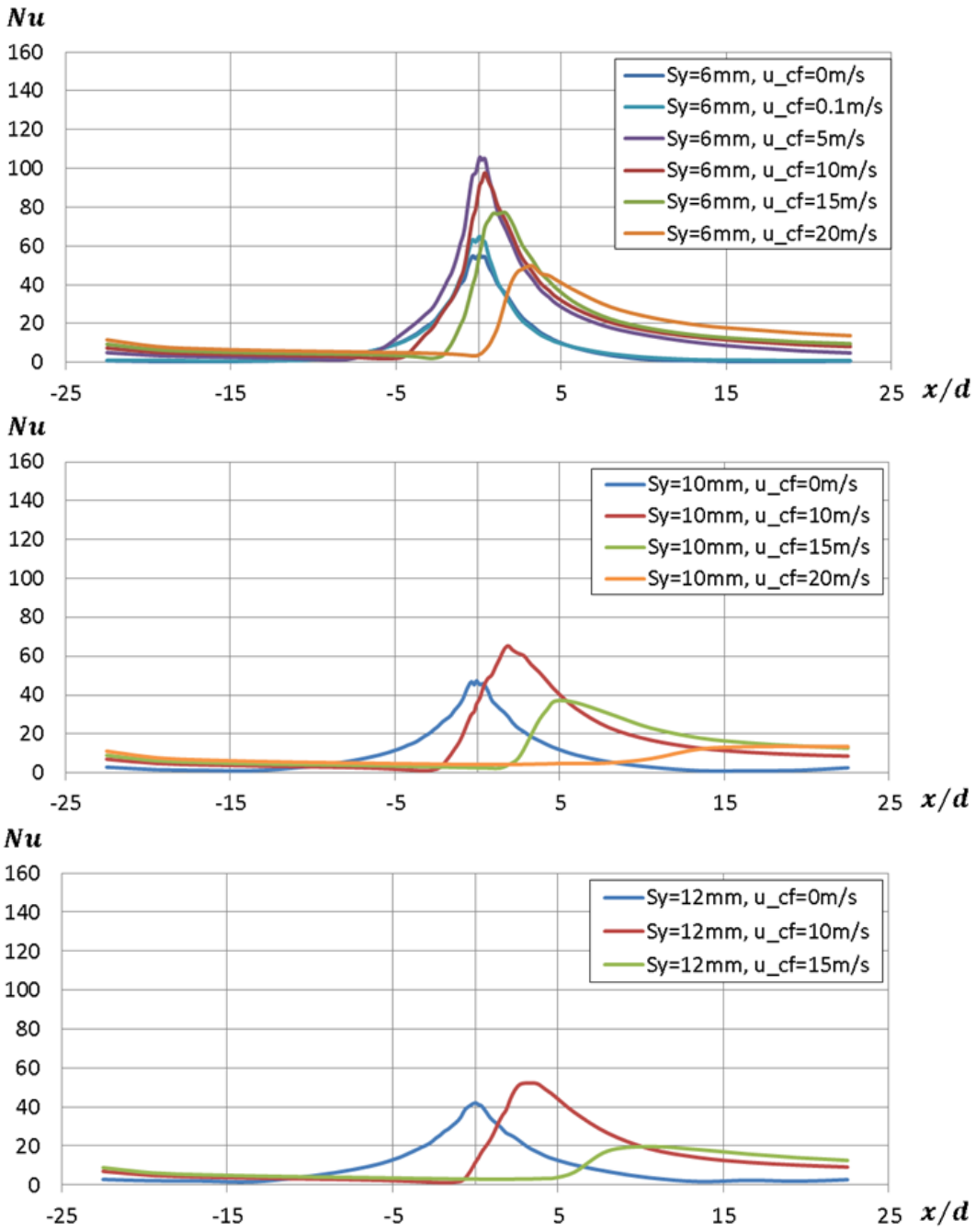

Figure 5.9 - Nusselt number with cross flow, flat surface.

Also, the graphs in Figure 5.9 show the typical effects of the increasing cross flow velocity. From 5 to 20 m/s, the jet becomes more deflected, the peak has a smaller value and the impingement point shifts downstream.

The mass flow rate recorded is about $9.6 \cdot 10^{-5}\, kg/s$, with very slight variations among the runs. The discharge coefficient changes for the two configurations: for $S_y = 6\, mm$ is 0.78, while for $S_y = 5\, mm$ is 0.75. These values are in good agreement with the literature [36, 37].

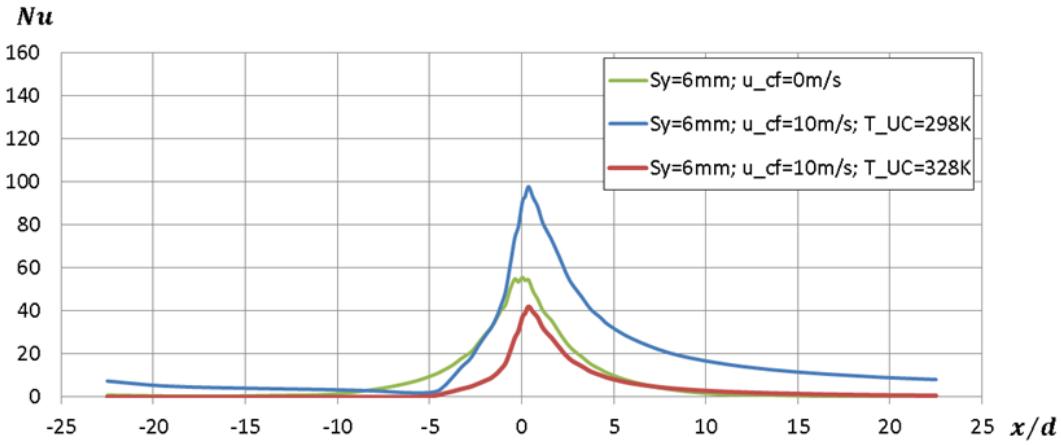

Figure 5.10 - Nusselt number, flat surface, effect of the cross flow temperature.

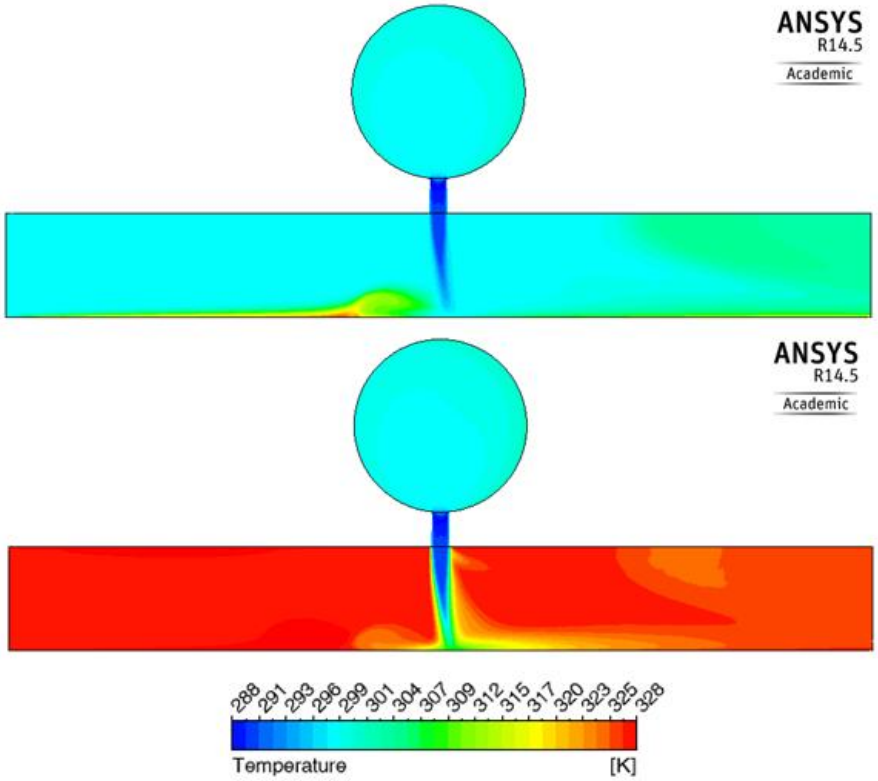

Figure 5.11 - Contour plots for the static temperature: top, $T_{UC} = 298\ K$; bottom, top, $T_{UC} = 328\ K$.

5.3.2 Dimpled Surface

The first roughening elements that have been analyzed are the dimples. The investigated patterns consisted in a single dimple placed under the impinging jet, as shown in Figure 5.12, top left. In all the simulations, the dimple diameter d_D has been kept constant, while its shape has been changed, with the consequent variations in terms of depth h_r and increase in wetted area $\Delta A_{\%}$ (as previously said, this value has been calculated in the range $x/d \leq \pm 5$). All the geometrical

parameters are listed in Table 5.10. The height of the undercowl channel is 5 mm, while $S_{y,eff}$ has been calculated with Equation 5.6.

While the hemispherical and the two elliptical dimples are an investigation into the effect of the dimple depth, the spherical-cap dimple is a study of the effect of the shape. The latter can be compared to the pattern *elliptical 2*, since they have the same value of h_r. The spherical cap has been designed as shown in Figure 5.12, top right. Here, the values of d_D and h_r have been held constant, while the diameter of the generating sphere d_C is calculated in order to respect the geometrical constraints shown in the figure. Compared to the elliptical shape with the same depth, the spherical cap exhibits a smaller wetted area and a less steep angle with the flat surface.

Table 5.10 - Geometrical parameters for the dimple patterns.

	$d_D\ [mm]$	$h_r\ [mm]$	$d_C\ [mm]$	$S_{y,eff}\ [mm]$	$\Delta A_{\%}$
Hemispherical (Hemi)	2	1	-	6	2.87
Elliptical 1 (Ell 1)	2	0.5	-	5.5	1.10
Elliptical 2 (Ell2)	2	0.25	-	5.25	0.38
Spherical cap 2 (Cap 2)	2	0.25	1.875	5.25	0.18

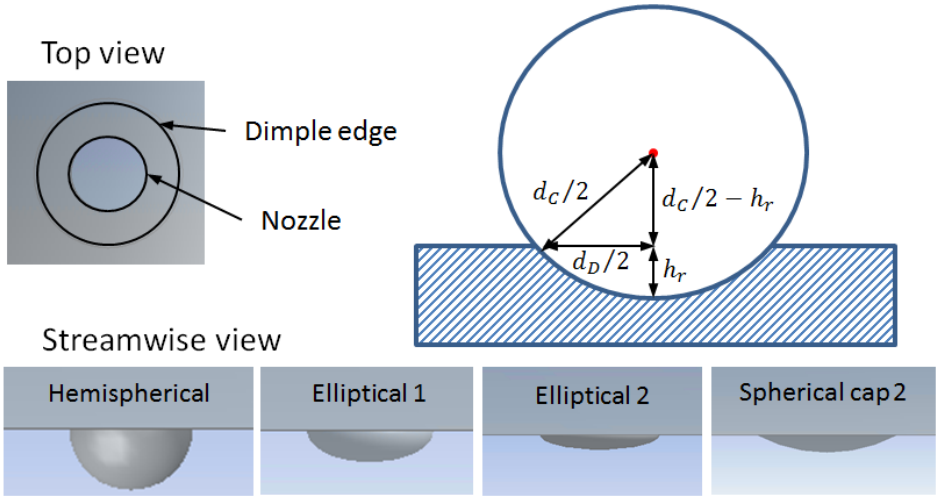

Figure 5.12 - Dimple and nozzle positions (top left); geometrical parameters and design of the spherical cap (top right); analyzed dimple patterns (bottom).

After the first simulations without cross flow, some patterns appeared to be promising to achieve the heat transfer enhancement. However, the same geometries under cross flow lost their advantage over the flat surface. This result can be related to the fact that the stagnation point has shifted downstream and has generated undesired interactions with the roughening elements. For this reason, further configurations have been investigated. Here, the roughening elements have been axially shifted, to a downstream location, in order to compensate the deflection of the jet under cross flow. Among the dimple patterns, this idea has

been applied to *Ell 2*, which has been shifted forward by 0.4 mm, creating the pattern *Ell 2 tr*, as shown in Figure 5.13.

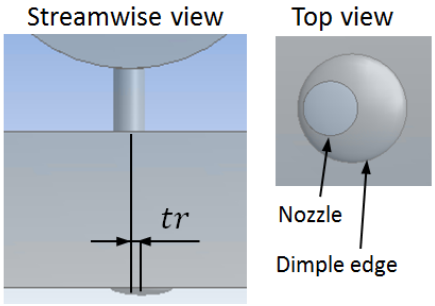

Figure 5.13 - Forward-shifted dimple pattern.

To begin with, Figure 5.14 shows the local Nusselt numbers for the several patterns compared to the flat surface without cross-flow. Note that all the graphs have been clipped to the range $x/d \leq \pm 10$, in order to better show the peak region. Generally, the shallower dimples (i.e. *Ell 2* and *Cap 2*) have performed better than the deeper dimples. In particular, the Nusselt number recorded in the peak region for the hemispherical dimple is significantly lower than that of the flat surface. The performance of the pattern *Ell 1* was slightly worse than that of the case without roughness. This behavior is in agreement with the studies performed by Kanokjaruvijit and Martinez-Botas [48]. According to the authors, the shallower dimples perform better for two reasons. First of all, the jet is closer to the target surface (i.e. $S_{y,eff}$ is smaller). Secondly, the deeper dimples promote larger regions of recirculating flow, which is a penalty for the heat transfer. This fact can be also noticed for *Hemi* and *Ell 1*, in the range $\pm 1 \leq x/d \leq \pm 2$, which is radially located just outside the edge of the dimple. Here, the two curves exhibit a Nusselt number that is smaller than that recorded for the flat surface.

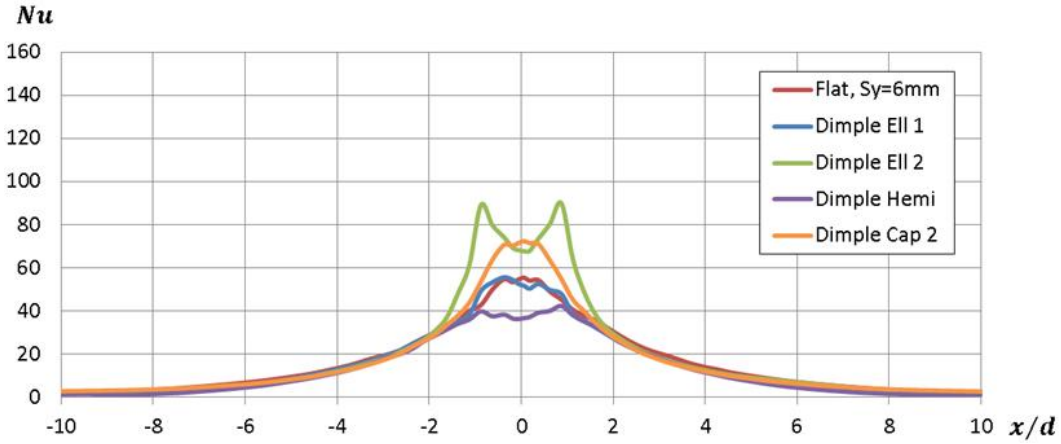

Figure 5.14 - Nusselt number: dimple patterns, no cross flow.

Moreover, the pattern *Ell 2* presents two peaks, which are approximately located at $x/d = \pm 0.9$, i.e. within the dimple. This effect can be explained by looking at the velocity contours shown in Figure 5.18, left column. In the configurations *Hemi* and *Ell 1*, the wall boundary layer forms outside the dimples, while the heat transfer within dimples is limited. In the case *Ell 2*, the boundary layer acquires a significant velocity when already inside the dimple, promoting a

higher Nusselt number. Actually, a similar phenomenon also occurs inside *Cap 2*, but here the curvature is significantly smaller and the flow develops without any detachment at its edge. Note that these peaks are not axisymmetric, since they do not develop in the spanwise direction, due to the interaction with the other jets of the row.

The curves, which are plotted in Figure 5.15, refer to dimple patterns under cross flow ($u_{CF} = 10\,m/s$, $T_{UC} = 298\,K$). The deflection induced by the undercowl air can be noticed in all the analyzed cases, with the peak in the stagnation region that moves downstream. As in the case without cross flow, the geometry *Ell 2* exhibits the highest peak value.

With the only exception of *Cap 2*, all the other dimples show a fall in the Nusselt number near $x/d = -1$. This fact can be explained by using the velocity contours in the middle column of Figure 5.18. Here, the interaction between the cross flow and the jet downwash results in a complete detachment of the wall boundary layer, which is promoted by the high curvature of the hemispherical and elliptical dimples. This phenomenon is also influenced by the fact that the impingement point is not near the center of the dimple, with a resulting flow field that is quite different from that shown in the contours without cross flow. On the contrary, the small curvature of *Cap 2* prevents the detachment, resulting in a higher heat transfer in the region $-7 < x/d < -1$. The described behavior can be also noticed in the temperature contours, shown in Figure 5.19 (central column). It has not been observed on the flat surface, since this cross flow velocity revealed to be not sufficient to induce the boundary layer detachment in this region.

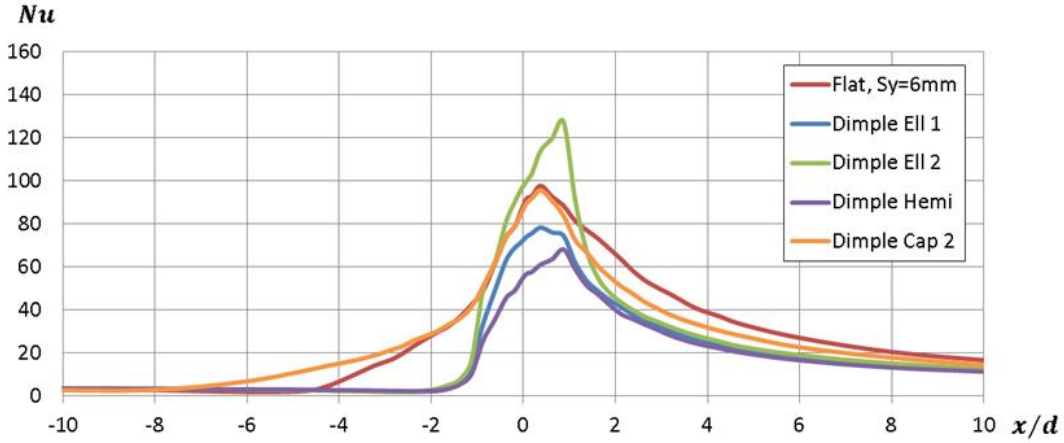

Figure 5.15 - Nusselt number: dimple patterns, $u_{CF} = 10\,m/s$, $T_{UC} = 298\,K$.

When analyzed without cross flow, the configuration *Ell 2* seemed promising in terms of heat transfer enhancement. However, it has lost its advantage over the flat surface when the cross flow has been introduced. In order to compensate the jet deflection, partly responsible for this negative result, the configuration *Ell 2* has been shifted in the streamwise direction, placed under the predicted impingement point. The other configurations have not been investigated, since their performance was already not interesting without cross flow. The translation applied was $tr = 0.4\,mm$. Figure 5.16 shows that this forward shift has a

beneficial effect on the Nusselt number: the heat transfer in the stagnation region is still high, while the detachment of the boundary layer outside the dimple is prevented, as can be seen in the contours in Figures 5.18 and 5.19 (middle column, last row). In this sense, *Ell 2 tr* behaves more like the dimple *Cap 2*.

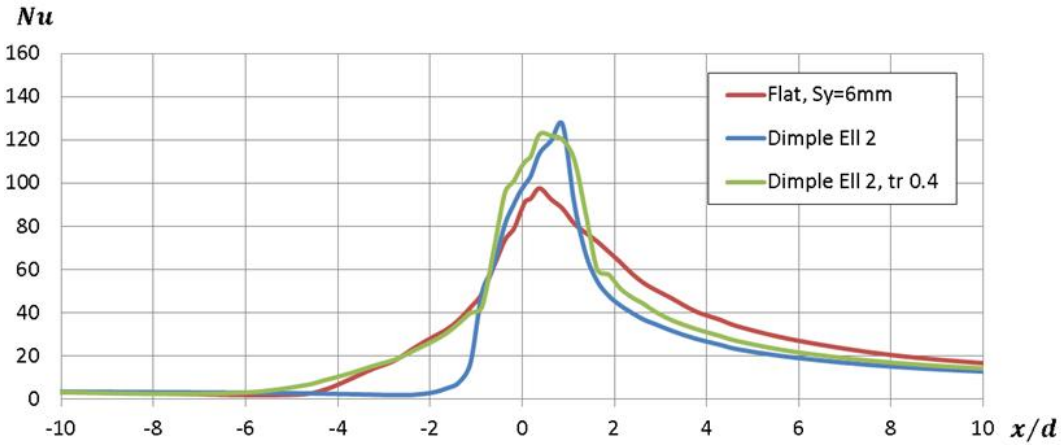

Figure 5.16 - Nusselt number: streamwise translation of *Ell 2*, $u_{CF} = 10\,m/s$, $T_{UC} = 298\,K$.

Then, the promising configurations that have been pointed out, i.e. *Ell 2 tr* and *Cap 2*, have been analyzed in the condition with a cross flow at the same temperature of the target surface $T_{UC} = 328\,K$. The results, shown in Figure 5.17, indicate that both the configurations perform significantly better than the flat surface, not only in the peak region, but also in the peripheral region of the jet.

Compared to the simulations with $u_{CF} = 10\,m/s$ and $T_{UC} = 298\,K$, there are no significant variations in the velocity contours (Figure 5.18, right column).

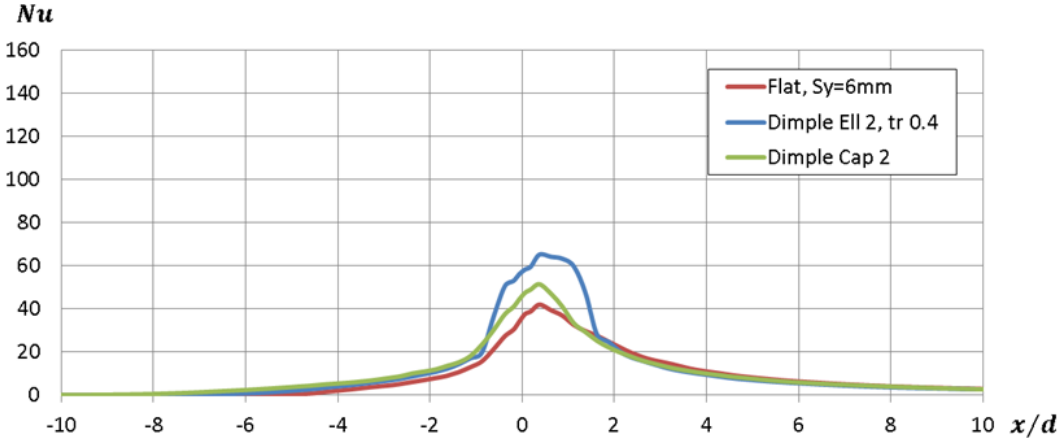

Figure 5.17 - Nusselt number: dimple patterns, $u_{CF} = 10\,m/s$, $T_{UC} = 328\,K$.

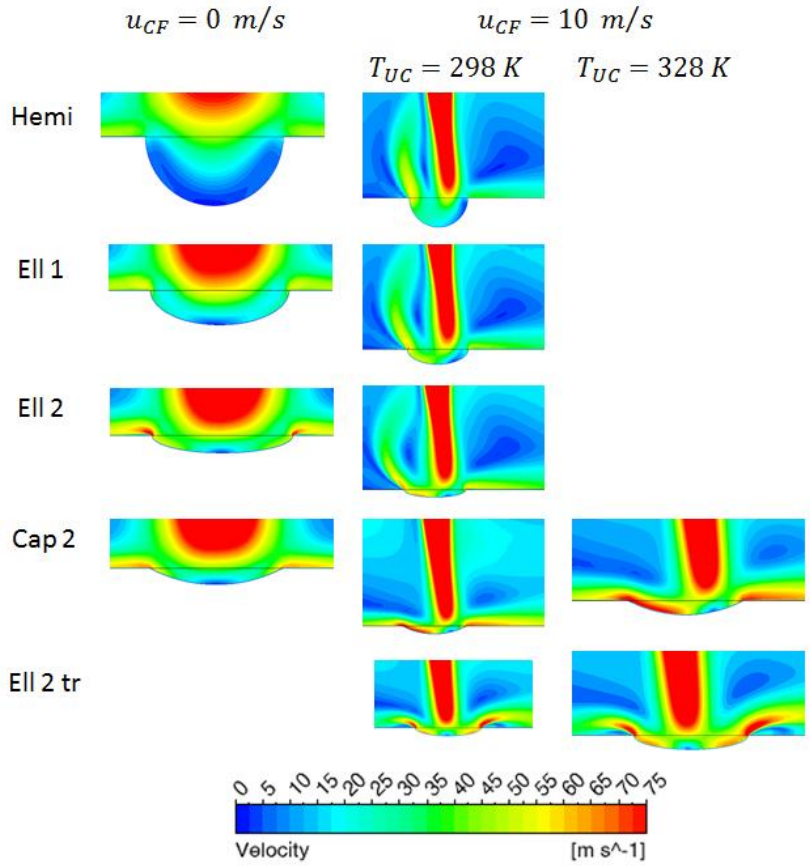

Figure 5.18 - Velocity contours for the dimple patterns.

Besides the graphs and the contours, the overall Nusselt numbers have been calculated in the range $x/d \leq \pm 5$. The obtained results are listed in Table 5.11.

In the case without cross flow, the configurations with shallower dimples appeared to be more promising. In particular, the heat transfer was enhanced by about 21.9% in the case *Ell 2*.

As the cross flow was introduced, the shallower dimples were still better than the others. However, all the investigated geometries exhibited an overall Nusselt number that was, in the best case, very similar to that of the flat surface. This general worsening turned out to be an effect of the interaction between the cross flow and the jet boundary layer, which was deflected by the curvature of the dimple. The forward shift of the roughening element in the case *Ell 2* significantly improved the performance.

Table 5.11 - Overall Nusselt numbers obtained from CFD, flat surface vs dimple patterns.

	$u_{CF} = 0\ m/s$	$u_{CF} = 10\ m/s$ $T_{UC} = 298\ K$	$u_{CF} = 10\ m/s$ $T_{UC} = 328\ K$
Normal $S_y/d = 6$	28.8	44.5	15.4
Hemi	24.3	25.1	-
Ell 1	27.7	28.8	-
Ell 2	35.1	36.4	-
Cap 2	30.6	43.2	18.4
Ell 2 tr	-	46.5	21.1

When the most promising configurations have been simulated under cross flow with high temperature, the heat transfer was considerably enhanced: the dimple with the shape of a spherical cap exhibited a 19.5% improvement, while a +37% in the overall Nusselt number has been recorded for the elliptical dimple *Ell 2 tr*, which has been properly shifted in the streamwise direction.

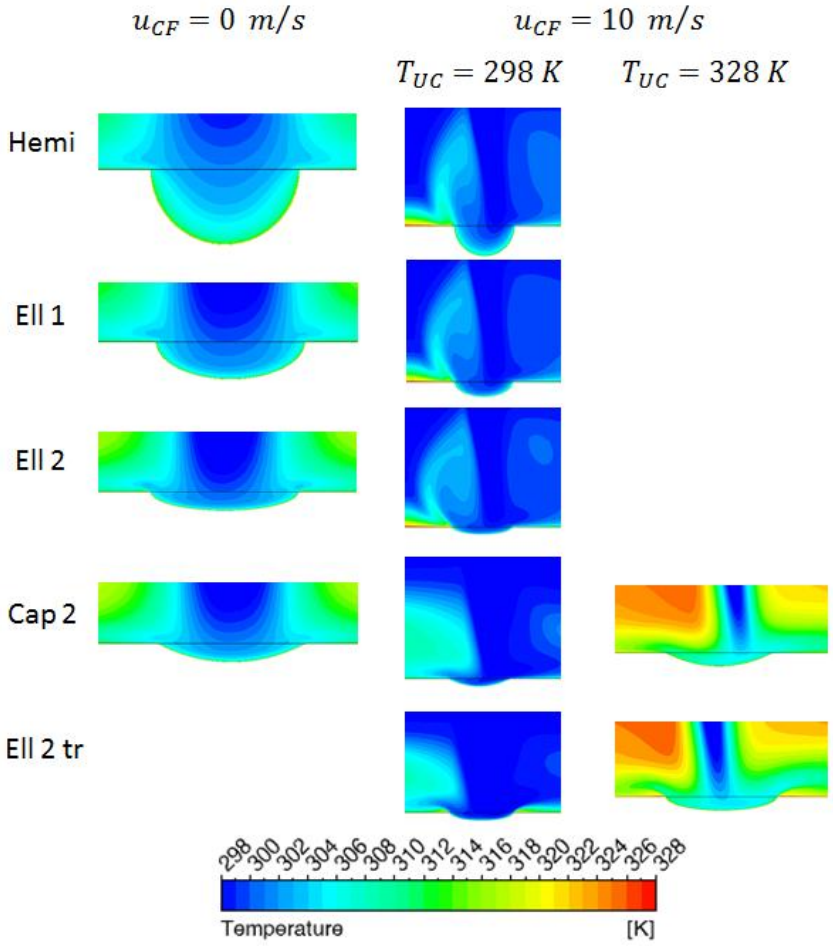

Figure 5.19 - Temperature contours for the dimple patterns.

To conclude, an investigation has been performed on the effect of the spanwise shift of the dimples. This shift has been applied as a fraction z/S_z of the jet spacing $S_z = 10\ mm$. The analyzed cases are $z/S_z = 0.1$ and $z/S_z = 0.5$, as shown in Figure 5.20. Since the latter configuration is quite similar to the flat surface, the results have been compared to the case without roughness with $S_y = 5\ mm$. Cross flow has not been included in these analyses.

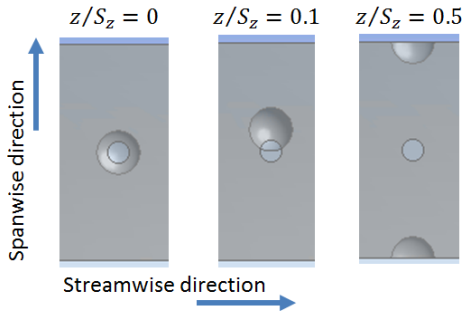

Figure 5.20 - Spanwise shift of the dimple patterns.

The obtained results are shown in Figures 5.21, 5.22 and 5.23, for the configurations *Hemi*, *Ell 1* and *Ell 2*, respectively.

The hemispherical dimple showed no surprises: a small spanwise shift has a negligible effect on the performance. When the dimple is located in the furthest position from the jet, it behaves like a flat surface, although the Nusselt number in the peak region is improved. The reason of this phenomenon is the stabilizing effect exerted by these deep dimples in this location, where the vortices developed between two adjacent jets interact.

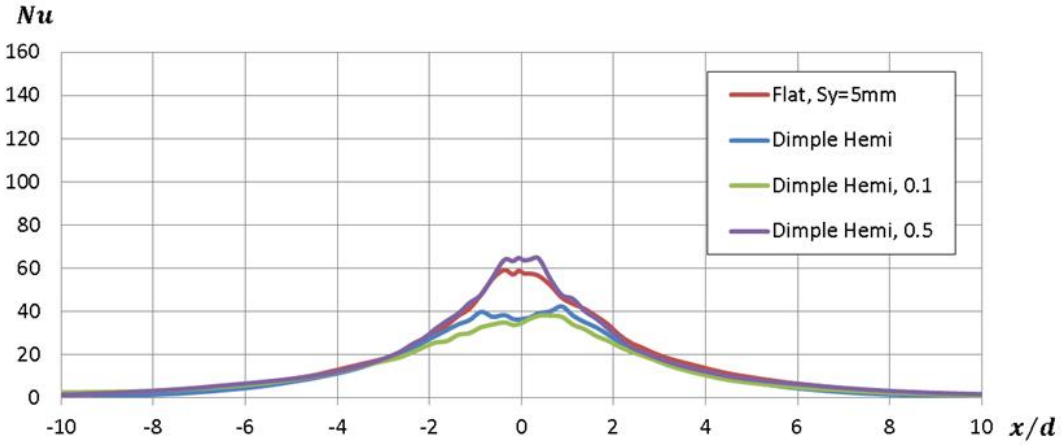

Figure 5.21 - Nusselt number: pattern *Hemi*, spanwise translation, no cross flow.

For shallower dimples, the situation is different, with the heat transfer that worsens as z/S_z increases. This trend is more pronounced for the geometry *Ell 2*, where the variation is significant. This behavior points out a fact already seen before, when the shallow, elliptical dimple has been shifted forward to compensate the cross flow effect. Although the roughening patterns with shallow dimples have a great potentiality to enhance heat transfer, they are very sensitive (much more than other configurations) to the relative position of the impinging jet, which can be significantly influenced, among other parameters, by the cross flow.

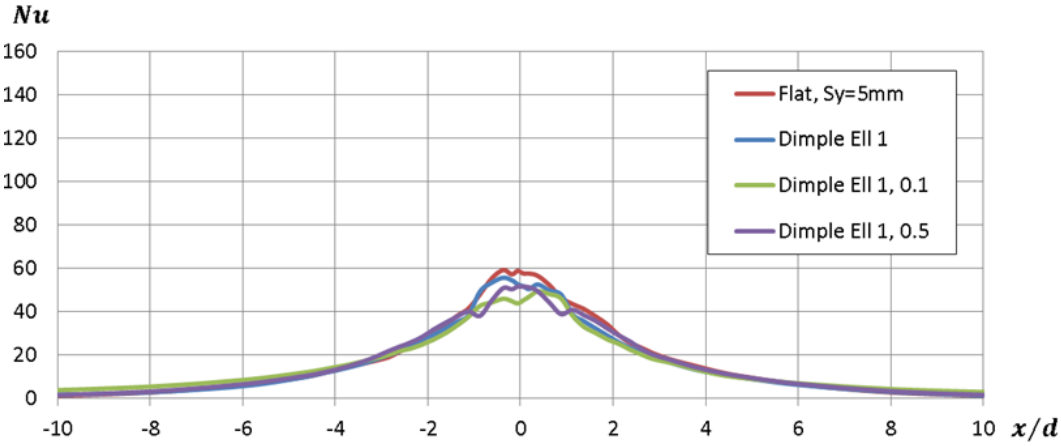

Figure 5.22 - Nusselt number: pattern *Ell 1*, spanwise translation, no cross flow.

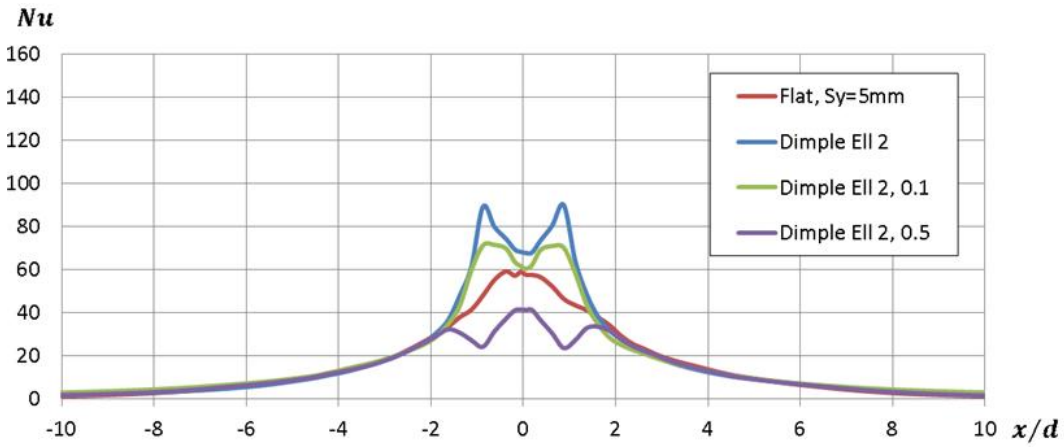

Figure 5.23 - Nusselt number: pattern *Ell 2*, spanwise translation, no cross flow.

A more in-deep look at the velocity contours plotted in Figure 5.24 and referring to the spanwise direction (or the *yz* plane), shows that a small misalignment between jet and dimple ($z/S_z = 0.1$) creates a strongly non-symmetric flow field, which has two effects. To begin with, recirculation regions near the edge of the dimples are visible and they are similar to the ones observed when the jet is under cross flow (see Figure 5.18). Secondly, the non-symmetry results in a disturbance for the subsequent jet of the row and in a slight jet deflection, which leads to reduced heat transfer. However, this contribution is moderate and does not worsen too much the performance.

When $z/S_z = 0.5$, the hemispherical dimple promotes a more stable interaction between two adjacent jets, while for the shallower dimples stronger vortices arise, which are more disturbing for the row of jets.

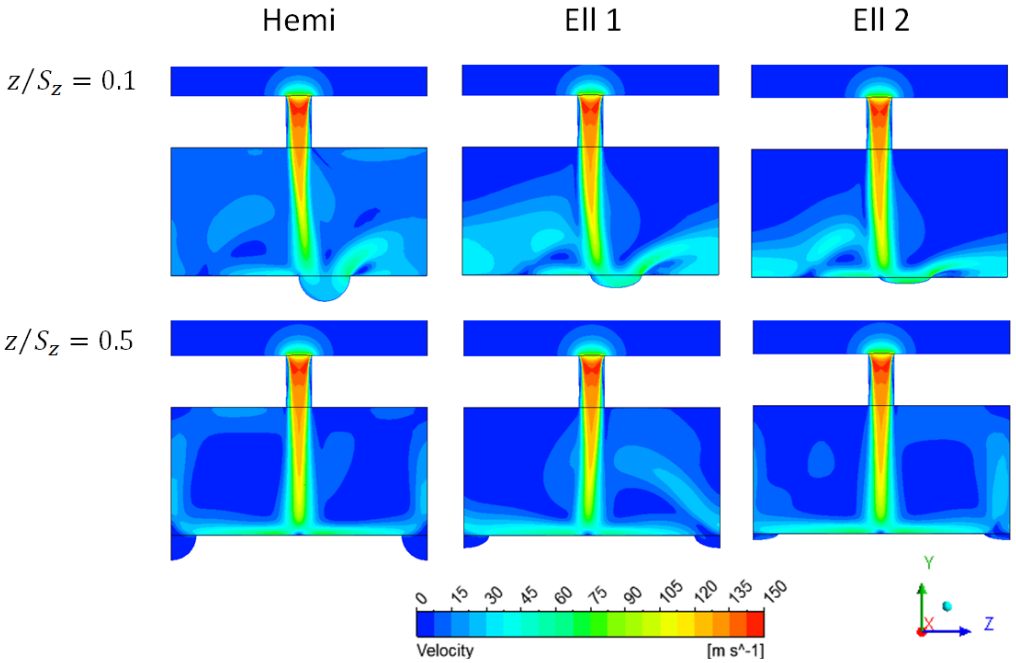

Figure 5.24 - Velocity contours for the dimples under spanwise shift, no cross flow.

5.3.3 Surface with Waved Dimples

After the studies carried out on simple dimples, other roughening patterns have been analyzed. The idea was to create more complex geometries and to investigate their effect on heat transfer. One of these patterns has been called *Waved Dimple*. In addition to the dimple under the impinging jet, five alternating waves have been added, as explained in Figure 5.25. The first two waves have a diameter and a maximum depth (or height) that are half of those of the dimple. For the outer three waves the diameter and the height are a forth of d_D and h_r. Overall, this geometry extends for a radius of 4.5 mm from the point below the impinging jet.

Two patterns have been realized, basing on the dimples *Ell 1* and *Ell 2*, which have been described in the previous subparagraph. With the addition of the waves, the increase in the wetted area becomes significant, as shown in Table 5.12, together with all the other geometrical parameters of the two patterns.

As for the dimples, the effect of the spanwise shift has been also investigated, with an additional run for each pattern at $z/S_z = 0.5$ and no cross flow.

Table 5.12 - Geometrical parameters for the waved dimple patterns.

	$d_D\ [mm]$	$h_r\ [mm]$	$S_{y,eff}\ [mm]$	$\Delta A_{\%}$
Waved Dimple 1 (WD 1)	2	0.5	5.5	12.87
Waved Dimple 2 (WD 2)	2	0.25	5.25	4.40

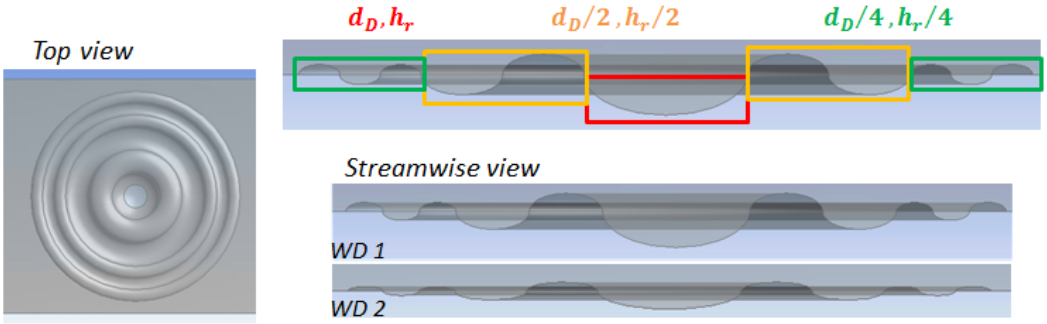

Figure 5.25 - Design of the waved dimple patterns.

A glance at Table 5.13, in which the overall Nusselt numbers are listed, tells that the waved dimples generally perform worse than the flat surface. However, when the patterns are shift at $z/S_z = 0.5$, heat transfer is significantly improved.

Table 5.13 - Overall Nusselt numbers obtained from CFD, flat surface vs waved dimple patterns.

	$u_{CF} = 0\ m/s$	$u_{CF} = 10\ m/s$ $T_{UC} = 298\ K$
Normal $S_y/d = 6$	28.8	44.5
WD 1	18.5	25.0
WD 2	23.2	33.3
WD 1, 0.5	26.7	-
WD 2, 0.5	25.6	-

The graph in Figure 5.26 compares the Nusselt number of the two patterns with the flat surface, in the absence of cross flow. Besides the lower heat transfer,

local peaks can be noticed in correspondence of the waves and are more noticeable for the run with the shorter waves, *WD 2*. This behavior can be explained by using the local velocity contours shown in Figure 5.28. The presence of the waves creates stagnation regions in the wave troughs. Here, it is difficult for the jet boundary layer to penetrate and heat transfer is worsened. This phenomenon is more accentuated for the geometry with deeper waves.

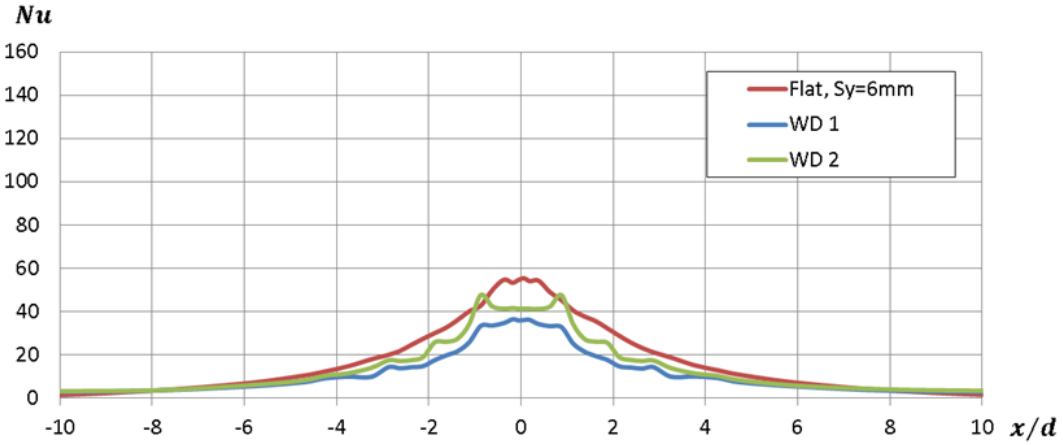

Figure 5.26 - Nusselt number: waved dimple patterns, no cross flow.

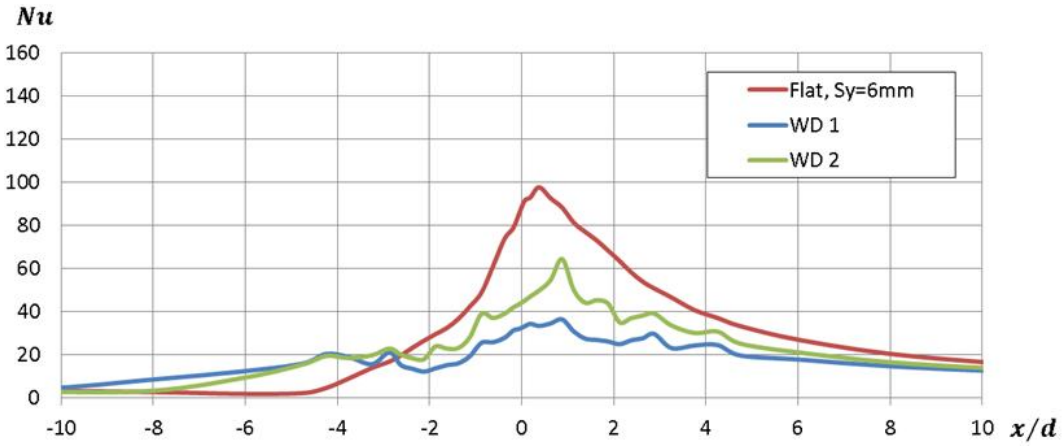

Figure 5.27 - Nusselt number: waved dimple patterns, $u_{CF} = 10\,m/s$, $T_{UC} = 298\,K$.

The local peaks are still observable when the cross flow is introduced (Figure 5.27). The interaction between the latter and the waves significantly worsens the heat transfer. Here, the stagnation regions in the wave troughs prevented not only the jet boundary layer, but also the cross flow, to cool down the target surface.

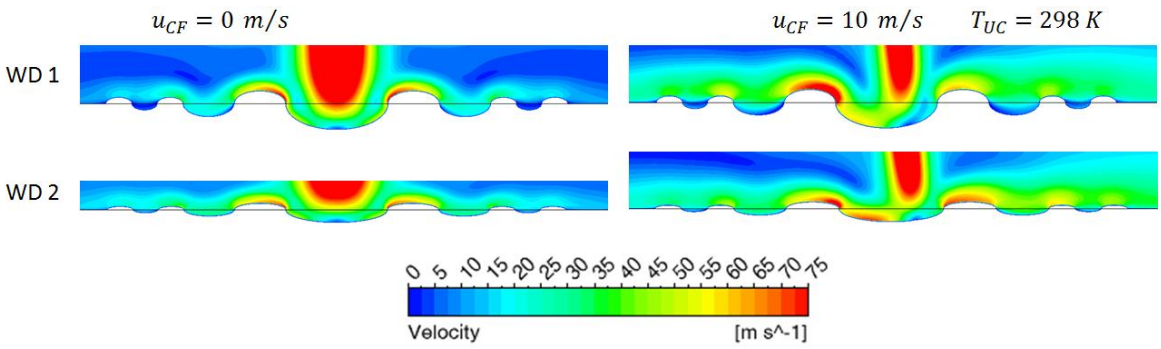

Figure 5.28 - Velocity contours for the waved dimple patterns.

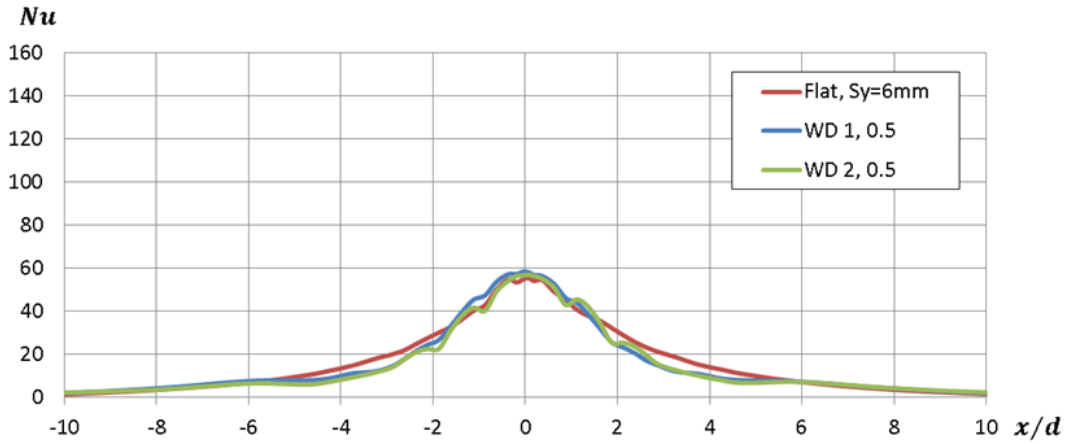

Figure 5.29 - Nusselt number: waved dimple patterns, $z/S_z = 0.5$, no cross flow.

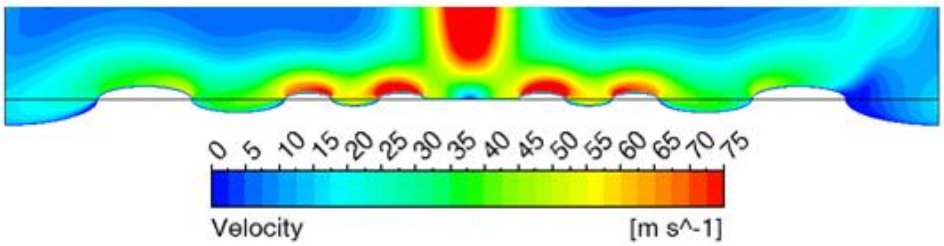

Figure 5.30 - Velocity contour on the spanwise direction for *WD 2*, $z/S_z = 0.5$, no cross flow.

The results that have been obtained under cross flow proved that these patterns are not a valid alternative to the flat surface. However, the effect of the shift in the spanwise direction has been investigated, placing both the patterns at $z/S_z = 0.5$. The Nusselt numbers in the streamwise direction are shown in Figure 5.29. In this configuration, the jet impinges on a flat portion of the target surface and encounters first the three smaller waves (with $d_D/4$ and $h_r/4$). Here, the boundary layer remains attached to the surface and no stagnation regions are recorded, as shown in the velocity contour, along the spanwise direction, in Figure 5.30. For both the geometries, the heat transfer has been significantly improved and the local peaks are still visible. However, the obtained results barely match those already achievable with the flat surface and are not as promising as other roughening patterns.

5.3.4 Surface with Composed Dimples

Another typology of roughening patterns that has been investigated is that one, in which the basic dimple is combined into more complex geometries. To begin with, dimples have been combined in groups of two or four, as shown in Figure 5.31. The structure *DD1* has been obtained with the partial union of two dimples, each one shifted by 0.75 mm from the position under the impinging jet. Then, a twist of 90 degrees has been applied to create pattern *DD2*. The union of these two geometries resulted in *QD1*, from which *QD2* has been obtained with a twist of 45 degrees. The basic dimple that has been utilized to realize these

patterns is *Ell 2*. The increase in wetted area $\Delta A_{\%}$ is 0.62% for the *DD* patterns and 0.84% for the *QD* geometries. Moreover, the maximum extension of these dimples on the target surface is $1.75d$ away from the jet.

Finally, the effect of a spanwise shift $z/S_z = 0.1$ has been analyzed.

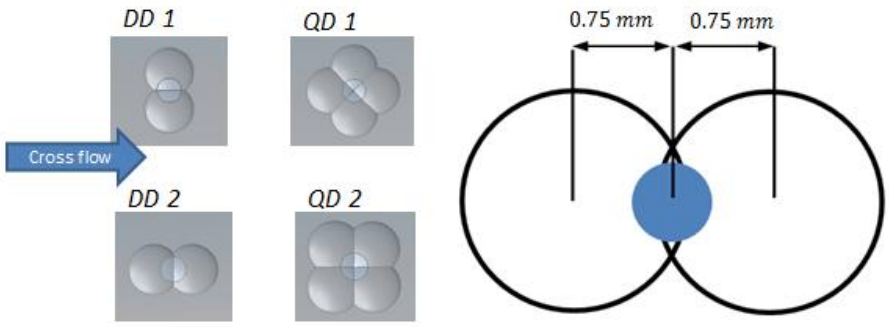

Figure 5.31 - Design of the multiple dimple patterns.

In terms of overall Nusselt number (shown in Table 5.14), all the proposed geometries perform better than the flat surface, without cross flow. For *DD* patterns, the result turned out to depend on the fact that the roughening element was disposed either in the spanwise (*DD1*) or in the streamwise (*DD2*) direction. This behavior can be explained with the presence of the adjacent jets in the spanwise direction, which negatively affect the wall boundary layer developed into the roughening elements (see the velocity contours in Figure 5.32). Moreover, this result can be compared to those shown in Figure 5.23, where a small spanwise shift of *Ell 2* led to a significant decrease in the Nusselt number. This difference can be also noticed between the two *QD* patterns, although it is very small, since they are less sensitive to a directional twist than the *DD* geometries.

When a cross flow at $u_{CF} = 10\,m/s$ and low temperature is introduced, the trends that have been previously described are still observable. In addition, all the configurations performed are worse than the condition without roughness. Even when the streamwise translation of *DD2* and *QD2* was applied, in order to compensate the jet deflection due to the cross flow, the recorded variations were negligible.

Table 5.14 - Overall Nusselt numbers obtained from CFD, flat surface vs multiple dimple patterns.

	$u_{CF} = 0\,m/s$	$u_{CF} = 10\,m/s$ $T_{UC} = 298\,K$	$u_{CF} = 10\,m/s$ $T_{UC} = 328\,K$
Normal $S_y/d = 6$	28.8	44.5	15.4
Ell 2 (basic dimple)	35.1	36.4	-
DD 1	30.9	35.7	-
DD 2	34.4	40.2	-
QD 1	31.6	38.1	-
QD 2	32.1	39.6	-
DD 2 tr	-	38.8	20.2
QD 2 tr	-	38.0	17.5

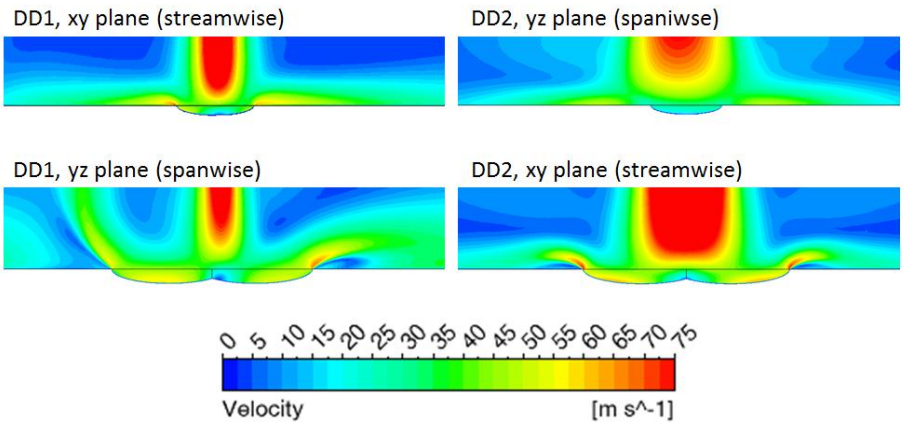

Figure 5.32 - Velocity contours for the *DD* patterns.

Finally, the most promising solutions, i.e. *DD2* and *QD2* with the streamwise shift of 0.4 mm, have been simulated into a cross flow at high temperature. Both the configurations performed significantly better than the flat surface: the *DD2* geometry exhibited an increase in the overall Nusselt number of +31.2%, while a moderate +13.6% was recorded for the *QD2* pattern.

The streamwise Nusselt numbers recorded for the proposed patterns in the absence of cross flow are shown in Figure 5.33, while the local Nusselt numbers near the impingement point are plot in Figure 5.34. The trend of the *DD1* pattern resembles that of *Ell 2* (see Figure 5.14), with two local peaks near the edge of the dimple. The region near the stagnation point shows a minimum. This is related to the interaction between the roughening element and the row of jets, as previously discussed.

Compared to *DD1*, *t*he *QD1* pattern exhibits a similar trend, even if the peaks in the Nusselt number are lower and the heat transfer near the impingement is higher. This result has been achieved thanks to the addition of the two dimples extending in the streamwise direction. Indeed, this pattern allows obtaining a more uniform heat transfer within the range $x/d \leq \pm 2$.

The two twisted patterns, *DD2* and *QD2*, prove to be capable of a better heat transfer in the entire region near the stagnation point, when compared to the flat surface. The reason for this behaviour can be explained with the direction of the dimples in relation to the row of adjacent jets. Both the *DD1* and *QD1* patterns extend in the spanwise direction. When the jet impinges on the target surface, the wall boundary layer is accelerated within the roughening element and exits from its edge. Here, this flow interacts with the downwash of the adjacent jet and detaches from the wall, resulting in worsening of heat transfer. On the contrary, for the twisted patterns, the jet boundary layer is expelled from the dimples in other directions than the spanwise one, resulting in a higher Nusselt number. The difference between *QD1* and *QD2* is less remarked because the use of four dimples, instead of two, allows a better split of the impinging jet.

This explanation is supported by the velocity contours shown in Figure 5.32 and can be noticed in the Nusselt plot in Figure 5.34, in the blue parts of the *DD1* and *QD1* dimples.

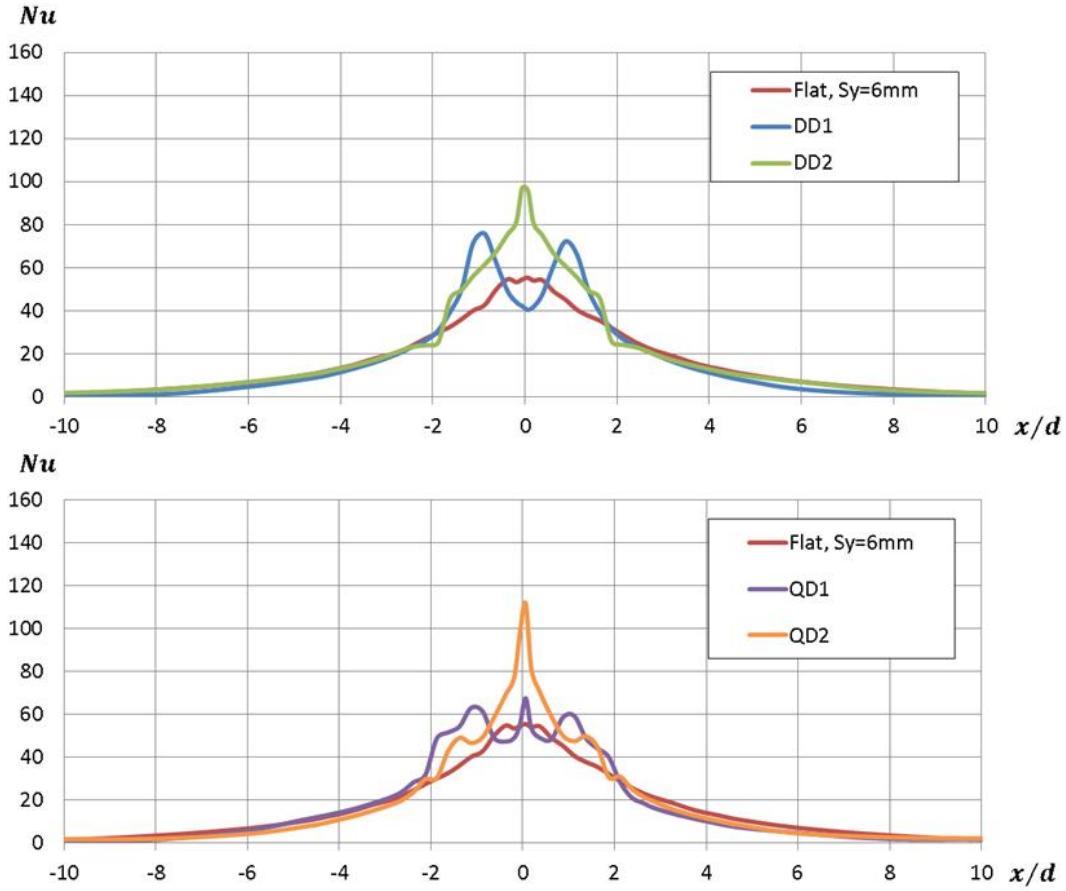

Figure 5.33 - Nusselt number: *DD* (top) and *QD* (bottom) patterns, no cross flow.

The same geometries have been investigated under cross flow at low temperature (Figure 5.35). Here, the observed behaviour is quite similar to that seen for the basic dimples. Due to the curvature of the dimple and to the incoming cross flow, the jet boundary layer detaches from the target surface, as shown in the velocity contours in Figure 5.37, middle column. Consequently, the Nusselt number suddenly drops near the edge of the dimple exposed to the cross flow.

Accordingly to the results obtained in the absence of cross flow, multiple peaks are still present for the untwisted patterns (two for *DD1* and three for *QD1*), even if the highest values are shifted downstream, due to the presence of the cross flow.

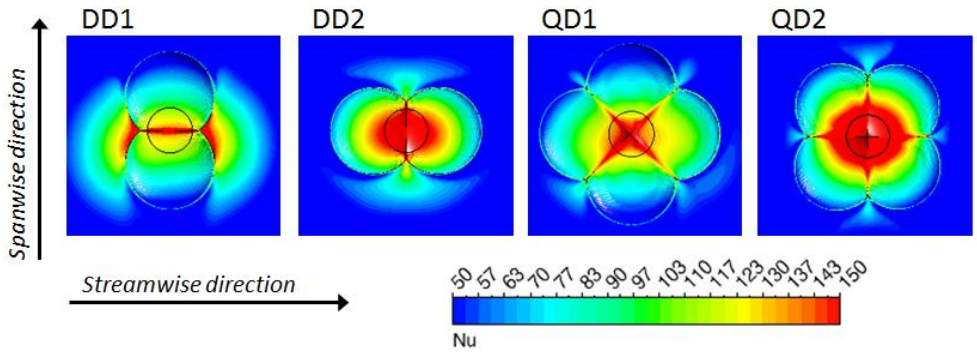

Figure 5.34 - Nusselt number: local plots near the impingement point, no cross flow.

Once again, the twisted patterns exhibit a more regular curve. In comparison with the flat surface, the heat transfer is enhanced in the stagnation region, while the Nusselt number is lower in the region outside the dimple.

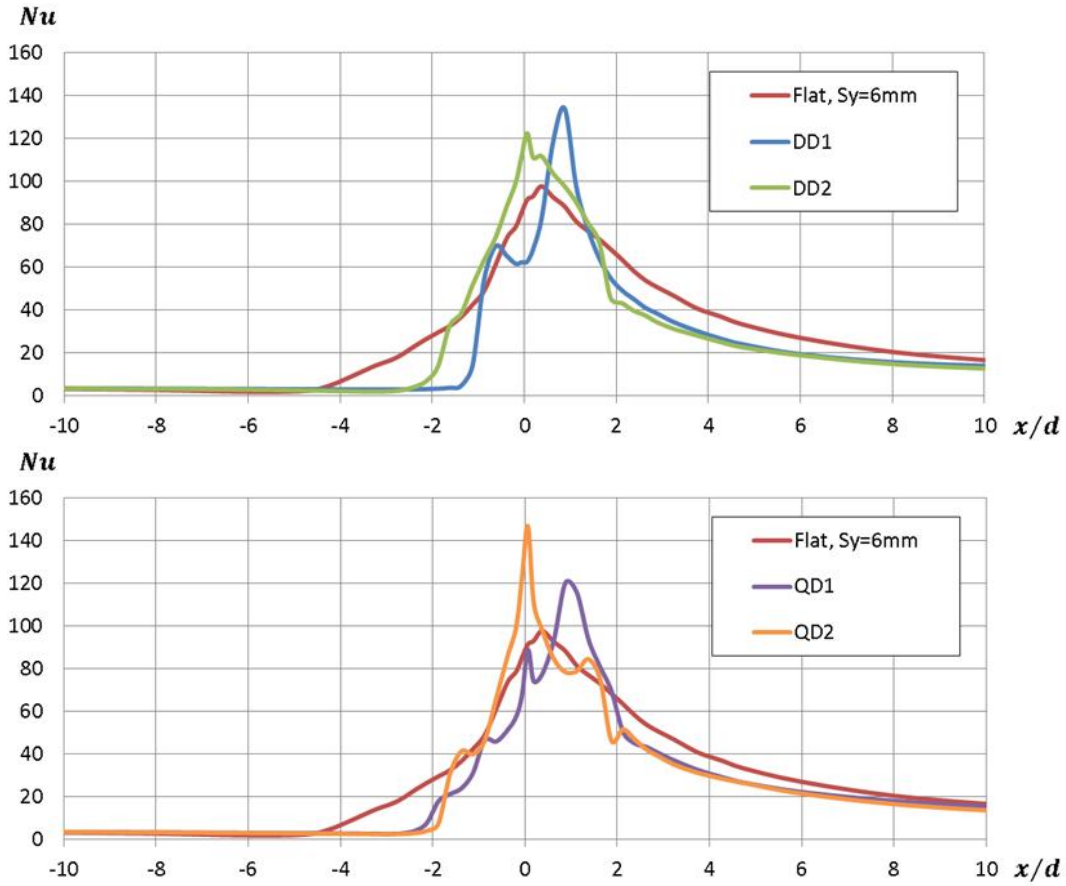

Figure 5.35 - Nusselt number: *DD* (top) and *QD* (bottom) patterns, $u_{CF} = 10\,m/s, T_{UC} = 298\,K$.

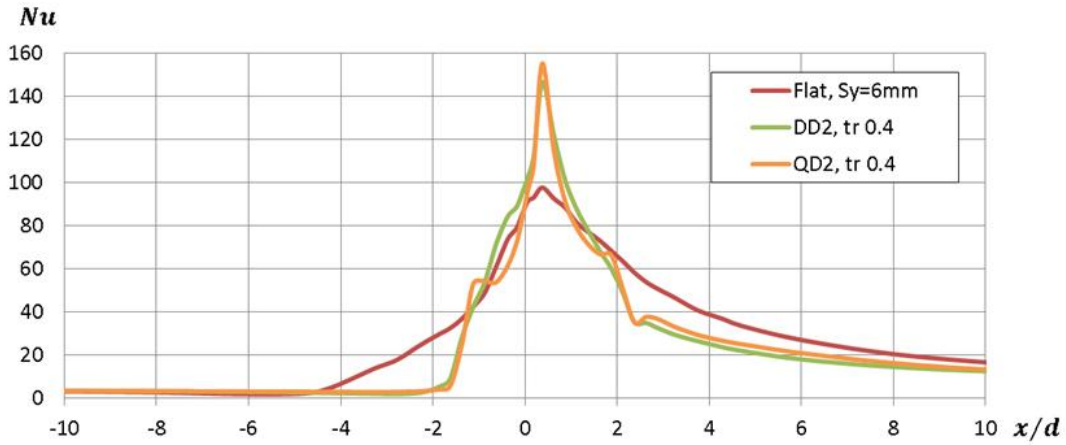

Figure 5.36 - Nusselt number: effect of the streamwise translation on *DD2* and *QD2*, $u_{CF} = 10\,m/s, T_{UC} = 298\,K$.

With the purpose to further improve the recorded performance, the *DD2* and *QD2* patterns have been shifted 0.4 mm in the streamwise direction, in order to compensate the deflection due to the cross flow. This expedient has been already applied to the elliptical dimple *Ell 2*, obtaining even better results when the

configuration has been put under cross flow (see Figures 5.16 and 5.17). However, this time the axial shift had no significant effect. Indeed, the velocity contours shown in Figure 5.37 are very similar (compare the column on the right with the central one). The same applies to the Nusselt number (see Figure 5.36), even if the maximum value for *DD2* is higher. Morever, the maximum value shifts downstream for both the patterns, as a consequence of the geometrical shift.

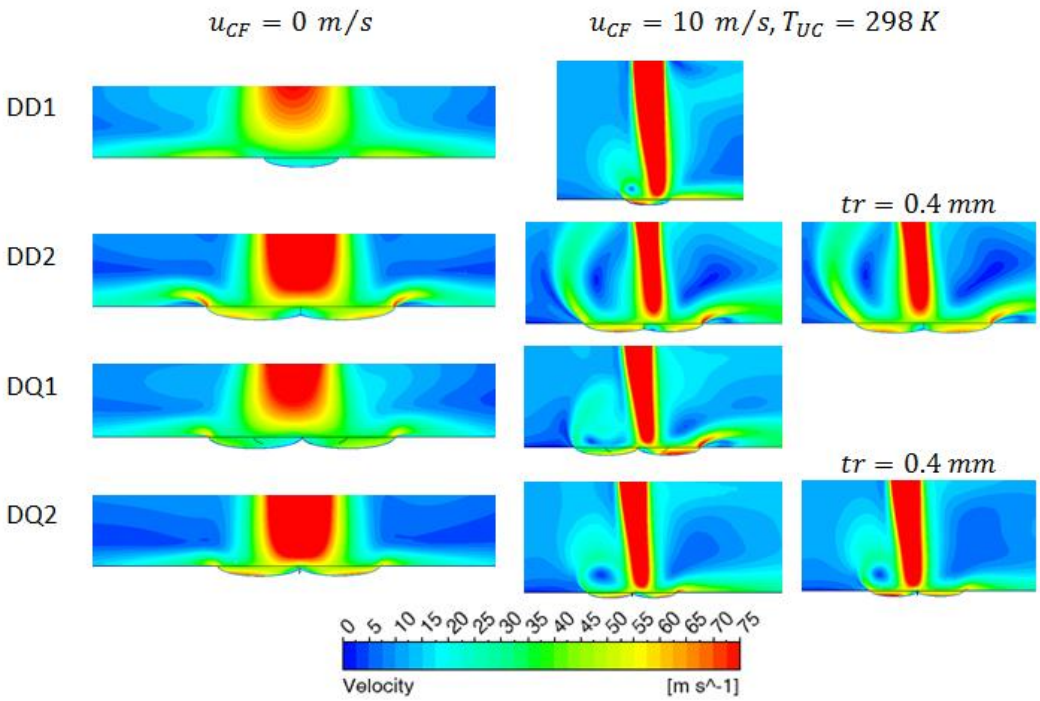

Figure 5.37 - Velocity contours for the multiple dimple patterns.

These two configurations have also been analyzed under cross flow at $T_{UC} = 328\ K$ and compared to the flat surface and to *Ell 2 tr* (all the curves are shown in Figure 5.38). All the patterns exhibit enhanced heat transfer near the stagnation region. While the Nusselt number obtained with the basic dimple is quite uniform in this region, the composed dimples show a peak near the impingement point. However, the *QD2* pattern has a smaller area than the basic configuration. On the contrary, the *DD2* pattern seems more promising.

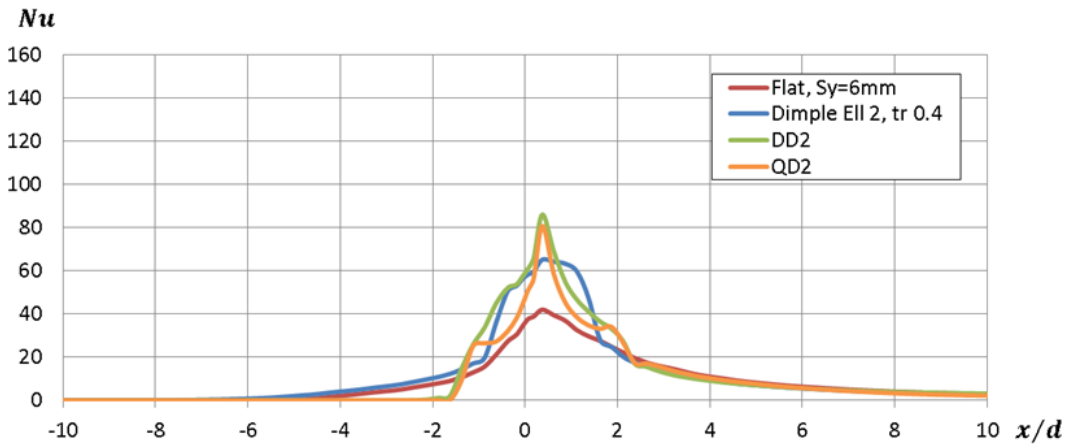

Figure 5.38 - Nusselt number: multiple dimple patterns, $u_{CF} = 10\,m/s$, $T_{UC} = 328\ K$.

Finally, the effect of the spanwise shift on the Nusselt number has been investigated. The four patterns have been simulated at $z/S_z = 0.1$, in the absence of cross flow. The overall Nusselt numbers are listed in Table 5.15. Compared to the basic dimple *Ell 2*, the composed patterns exhibit the advantage to be more stable, since the Nusselt number slightly changes. Indeed, the curves are plotted in Figure 5.39 are very similar to those shown in Figure 5.33 at $z/S_z = 0$.

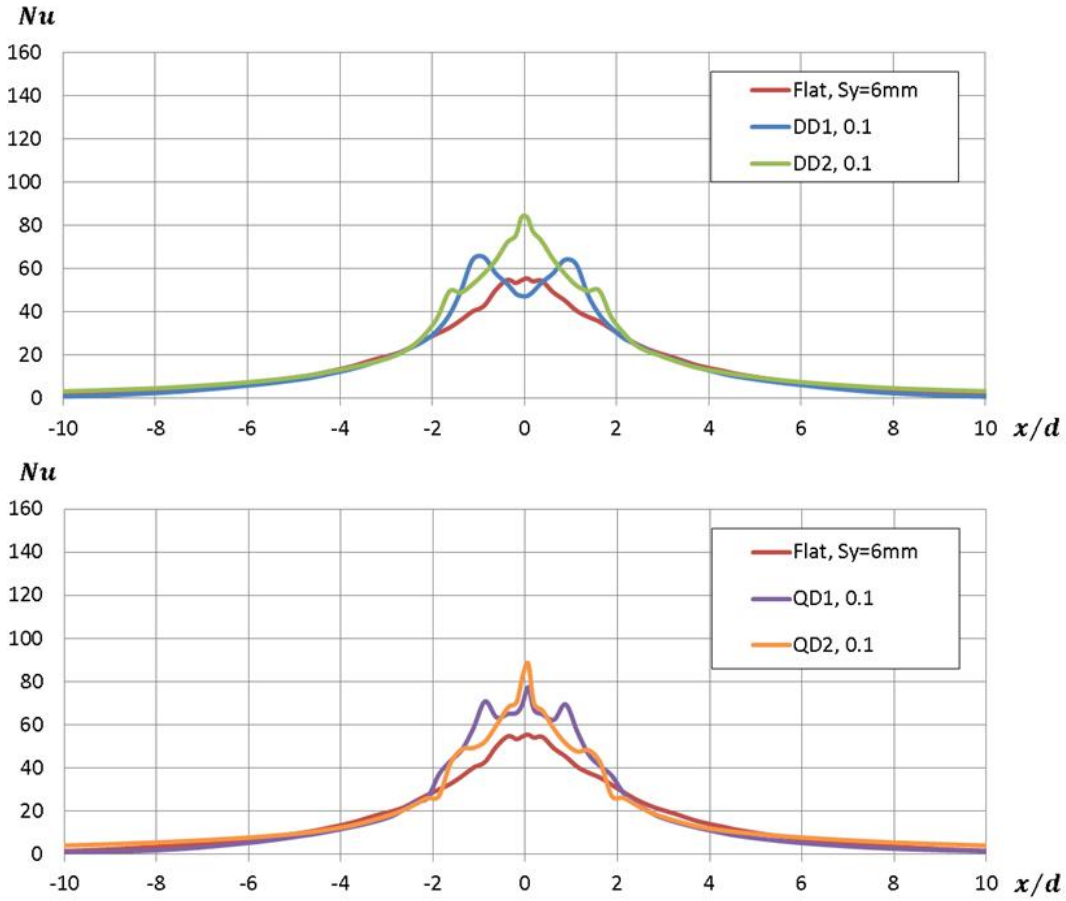

Figure 5.39 - Nusselt number: *DD* (top) and *QD* (bottom) patterns, no cross flow, $z/S_z = 0.1$.

Table 5.15 - Overall Nusselt numbers, flat surface vs multiple dimple patterns, effect of the spanwise shift, no cross flow.

	$z/S_z = 0$	$z/S_z = 0.1$
Normal $S_y/d = 6$	28.8	
Ell 2 (basic dimple)	35.1	32.8
DD 1	30.9	31.2
DD 2	34.4	34.6
QD 1	31.6	32.6
QD 2	32.1	31.8

The velocity contours plotted in Figure 5.40 refer to the spanwise direction. As observed for the dimples in subparagraph 5.4.2, the spanwise shift creates a non-symmetric flow field, which induces a disturbance in the row of jets. However, these patterns are more stable than the basic dimples. In particular, the projections of the patterns *DD1*, and *QD1* show that one of the two dimples is

aligned to the jet. It can be noticed that the boundary layer behaves in different ways, according to the length of the projection of the dimple. For the pattern *DD1*, which exhibits a smaller projection, the boundary layer creates a recirculation region at the edge of the second dimple. Then, it separates due to the flow coming from the adjacent jet. The pattern *DD2* has bigger dimples in projection, and the separation can be already observed at the edge of the second dimple. Although the spanwise projection of pattern *QD2* is not aligned to the impinging jet, a similar mechanism to the one previously described can be noticed. In this case, the boundary layer forms no recirculation regions and separation occurs closer to the subsequent jet. The flow field seen for the pattern *QD2* is very similar to the contour plotted for the pattern *DD2*. In the latter, the spanwise projection consists of a small dimple, with the impingement occurring outside the dimple, near its edge. From these contours, it clearly appears how a small change in the dimple position could affect the development of the boundary layer and, consequently, the heat transfer on the impingement surface.

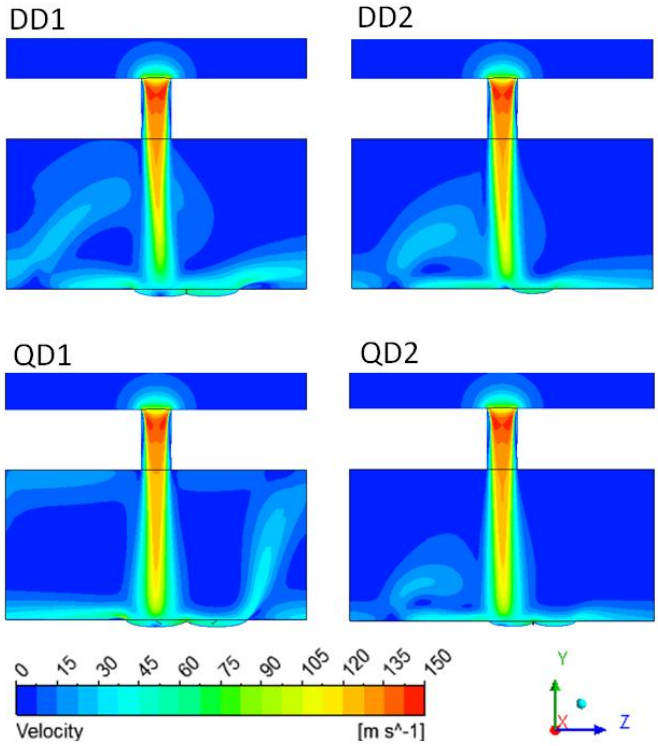

Figure 5.40 - Velocity contours for the composed dimples at $z/S_z = 0.1$, no cross flow.

5.3.5 Surface with Composed Dimples and Bumps

The pattern made by the union of two *Ell 2* dimples and placed in the streamwise direction, named *DD2*, appears to be promising in the perspective to enhance the heat transfer on the casing of the LPT. However, the separation of the wall boundary layer occurring under cross flow limits the enhancement to the region within the dimple. The configurations that are investigated in this subparagraph are a possible solution to overcome this limit.

The investigated patterns are obtained by combining the geometry *DD2* with a bump placed at the edge of the dimple, as shown in Figure 5.41. The diameter of the bump is the same of the basic dimple, $d_D = 2\,mm$. The extension of this geometry, in terms of maximum distance from the impinging jet, is $3.75d$ in the streamwise direction and $3d$ in the spanwise direction. The cross-section of the bump can be either elliptical (as for the dimple) or spherical-cap. Two values of the height h_B have been investigated: when $h_B = h_r = 0.25\,mm$, the bump is indicated as *BD2* or *BCap2* (depending on its cross-section), while the height $h_B = 0.125\,mm$ is named *BD3* or *BCap3*. To summarize, four combinations have been analyzed in the absence of cross flow and with cross flow at low and high temperature.

In addition, two other patterns, the dimple composed by two *Cap 2* and combined with *BCap2* and *BCap3*, have been investigated in the same conditions. These geometries have been included in the present analysis because the simple spherical-cap pattern was not affected by the separation of the boundary layer, which has been recorded for all the other dimple patterns under cross flow (see the velocity contours in Figure 5.18). The increase in wetted area is shown in Table 5.16, together with the overall Nusselt numbers.

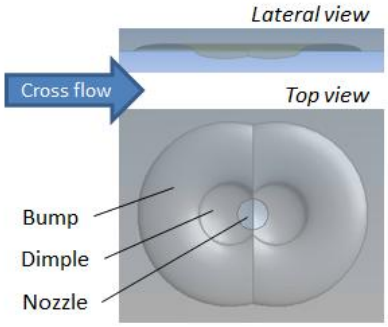

Figure 5.41 - Design of a generic composed dimple with bump.

By looking at the results obtained in absence of cross flow, it turns out that all the proposed patterns perform better than the flat surface. However, the most interesting results are the configurations DD2 combined with the spherical-cap bumps *BCap2* and *BCap3*, in which heat transfer is enhanced by 23.3% and 27.8%, respectively. These improvements are also higher than the values recorded for the *DD2* or for the *Ell 2* dimple (the latter with an increase of 21.9% and the former with a slightly lower 19.4%, in terms of overall Nusselt number).

When the cross flow at low temperature is introduced, all the proposed geometries exhibit higher Nusselt numbers than the basic dimple and the *DD 2* pattern. The only exception is the *DD2+BD2* pattern, since it has a smaller Nusselt number than the *DD 2* geometry. This means that, in general, the addition of the bump delays the separation of the boundary layer under the action of the external cross flow.

Under the cross flow at high temperature, the worst result is an improvement of 12.3% in the overall Nusselt number (*DCap2+BCap2* pattern), compared with the flat surface. The best results have been obtained by combining the *DD 2* to the

spherical-cap bumps, with the remarkable increase of 53.2% and 44.8% for the higher bump and for the shorter one, respectively.

Table 5.16 - Overall Nusselt numbers obtained from CFD, flat surface and basic dimple vs patterns combining dimples and bumps. In addition, the increase in wetted area is shown. (* Nu for *tr* runs).

	$u_{CF} = 0\ m/s$	$u_{CF} = 10\ m/s$ $T_{UC} = 298\ K$	$u_{CF} = 10\ m/s$ $T_{UC} = 328\ K$	$\Delta A_{\%}$
Normal $S_y/d = 6$	28.8	44.5	15.4	-
Ell 2	35.1	36.4	*21.1	0.38
DD 2	34.4	40.2	*20.2	0.62
DD2+BD2	30.4	39.3	18.4	2.72
DD2+BD3	31.3	40.9	19.1	1.29
DD2+BCap2	35.5	49.5	23.6	1.82
DD2+BCap3	36.8	41.9	22.3	0.92
DCap2+BCap2	29.3	41.2	17.3	1.51
DCap2+BCap3	30.1	42.8	17.4	0.62

The curves plotted in Figure 5.42 refer to the simulations carried out without cross flow. More details, in terms of velocity contours, are shown in Figure 5.44, in the left column. In comparison with the flat surface, all those patterns, which are based on the *DD 2* dimples, exhibit a higher Nusselt number in the range $x/d \leq \pm 2$ and a similar performance outside this range. However, compared to the basic *DD 2* geometry (shown in Figure 5.33), the addition of elliptical bumps worsened the heat transfer.

The reason of this different behavior stays in the curvature at the junction between the dimple and the bump. Indeed, this geometrical feature interacts with the boundary layer, promoting regions with lower static pressure, as shown in the Figure 5.43. Considering the elliptical bump, the curvature at the junction increases if the shorter bump is used instead of the higher one. At the same time, the region at lower pressure decreases and the Nusselt number is higher.

For the spherical-cap bump, the use of the shorter bump imposes, once again, a steeper deflection to the boundary layer than the one recorded with the higher bump. However, unlike for the elliptical bumps, the region at low static pressure is larger with the shorter bump. This behavior is due to the fact that, considering two bumps with the same height, the spherical-cap shape exhibits a lower curvature than the elliptical one. Moreover, when the height is reduced, the former approaches to the geometry of the flat surface. Consequently, a very short *Cap* dimple, in combination with the *DD 2* dimple, will eventually behave as if the bump was not present. This consideration does not apply for the results without cross flow, but it can be verified in the case *DD 2+BCap 3* at $u_{CF} = 10\ m/s$, where the boundary layer eventually separates (see the velocity contour in Figure 5.44, column on the right), similarly to case with the basic *DD 2*.

The combination of spherical-cap dimples with bumps of the same shape leads to no significant effect on heat transfer, since the recorded Nusselt numbers are very similar to those of the flat surface over the entire analyzed range, except

for a slight increase near the stagnation region. The reason is the gentle slope of the roughening elements, which do not act on the boundary layer with multiple accelerations or decelerations, unlike for the *DD 2*-based patterns. This explanation can be confirmed by the pressure contours shown in Figure 5.43.

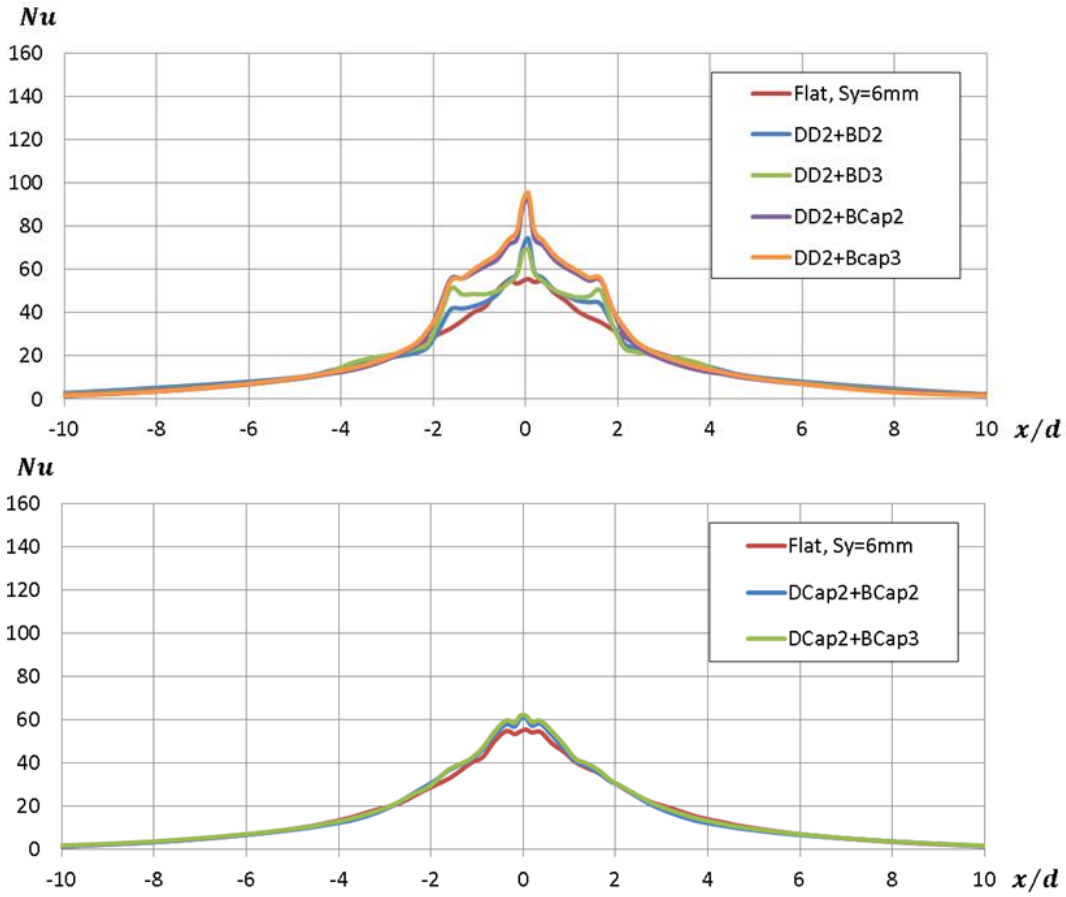

Figure 5.42 - Nusselt number: *DD 2* (top) and *DCap 2* (bottom) patterns, combined with bumps, no cross flow.

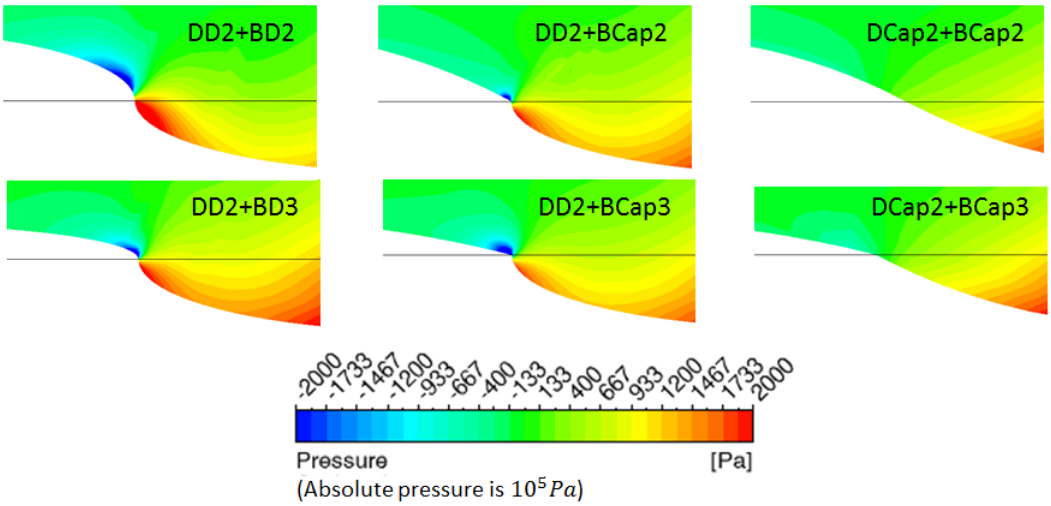

Figure 5.43 - Static pressure at the junction between dimple and bump, no cross flow.

However, the real improvement, which is expected by simulating these configurations, is a better response under cross flow. In particular, the basic *DD 2*

(shown in Figure 5.35), as well as the other composed dimples, exhibited a sudden decrease in the Nusselt number in the range $x/d < -2$, unlike the more gradual decrease obtained when the jet impinged on the flat surface. This phenomenon is related to the sudden detachment of the boundary layer from the edge of the basic composed dimples.

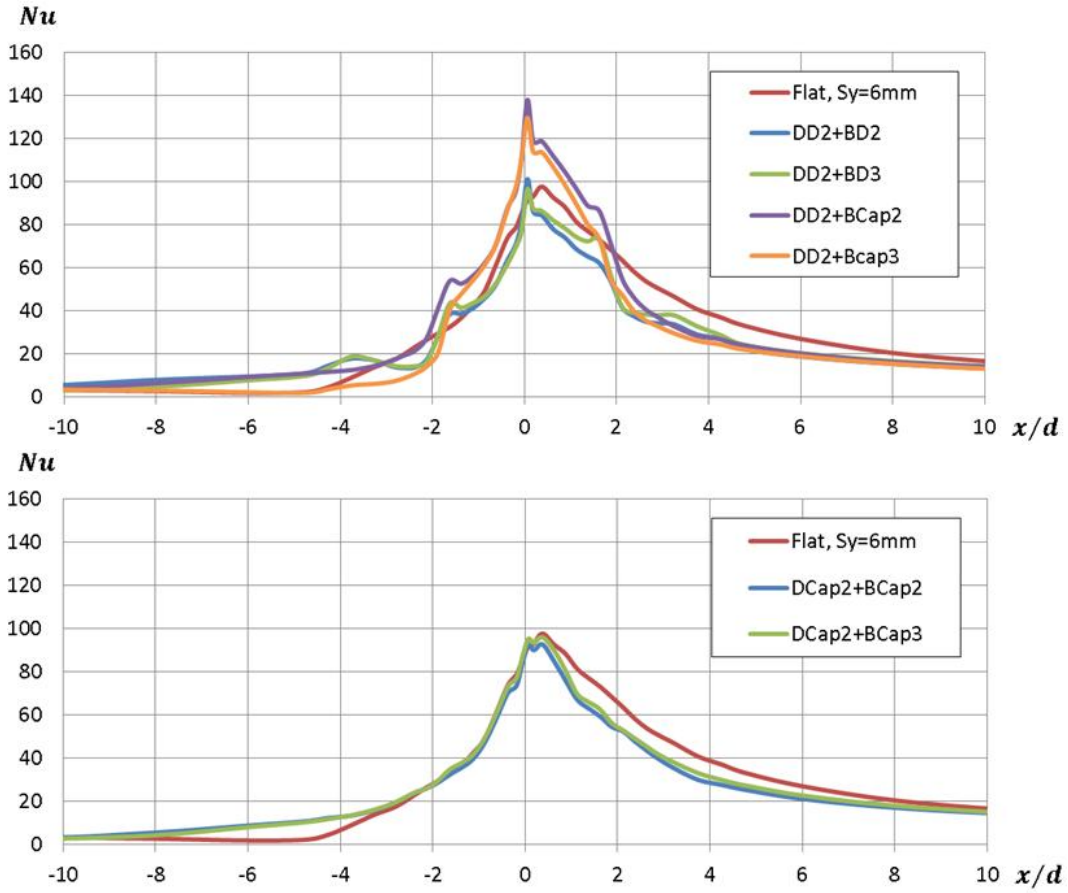

Figure 5.44 - Nusselt number: *DD 2* (top) and *DCap 2* (bottom) patterns, combined with bumps, $u_{CF} = 10\,m/s$, $T_{UC} = 298\,K$.

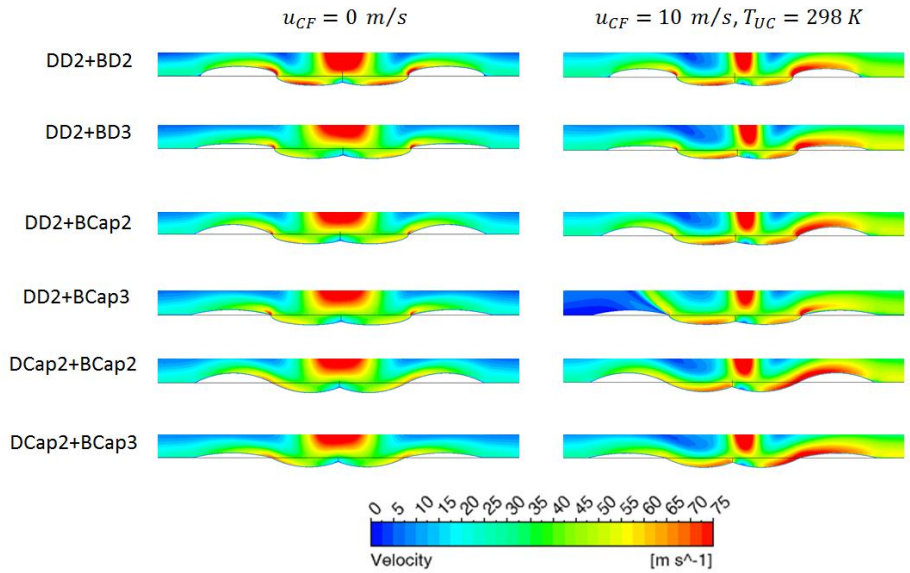

Figure 5.45 - Velocity contours for the dimples combined with bumps.

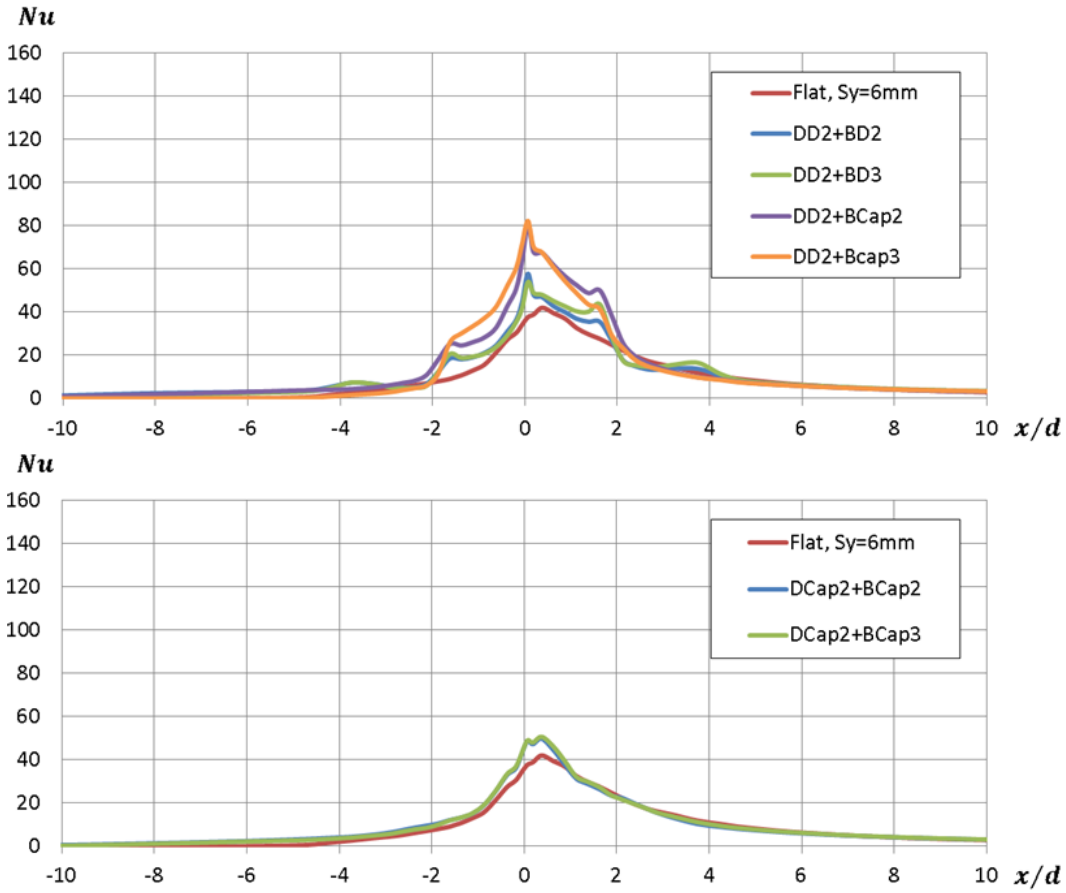

Figure 5.46 - Nusselt number: *DD 2* (top) and *DCap 2* (bottom) patterns, combined with bumps, $u_{CF} = 10\,m/s$, $T_{UC} = 328\,K$.

On the contrary, the addition of the bumps eliminated or at least mitigated this side effect, as plotted in Figure 5.44. In the graph where the *DD 2*-based patterns are shown, it can be noticed that all the curves have shapes similar to the basic *DD 2* (see Figure 5.46, top). Among the several proposed solutions, the pattern *DD 2+Bcap2* is the best one, with enhanced heat transfer in the entire range $x/d \leq \pm 2$. Remarkable results are also obtained for the same typology of pattern with the shorter bump, *DD 2+Bcap3*, even if the boundary layer separated at the edge of the dimple, for the reason previously explained. The patterns with spherical-cap dimples still behave similarly to the flat surface.

When the jet is emitted under cross flow at high temperature (see Figure 5.46), all the proposed patterns exhibit enhanced heat transfer in the range $x/d \leq \pm 2$. The conclusions previously discussed still apply.

5.4 Overall Comparison

The extended CFD investigations carried out in the previous paragraph pointed out several interesting solutions that allow enhancing the heat transfer on the casing of a LPT, which is cooled down by means of jet impingement. In Figure 5.47, all the obtained results are compared in terms of overall Nusselt number, calculated in the range $x/d \leq \pm 5$.

As previously seen, the configurations *DD2+BCap2* and *DD2+BCap3* proved to be the most promising in terms of heat transfer enhancement. However, it must be considered that these patterns have to be manufactured as additional material on the casing of the LPT, which is made in Ti-Al alloys. In addition, the ACC of the LPT utilizes several thousand of impinging jet. Consequently, it is important to provide an evaluation about the increase in terms of weight.

The volumes of the two roughening elements have been calculated on the CAD model and are listed in Table 5.17. As already seen in paragraph 5.2, the CFD model is not axisymmetric, i.e. the circumferential curvature of the casing is neglected. However, this assumption does not introduce a significant error, since the casing is large, while the roughening elements are very small. The weight is calculated assuming the density of titanium (4.5 g/cm^3) as a reasonable guess.

The increase in weight introduced by the two patterns is of the order of sixty grams for every 1000 nozzles, while the heat transfer can be enhanced up to 53.2% and 44.8%, for *DD2+BCap2* and *DD2+BCap3* respectively.

Despite several configurations appear to be promising solutions in terms of heat transfer enhancement with low overall weight increase, there are some observations to be made about their practical application.

The first one concerns the realization of the roughening pattern by using additive manufacturing techniques. Typical values of surface roughness, which are obtained by means of laser beam melting, are in the range of 25-40 μm [71]. In particular, the energy density utilized in the laser process is a key factor in determining the surface roughness of the finished part. In order to obtain the smallest values of roughness, energy densities below 30 J/mm^2 should be applied during the process. However, the energy density also affects the sub-surface porosity, with the latter increasing as the former is higher (typically, energy densities above 40 J/mm^2 allow obtaining relative material densities above 99.7%). In general, a good compromise, between low surface roughness and low porosity, can be obtained by applying energy densities slightly above 30 J/mm^2[71].

Although additional treatments [72] can be applied to remove the residual powder after the manufacturing, in order to reduce the surface roughness, the presence of this random roughness may interfere with the formation of the wall jet. As found in the literature, the presence of random roughness on a flat surface enhances the heat transfer, compared to the smooth surface [46]. However, in this case the roughness interacts with surfaces that are not flat.

Moreover, the realization of dimples may be complex to be realized with the additive manufacturing technique, especially for the smaller dimples, since it is required to obtain a certain curvature within a very small space.

The second observation concerns the position of the roughening element in relation to the impinging jet. Generally, the best condition occurs when the dimple is centered under the nozzle, but a small axial displacement could be applied to compensate the jet deflection due to the cross flow. Since the values of u_{cf} considered in the present study are moderate, this correction is, generally, not

required. One exception is the configuration *Ell 2 tr*, where the downstream displacement has been applied, resulting in enhanced heat transfer. In particular, the axial displacement influenced the separation of the boundary layer at the leading edge of the dimple, i.e. the region where the cross flow and the wall jet are going in opposite directions. The same axial displacement has been applied to the composed dimples *DD2 tr* and *QD2 tr*, to investigate its effect on these configurations. In this case, the correction resulted into a slight worsening of the Nusselt number. Overall, it turned out that the axial displacement affects the performance of the roughening elements. This aspect deserves a more in-depth analysis, in order to identify a trend that allows predicting this behavior. Indeed, the axial displacement not only depends on the jet deflection due to the cross flow, but could also occur as a consequence of thermal expansion under operating conditions. Moreover, a further contribution is due to the installation of the ACC pipes around the LPT casing. In order to obtain a good alignment between the dimple and the nozzle, this installation should be precise.

This last consideration also applies to the nozzle-dimple alignment in the spanwise direction. This aspect has been analyzed in chapter 5, when the several roughening elements have been simulated including a spanwise shift in the periodicity range ($0 \leq z/S_z \leq 0.5$), without cross flow. Generally, higher misalignment in the spanwise direction, i.e. higher values of z/S_z, led to worse heat transfer characteristics. This behavior has been observed especially for the simple dimples. Considering as example the geometry *Ell 2*, even under just a millimeter of spanwise shift ($z/S_z = 0.1$), the overall Nusselt number dropped and the recorded performance was similar to the one observed for the flat surface. For the same element placed at $z/S_z = 0.5$, the overall heat transfer was reduced of about 20%, compared to the flat surface.

On the contrary, the more complex geometries, which have been discussed in subparagraph 5.3.4, exhibited a more robust behavior under a small shift, $z/S_z = 0.1$, with negligible variations in the overall Nusselt number. For the condition $z/S_z = 0.5$, the recorded behavior was the same of *Ell* 2.

Among all the analyzed roughening elements, the hemispherical dimple and the waved dimples showed an opposite trend, with increasing Nusselt numbers for larger spanwise shifts. However, the obtained results were similar to the ones recorded for the flat surface at best.

Moreover, all the simulations have been carried out with a fixed value of d_D/S_z . In other words, the effect related to larger dimples or to more compact jet arrays has not been investigated. These two effects could indeed reduce the negative effect of the spanwise shift.

Table 5.17 - Weight evaluation for the two best patterns.

	Volume (element) $[mm^3]$	Weight (1000 nozzles) $[g]$
DD2+BCap2	14.704	66.2
DD2+BCap3	13.176	59.3

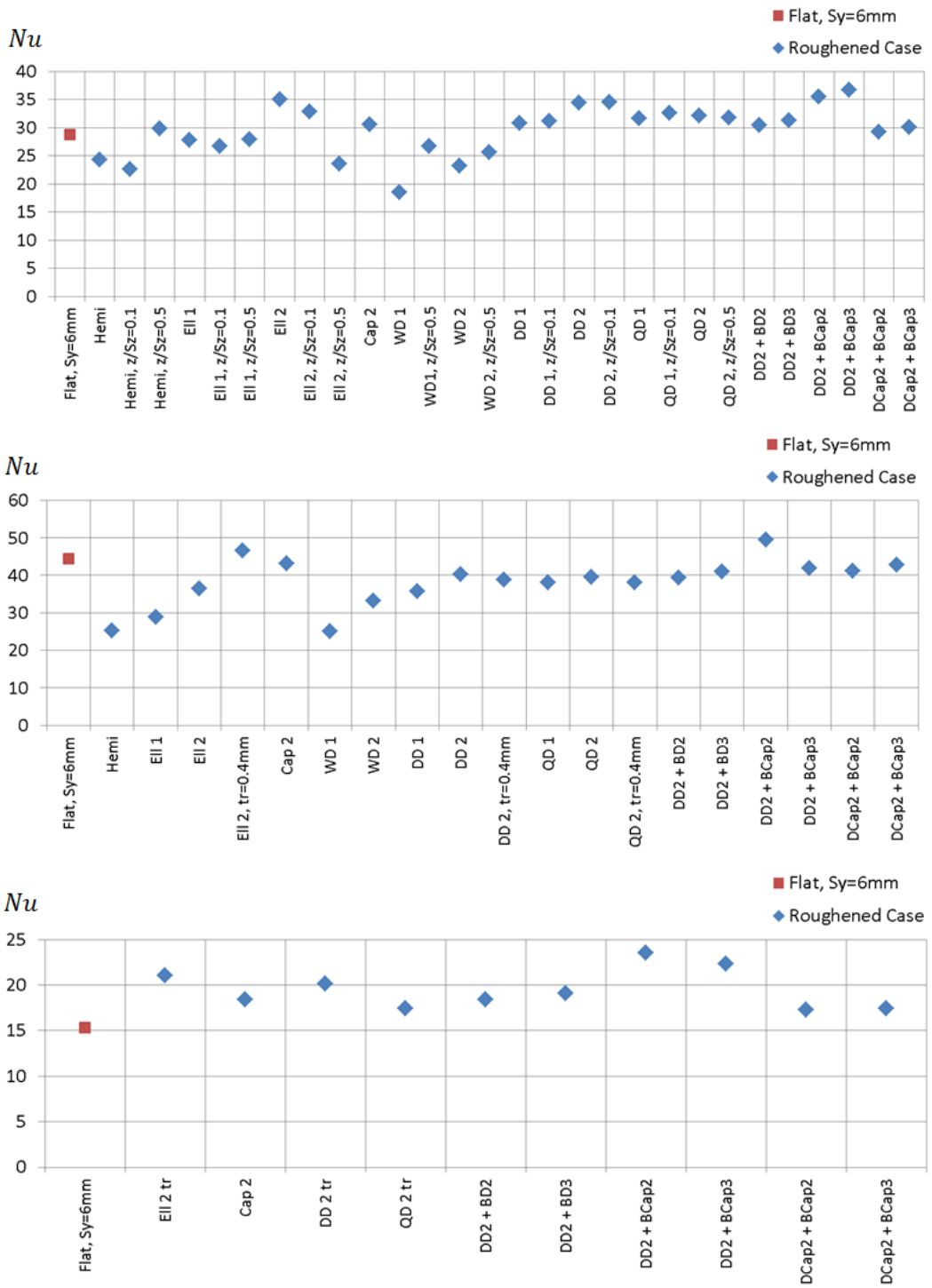

Figure 5.47 - Nusselt numbers obtained for all the patterns: no cross flow (top); $u_{CF} = 10\,m/s$ and $T_{UC} = 298\,K$ (center) or $T_{UC} = 328\,K$ (bottom).

Chapter 6

Conclusions

The purpose of the present research was to point out some solutions that allow improving the performance of the ACC system currently utilized to cool down the LPT casing by means of jet impingement.

The first step consisted into pointing out how the main design parameters of the ACC system influenced the available mass flow rate, with particular attention to the cruise phase. The analyses have been carried out with a DoE approach, by using a flow network solver, for a total of 64 runs.

Six parameters have been investigated: the diameter of the main pipe and manifold, the loss coefficient of the off-take, the discharge coefficient of the valve, the pipe roughness, the recovery factor of the diffuser near the off-take, the tapering of the axial headers. For each of these parameters, a non dimensional derivative has been calculated, in order to better compare their effects. These derivatives measured the variations of the mass flow rate in relation to those of the considered parameter. Although the diameter of the main pipe and manifold had the highest derivative, also those related to the off-take, the valve and the recovery factor were also significant. The roughness was found to be negligible (since the ACC pipes are quite smooth) as the tapering of the axial headers. The latter result was important in the perspective of weight reduction, since tapered (i.e. lighter) axial headers can be utilized without worsening the performance.

The results have been also utilized to investigate the robustness of the system. In other words, it was tested if, under the condition with a reduced diameter of the main pipe, an improvement of the other design parameters could balance the penalty in terms of available mass flow rate. In this way, it could be possible to reduce the overall weight of the ACC system. Several alternative solutions turned out to be promising.

Then, the flow network model has been integrated with a tool for the heat pick-up calculation, by means of an interface that allowed to analyze all the sections of the ACC pipeline.

Thanks to the low computational time required to carry out its tasks, this tool became interesting due to its capability to provide, already during the preliminary design, the circumferential distribution of the mass flow rate and temperatures for both the cooling air and the wall of the pipes. Then, it was applied to the DoE, revealing that the non-uniformity in feeding the several axial headers was significant. In particular, a reduced diameter of the main pipe and the manifold worsened this condition, with a difference up to 15% in mass flow rate between the first axial header and the last one. All the other investigated parameters had no significant effect on this circumferential distribution.

Moreover, none of the parameters included in the DoE significantly influenced the circumferential distribution of the air and metal temperatures. At this point, a statistical analysis was carried out on the air and metal temperatures for the spider rails of all the runs performed within the DoE. The approach was to analyzed one rail at a time, in order to point out how these temperatures spread in each of them. For the cooling air, the obtained Gaussian distributions exhibited larger standard deviations in the first rails, meaning a greater circumferential non-uniformity. On the contrary, lower standard deviations have been recorded in the last rails.

Finally, the last part of the research was focused on the heat transfer enhancement of the impinging jet technique. In the last decades, many literature works have been produced on this topic. Among the several methods available to achieve this objective, the roughening of the impinged surface appears to be promising for applications to the LPT casing. In this perspective, extended CFD investigations were carried out in order to identify some roughening patterns that allowed improving the performance of the ACC system.

The numerical model reproduced a row of impinging jets in the absence or in presence of an external cross flow, which represented the undercowl air flow. First of all, the flat surface was simulated and compared to the literature data, in order to verify that the physical phenomenon was adequately modeled. The agreement with well-known experimental studies in the literature was reasonable.

Then, the model was utilized to study several typologies of roughening patterns. First of all, simple dimples were investigated, finding out that shallow dimples placed under the impinging jet were more effective than the deeper ones. This result was also in agreement with a literature study. In addition, the shape of the dimple turned out to be important in determining the detachment of the wall boundary layer, especially in presence of cross flow. After this study, more complex roughening patterns were analyzed. Among the several geometries designed, the use of shallow, elliptical dimples combined with bumps of similar dimension resulted very promising. In particular, two patterns of this group significantly enhanced the heat transfer (up to 53.2% and 44.8%, for *DD2+BCap2* and *DD2+BCap3*, respectively). Finally, an evaluation of the weight increase, due to the use of the proposed patterns on the surface of the LPT casing, was carried out by measuring the volume on the CAD model. It turned out that the application of the surface roughening, theoretically, involved a reasonable weight increase of about sixty grams for every 1000 nozzles.

Despite the proposed solution appears to be promising in terms of heat transfer enhancement, there are several drawbacks when it comes to its practical application. To begin with, the additive manufacturing technique may encounter issues during the realization of these elements. Moreover, the surface roughness obtained with this method is quite high, so additional surface treatments may be required. Another factor that could significantly affect the performance of the roughening pattern is its misalignment with the impinging nozzle, both in the streamwise and in the spanwise directions. In this perspective, the contributions related to the thermal expansion and to the jet deflection under external cross flow may somehow be predicted and included in the design of the roughening elements. Another effect is related to the installation of the ACC pipes above the LPT casing, which has to be highly precise, in order to avoid the negative effects observed when a significant spanwise nozzle-to-dimple misalignment has been introduced.

Appendix

The 1D fluid network is realized by using a commercial software. It is composed by chambers and elements. For the elements, the geometry and the flow resistance are defined as input. There are boundary and internal chambers. While in the former, the fluid pressure, the temperature, the velocity and the flow direction are defined, the latter require initial guess values in terms of pressure ($p_{c,guess}$) and temperatures.

Once the model has been defined, a relaxed Newton-Raphson solver enforces, iteratively, the flow continuity in the internal chambers, within a specified tolerance. At each iteration, the software calculates the flow through the elements, $\dot{m}_{el}$, referring to the set of guessed pressures. In this way, temperatures and velocities are recalculated in all the internal chambers, based on the outlet conditions of those elements, whose flows enter each chamber. Then, a new set of pressure guesses can be calculated, by using the difference between inflow and outflow at the internal chambers ($\Delta\dot{m}_c = \dot{m}_{c,\,inlet} - \dot{m}_{c,\,exit}$) and the pressure losses defined for each element. This iterative procedure is carried out until convergence is reached.

About the elements that model the pipes, each of them is divided into fifteen stations. At each station, among the other values, the air temperature is calculated and the convection occurring with the inner walls of the pipe is taken into account. The temperature values of the inner wall of the pipes are provided as input data at each station and the convective heat transfer coefficient is calculated by means of an appropriate correlation (distinguishing between laminar or turbulent flow regimen). Consequently, the heat pick-up effect on the mass flow rate is also considered.

The thermal model requires as input the geometry and the distributions in terms of air temperature, pressure and mass flow rate. All these data are available from the fluid network solution. Then, as described in chapter 4, the solver calculates the wall temperatures of the pipes. Among these values, the inner temperatures are provided as input for the fluid network, in order to consider the heat pick-up. In order to couple two models that are written with different codes, the interface tool had to be developed in an environment that allowed the interface of the two programs.

Initially, both the thermal and the interface tool have been developed in Excel VBA. In this way, it was necessary to convert just the input and output files from the flow network model. Unfortunately, this version of the tool was too slow to be suitable for any use as a preliminary design tool. In particular, the structure of the interface program, made by Excel's macros, required to open (and, then, to close) a new instance of the thermal tool for each ACC part. Consequently, the heat pick-up analysis of all the 339 parts required about one hour and a half. Moreover, the macros required much time (about twenty minutes) for the conversion of the

obtained results into a new input file for the flow network solver. In total, the 1D thermal analysis of a single ACC system configuration required almost two hours.

In order to reduce the required computational time, it was necessary to modify the development environment. For this reason, a second version of the interface tool has been developed, in which the most of the code has been converted from the Excel macros to a Matlab code, including all the operations carried out by the thermal tool.

Besides the main script in Matlab, there are a few modules needed to support the main workflow of the tool.

First off all, there is a script that contains all the information not included in the flow network model and that can be set or directly modified by the user. These data, which are saved into matrices that will be utilized by the main script, are the thermal boundaries, the material properties and the geometrical data (thickness of the pipes and number of impingement nozzles for each rail). Other data included are the air properties that can be interpolated as required during the heat pick-up calculations. Moreover, this file also includes a vector that places in the correct order the several parts of the ACC system, basing on the ID number recorded for each element of the flow network solver.

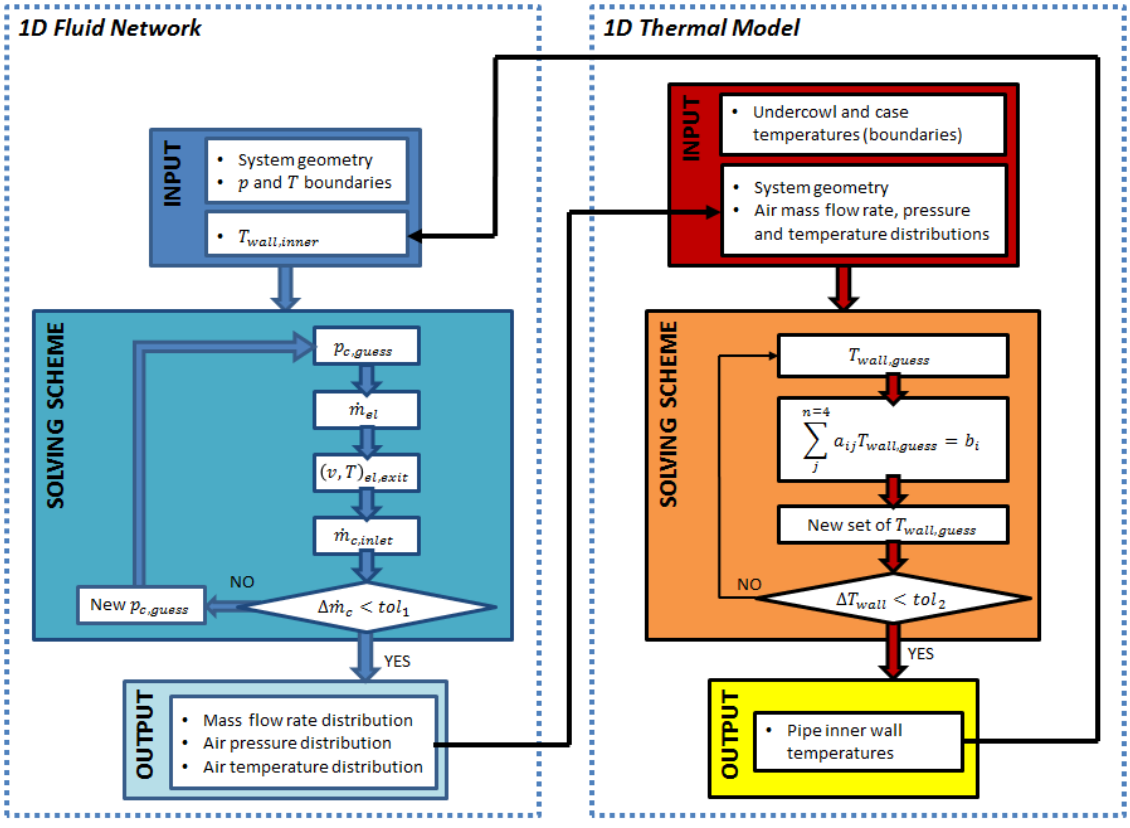

Figure A.1 - Coupled 1D solver.

Matlab has a function to easily import external files, such as the input and output files from the flow network model. When applied, this function creates a matrix into the Matlab workspace that should contain all the original data. Unfortunately, the import function does not work properly with the files from this software, since their data are not readable once the import function has been run.

Consequently, it is necessary to accomplish this task by using Excel. Once the correct data conversion has been ensured, the files from the flow network model are saved as *.xlsx* files. Now, they can be imported in Matlab's workspace and read without any problem.

The whole routine performed in Matlab just requires a couple of minutes to be accomplished, with a significant reduction in the required computational time, compared to the previous version running in VBA that required almost two hours. Hence, this second version of the interface tool could be utilized during the phase of preliminary design for the ACC system.

References

[1] https://www.unenvironment.org/resources/emissions-gap-report-2017.

[2] https://unfccc.int/process/the-kyoto-protocol.

[3] Ruijgrok, G.J.J. Van Paassen, D.M., *Elements of aircraft pollution*. Delft Academic Press, 2007.

[4] Lattime, S. B., Steinetz, B. M., *Turbine Engine Clearance Control Systems: Current Practices and Future Directions,* NASA Technical Memorandum TM-2002-211794, 2002.

[5] Chupp R. E., Hendricks, R. C., Lattime, S. B., Steinetz, B. M., *Sealing in Turbomachinery*, J. of Propulsion and Power, Vol. 22, pp. 313 – 349, 2006.

[6] Liang, G., *Turbine Rotor Blade with Multi-Vortex Tip Cooling Channels*, U.S.Patent 8,708645 B1, 2014.

[7] Glynn, C. C., Alford, M. E., Noe, M. E., Darkins, T. G. JR, *Turbine Engine Shroud Assembly Including Axially Floating Shroud Segment*, U.S. Patent 2004/0062639 A1, 2004.

[8] Carpenter, K. D., Wiedemer, J. D., Smith, P. A. JR, *Rotor Blade Outer Tip Seal Apparatus*, U.S. Patent 5,639,210, 1997.

[9] Catlow, R., Blade Tip Clearance Control Apparatus, U.S. Patent 5,211,534, 1993.

[10] Schimmels, S. A., Fusinato, D. J., Glessner, J. C., Mirkovich, D. N., Proctor, R., *Active Clearance Control Manifold System*, U.S. Patent 2014/0030066 A1, 2014.

[11] Matsunuma, T., Segawa, T., *Active Tip Clearance Flow Control for an Axial-Flow Turbine Rotor Using Ring-Type Plasma Actuators*, Proc. ASME Turbo Expo, GT2014-26390, 2014.

[12] Sun, F., Chaudhry, Z., *Electro-Thermally Active Seal for Fast Response Tip Clearance Control*, NNX13AB90A, 2014.

[13] DeCastro, J. A., Melcher, K. J., *A Study on the Requirements for Fast Active Turbine Tip Clearance Control Systems*, NASA Technical Memorandum TM-2004-213121, 2004.

[14] Kai, P., Ding, F., Fan, Y., Qiang, F., Yong, L., *Active generalized predictive control of turbine tip clearance for aero-engines*, Chinese J. of Aeronautics, 26, 1147-1155, 2013.

[15] Zubia, J., Berganza, A., Mateo, J., Vazquez, C., *Different Configurations of a Reflective Intensity-Modulated Optical Sensor to Avoid Modal Noise in Tip-Clearance Measurements*, J. Lightwave Technology, DOI: 10.1109/JLT.2015.2397473, 2015.

[16] Smith, C. D., *Active Tip Clearance Control for a Gas Turbine Engine*, European Patent EP2143889A2, 2010.

[17]https://commons.wikimedia.org/wiki/File:Salon_du_Bourget_20090619_254.jpg, photo by Georges Seguin, 19 June 2009.

[18] Da Soghe, R., Facchini, B., Micio, M., Andreini, A., *Aerothermal Analysis of a Turbine Casing Impingement Cooling System*, Int J of Rotating Machinery, 2012, DOI: 10.1155/2012/103583.

[19] Idel'chick, I.E., *Handbook of Hydraulic Resistance*, Research Institute for Gas Purification, Moscow, 1960.

[20] Miller, D.S., *Internal Fluid Systems*, 2nd Edition, 92-94, 1990.
[21] Moran, M.J., Shapiro, H.N., Munson, B.R., De Witt, D.P, *Introduction to Thermal Systems Engineering: Thermodynamics, Fluid Mechanics, and Heat Transfer*, Willey, 2003.
[22] Gubareff, G.G., Janssen, J.E., Torborg, R.H., *Thermal Radiation Properties Survey: A Review of the Literature*, Honeywell Inc, 1960.
[23] Incropera, F.P., DeWitt, D.P., Bergman, T.L., Lavine, A.S., *Fundamentals of Heat and Mass Transfer*, Sixth Edition, Chapter 2, pag 62, 2006.
[24] Taler, D., Taler, J., *Simple Heat Transfer Correlations for the Turbulent Tube Flow*, E3S Web of Conferences (13), 2017.
[25] Livingood, J. N. B., Hrycak, P., *Impingement Heat Transfer from Turbulent Air Jets to Flat Plates, a Literature Survey*, NASA/TM-X 2778, 1973.
[26] Zuckerman, N., Lior, N., Jet Impingement Heat Transfer: Physics, Correlations, and Numerical Modeling, Advances in Heat Transfer, 39, 565-631, 2006.
[27] Fox, M. D., Kurosaka, M., Hedges, L., Hirano, K., *The Influence of Vortical Structures on the Thermal Fields of Jets*, J. Fluid Mech., 255, 447-472, 1993.
[28] Weigand, B., Spring, S., *Multiple Jet Impingement- A Review*, Int. Symp. on Heat Transfer in Gas Turbine Systems, 2009.
[29] Perry, K. P., *Heat transfer by convection from a hot gas jet to a plane surface*, Proc Inst Mech Eng, 178, 175-180, 1954.
[30] Karagozian, A., *The Jet in a Crossflow*, Physics of Fluids, 26, 101303, 2014.
[31] Goldstein, R.J., Behbahani, A.I., *Impingement of a Circular Jet with and without Cross Flow*, Int J Heat and Mass Transfer, 25 (9), 1377-1382, 1982.
[32] Kamotani, Y., Greber, I., *Experiments in a Turbulent Jet in a Crossflow*, AIAA Journal, 10 (11), 1425-1429, 1972.
[33] Florschuetz, L.W., Metzger, D.E., Takeuchi, D.I., Berry, R.A., *Multiple Jet Impingement Heat Transfer Characteristic - Experimental Investigation of In-Line and Staggered Arrays with Crossflow*, NASA CR 3217, 1980.
[34] Kearton, W. J., Keh, T. H., 1952, *Leakage of Air through Labyrinth Glands of Staggered Type*, Proc. IMechE Series A, 116, 180 – 195, 1952.
[35] Florschuetz, L.W., Isoda, Y., *Flow Distributions and Discharge Coefficient Effects for Jet Array Impingement with Initial Crossflow*, 82-GT-156, 1982.
[36] Schulz, A., Gritsch, M., Wittig, S., *Effect of Crossflows on the Discharge Coefficient of Film Cooling Holes with Varying Angles of Inclination*, Proc ASME Turbo Expo, 2001-GT-0134, 2001.
[37] Andreini, A., Da Soghe, R., *Numerical Characterization of Aerodynamic Losses of Jet Arrays for Gas Turbine Applications*, J. Eng. Gas Turbines Power, 134, 052504, 2012.
[38] Da Soghe, R., Andreini, A., *Numerical Characterization of Pressure Drop for Turbine Casing Impingement Cooling System*, Proc ASME Turbo Expo, GT2012-68787, 2012.
[39] Engineering ToolBox, (2018). *Air - Prandtl Number*. [online] Available at: https://www.engineeringtoolbox.com/air-prandtl-number-viscosity-heat-capacity-thermal-conductivity-d_2009.html [Accessed 03 Feb 2019].
[40] Gardon, R., Cobonpue, J., *Heat Transfer Between a Flat Plate and Jets of Air Impinging on It*, International Developments in Heat Transfer, ASME, 454-460, 1963.

[41] Goldstein, R.J., Behbahani, A.I., Heppelmann, K.K., *Streamwise Distribution of the Recovery Factor and the Local Heat Transfer Coefficient to an Impinging Circular Air Jet*, Int J of Heat Mass Transfer, 29, 1227-1235, 1986.
[42] Florschuetz, L.W., Truman C. R., Metzger D. E., *Streamwise Flow and Heat Transfer Distributions for Jet Array Impingement with Crossflow*, J Heat Transfer, 103,337-342 (1981).
[43] Vejrazka, J., Tihon, J., *Effect of an external excitation on the flow structure in a circular impinging jet*, Physics of Fluids, 17, 105102-1-14, 2005.
[44] Liu, T., Sullivan, P., *Heat Transfer and Flow Structures in an Excited Circular Impinging Jet*, Int. J. Heat Mass Transfer, 39 (17), 3695-3706, 1996.
[45] Hwang, S. D., Lee, C. H., Cho, H. H., *Heat transfer and flow structures in axisymmetric impinging jet controlled by vortex pairing*, Int. J. Heat Fluid Flow, 22, 293-300, 2001.
[46] El-Gabry, L.A., Kaminski, D.A., *Experimental investigation of local heat transfer distribution on smooth and roughened surfaces under an array of angled impinging jets*, J. of Turbomach., 127, 532–544, 2004.
[47] Taslim, M.E., Setayeshgar, L. & Spring, S.D., *An experimental evaluation of advanced leading edge impingement cooling concepts*, J. of Turbomach., 123, 147–153, 2002.
[48] Kanokjaruvijit, K., Martinez-Botas, R.F., *Heat transfer and pressure investigation of dimple impingement*, Paper No. GT-2005-68823, IGTI Turbo Expo, Reno-Tahoe, Nevada, USA, 2005.
[49] Gau, C., Lee, C.C., *Impingement cooling flow structure and heat transfer along rib-roughened walls*, Int. J. Heat Mass Transfer, 35(11), 3009–3020, 1992.
[50] Yu, R., Peng, C., Chaoyi, W., *Experimental and Numerical Investigations of Impingement Heat Transfer on the Surface with Micro W-shaped Ribs*, Int. J. Heat Mass Transfer, 93, 683-694, 2016.
[51] http://www-mdp.eng.cam.ac.uk/web/library/enginfo/aerothermal_dvd_only/aero/atmos/atmos.html
[52] Guha, A., *Optimum Fan Pressure Ratio for Bypass Engines with Separate or Mixed Exhaust Streams*, J Propulsion and Power, 17 (5), 1117-1122, 2001.
[53] https://blogs.nasa.gov/J2X/tag/main-oxidizer-valve/
[54] https://www.unitedstatesfittings.com/true-wyes/
[55] https://slideplayer.com.br/slide/2321443/
[56] http://blog.opticontrols.com/archives/994
[57] Colebrook, C.F., *Turbulent Flow in Pipes, with Particular Reference to the Transition Region between the Smooth and Rough Pipe Laws*, Journal of the Institution of Civil Engineers, 11 (4), 133–156, 1939.
[58] Moody, L. F., *Friction factors for pipe flow,* Transactions of the ASME, 66 (8), 671–684, 1944.
[59] https://en.wikipedia.org/wiki/Moody_chart, graph by S. Beck and R. Collins, University of Sheffield, 26 May 2017.
[60] Engineering ToolBox, (2005). *Dry Air Properties*. [online] Available at: https://www.engineeringtoolbox.com/dry-air-properties-d_973.html [Accessed 23 02 2019].
[61] Ross, S. M., *Introduction to Probability and Statistics for Engineers and Scientists*, Academic Press, 2009.
[62] http://sro.sussex.ac.uk/id/eprint/67414/1/ManufactureofTurbomachinery4.pdf

[63] Lars-Erik Lindgren, *Computational Welding Mechanics*, Woodhead Publishing, 190-196, 2007.
[64] Magerramova, L., Vasilyev, B., Kinzburskiy, V., *Novel Designs of Turbine Blades for Additive Manufacturing*, Proc ASME Turbo Expo, GT2016-56084, 2016.
[65] Zuckerman, N., Lior, N., *Impingement Heat Transfer: Correlations and Numerical Modeling*, J Heat Transfer, 127 (5), 544-552, 2005.
[66] Andreini, A., Da Soghe, R., Facchini, B., Maiuolo, F., Tarchi, L., Coutandin, D., *Experimental and Numerical Analysis of Multiple Impingement Jet Arrays for an Active Clearance Control System*, Proc ASME Turbo Expo, GT2012-68791, 287-299, 2012.
[67] *Ansys CFX-Solver Theory Guide*, Chapter 9, 255-256, 2009.
[68] http://www.itcmp.pwr.wroc.pl/~znmp/dydaktyka/fundam_FM/Lecture_no3_Turbulent_flow_Modelling.pdf
[69] Salim, M., Cheah, S.C., *Wall y^+Strategy for Dealing with Wall-bounded Turbulent Flows*, Proc Int MultiConference of Engineers and Computer Scientists, 2, 2165-2170, 2009.
[70] https://www.sharcnet.ca/Software/Ansys/17.0/en-us/help/wb_msh/msh_skew-ness.html
[71] *Introduction to additive manufacturing technology*, European Powder Metallurgy Association, 2015.
[72] Gora, W.S, Tian, Y., Cabo, A.P., Ardron, M., Maier, R.R.J., Prangnell, P., Weston, N.J., Hand, D.P., *Enhancing Surface Finish of Additively Manufactured Titanium and Cobalt Chrome Elements Using Laser Based Finishing*, Physics Procedia, 83, 258-263, 2016.